MINISTRY OF HIGHER EDUCATION AND SCIENTIFIC RESEARCH
HASSIBA BENBOUALI UNIVERSITY OF CHLEF

FACULTY OF TECHNOLOGY

MECHANICAL ENGINEERING DEPARTMENT

THESIS

presented to obtain the degree of

DOCTORATE

Major: Mechanical Engineering

Specialty: Mechanical Manufacturing and Production

by

Adel HADJ AMAR

Title:

Study of the aptitude of DC0xEK steels for enameling and deep drawing

Defended on 19/12/2024, before a jury composed of:

MENDAS Mohammed	Professor	Chlef university	President
HADJ MILOUD Mohamed	MCA	Chlef university	Examiner
BENDALI Nadir	MCA	Khemis-Miliana university	Examiner
MEDJDOUB Sidi Mohamed	MCA	Sidi Bel Abbes university	Examiner
ZAHLOUL Hamou	Professor	Chlef university	Supervisor
ZIDANE Ibrahim	Professor	Chlef university	Co-Supervisor
BENHADJ M'HAMED Ali	Chief Production Engineer	EIMS Miliana	Invited

Acknowledgements

Abstract

In this study, we investigated the aptitude of cold-rolled steels DC05EK and DC06EK for deep drawing and enameling in the Industrial Sanitary Equipment Company (EIMS) of Miliana. The first part aimed to perform a numerical simulation of the bathtub type "1400" using real industrial parameters to analyze wrinkling and rupture defects. We utilized the ABAQUS/Explicit FE software. 3D and ultrasonic thickness measurements were carried out on a bathtub manufactured without defects. Numerical and experimental plots of the thickness reduction show that the two approaches are in good agreement. The numerical results indicated no rupture or wrinkling in the final bathtub shape, matching the actual product made by the company. Numerical analysis was also performed on various scenarios likely to cause defects, such as the influence of blank holder pressure, the initial blank shape, and the die design using draw beads. The second part aimed to analyze the occurrence of fish scale defects in enameled sanitary ware, focusing on the different levels of plastic strain and anisotropy encountered in the deep drawing of DC06EK and DC05EK sheet metals. Additionally, corrosion phenomena in these types of steel based on different deformation levels were examinate. Experiments were conducted on pre-strained samples. These samples were enameled following the same process used at the EIMS company. After 20 days, fish scale began to appear in samples with plastic strain levels between 0 and 3%. This phenomenon was explained by the release of the hydrogen chemical component and the low roughness. Overall, we concluded that DC05EK steel is more resistant to fish scale defects and corrosion, whereas DC06EK steel has better formability.

Key words: Bathtub; Deep drawing; Experimental measurements; Numerical simulation; Enameling; Fish scale.

Résumé

Dans cette étude, nous avons étudié l'aptitude des aciers laminés à froid DC05EK et DC06EK pour l'emboutissage profond et l'émaillage dans l'Entreprise Industrielle de Matériel Sanitaire (EIMS) de Miliana. La première partie visait à réaliser une simulation numérique de la baignoire type « 1400 » en utilisant des paramètres industriels réels pour analyser les défauts de plissement et de rupture. Des mesures 3D et d'épaisseur par ultrason ont été réalisées sur une baignoire fabriquée sans défaut. Les résultats numériques et expérimentaux sur la réduction d'épaisseur ont montré une bonne concordance. Les résultats numériques ont indiqué qu'il n'y avait ni ruptures ni plissements dans la forme finale de la baignoire, correspondant au produit réel fabriqué par l'entreprise. Une analyse numérique a également été réalisée sur divers scénarios susceptibles de provoquer des défauts, tels que l'influence de la pression du serre-flan, la forme géométrique initiale de la tôle et la conception de la matrice avec des bourrelets d'étirage. La deuxième partie visait à analyser l'apparition de défauts de coups d'ongle dans les appareils sanitaires émaillés, en se concentrant sur les différents niveaux de déformation plastique et l'anisotropie rencontrés lors de l'emboutissage des tôles DC05EK et DC06EK. De plus, les phénomènes de corrosion dans ces types d'acier en fonction des différents niveaux de déformation ont été examinés. Des expériences ont été menées sur des échantillons pré-déformés. Ces échantillons ont été émaillés en suivant le même processus utilisé chez l'EIMS. Après 20 jours, des marques d'ongles ont commencé à apparaître sur des échantillons avec des niveaux de déformation plastique entre 0 et 3%. Ce phénomène a été expliqué par la libération de la composante chimique de l'hydrogène et la faible rugosité. En conclusion, nous avons constaté que l'acier DC05EK est plus résistant aux défauts d'écailles de poisson et à la corrosion, tandis que l'acier DC06EK a une meilleure formabilité.

Mots-clés : Baignoire ; Emboutissage profond ; Mesures expérimentales ; Simulation numérique ; Émaillage ; Coups d'ongle.

ملخص

في هذه الدراسة، قمنا بدراسة مدى ملاءمة الفولاذ المدرفل على البارد نوع DC05EK وDC06EK لعمليات التشكيل الصفائحي العميق و الطلاء بالمينا في شركة EIMS بمليانة. استهدف الجزء الأول إجراء محاكاة رقمية لحوض الاستحمام نوع "1400" باستخدام معايير صناعية حقيقية لدراسة و تحليل عيوب التجاعيد والتمزق. استخدمنا برنامج التحليل بالعنصر المحدد Abaqus/explicit. تم إجراء قياسات ثلاثية الأبعاد وفوق صوتية على حوض استحمام خالٍ من العيوب. أظهرت النتائج الرقمية والتجريبية لتباين السمك توافقًا جيدًا. وأشارت النتائج الرقمية إلى عدم وجود تمزق أو تجاعيد في الشكل النهائي لحوض الاستحمام، وهو ما يتطابق مع المنتج الفعلي الذي تم صناعته في الشركة. كما تم إجراء تحليل رقمي على سيناريوهات مختلفة قد تسبب عيوبًا مثل تأثير ضغط حامل الصفيحة، الشكل الأولي للصفيحة وتصميم القالب باستخدام قضبان السحب. استهدف الجزء الثاني تحليل ظهور عيوب القشور السمكية في الأجهزة الصحية المطلية بالمينا، بالتركيز على تشوه البلاستيكي (التصلب) وتباين الخواص أثناء تشكيل صفائح DC06EK وDC05EK. بالإضافة إلى ذلك، قمنا بدراسة ظواهر التآكل في هذه الأنواع من الفولاذ بناءً على مستويات التشوه المختلفة. أُجريت التجارب على عينات معدة و ممدودة مسبقًا وفقًا لظروف تشكيل صفائح DC06EK وDC05EK. تم طلاء هذه العينات بالمينا باتباع نفس العملية المستخدمة في شركة EIMS في مليانة. بعد مرور 20 يومًا، بدأت تظهر علامات الأظافر على العينات التي لديها مستوى تشوه بلاستيكي بين 0 و 3%. تم تفسير هذه الظاهرة بإطلاق مكون الهيدروجين الكيميائي والخشونة المنخفضة. في الختام، خلصنا إلى أن الصفيحة DC05EK أكثر مقاومة لعيوب القشور السمكية والتآكل، بينما تتمتع الصفيحة DC06EK بقابلية تشكيل أفضل.

كلمات البحث: حوض الاستحمام ؛ التشكيل الصفائحي العميق ؛ قياسات تجريبية ؛ محاكاة عددية ؛ الطلاء بالمينا ؛ قشور السمكية.

Table of Contents

List of figures

VI

List of tables

Nomenclature

A	Elongation	[%]
E	Young's modulus	[GPa]
F, G, H, N	Hill parameters	[-]
K	Material consistency	[-]
L_0	Initial length of the specimen	[mm]
L_r	Final length of the specimen	[mm]
Δl	Elongation of the specimen	[mm]
n	Hardening exponent	[-]
r	Lankford coefficient	[-]
r_0, r_{45}, r_{90}	Lankford's r-values	[-]
R_e	Elastic strength	[MPa]
$R_{p0.2}$	Yield stress	[MPa]
R_m	Tensile strength	[MPa]
R_r	Breaking points	[MPa]
S	Cross-section of specimen	[mm^2]
S_0	Initial cross-section of metal	[mm^2]
t_0	Sheet metal thickness	[mm]
α	Hardening parameter	[-]
ε	Elastic strain	[%]
ε_0	Strain at yield point	[%]
ε_p	Equivalent plastic strain	[-]
ε_{true}	True strain	[%]
ε_n	Nominal strain	[%]
$\dot{\bar{\varepsilon}}^p$	Equivalent plastic strain	[%]
$\varepsilon_1, \varepsilon_2, \varepsilon_3$	Principal strains	[%]

μ	Friction coefficient	[-]
ν	Poisson's ratio	[-]
σ_H	Hill equivalent stress	[MPa]
σ_0	Stress at yield	[MPa]
σ_{true}	True stress	[MPa]
σ_n	Nominal stress	[MPa]
σ_y	Plasticity threshold stress	[MPa]
σ_s	Saturation stress	[MPa]
σ_{ij}	Stress tensor components	[MPa]
$\sigma_{xx}, \sigma_{yy}, \sigma_{zz}$	Plane stresses	[MPa]

Abbreviations

BHP	Blank holder pressure
CAD	Computer-Aided Design
COF	Coefficient of Friction
DIC	Digital Image Correlation
EED	Extra-deep drawing
FE	Finite element
EIMS	Industrial Sanitary Equipment Company
FLC	Forming Limit Curve
RD	Rolling direction
VBHF	Variable blank holder force
VBHP	Variable blank holder pressure

Introduction

Deep drawing is a sheet metal forming technique that is used extensively at the 'EIMS' company. This company is currently facing significant losses in production time and costs due to defects such as ruptures, wrinkling, and especially enamel coating issues. These losses have become a real problem for many industrial companies during the Coronavirus pandemic, especially with the rising costs, acquisition difficulties, and quality concerns of imported DC0xEK steel sheets. The goal of this thesis is to study the suitability of these steel sheets for enameling and deep drawing of sanitary products to minimize company losses. This study must meet potentially conflicting requirements: formability, fish scale resistance, enamel adhesion, and good surface appearance after enameling.

Numerical simulation is an essential tool for modeling the manufacturing of deep-drawn products with real industrial parameters used in EIMS. This tool predicts rupture and wrinkling defects and studies formability. However, fish scale resistance, enamel adhesion, and post-enameling surface appearance can only be experimentally studied at EIMS. These aspects increase the research difficulty, but their application is not limited to a specific process. Thus, the research results can be applied to other investigations. The industrial contribution addresses industrial demands by optimizing forming cycle times and energy inputs for time and cost savings, reducing part weight, and optimizing part shapes to improve rigidity and service performance.

This thesis is divided into four chapters:

The first chapter starts with a brief introduction to EIMS, followed by an overview of the deep drawing and enameling processes. It then describes the steps involved in manufacturing bathtubs through an extra-deep drawing process. Next, real examples from EIMS are used to illustrate the failure modes and reasons for rejecting bathtubs. This underscores the need for numerical simulation to reduce rejection rates. A literature review in this research area, with an emphasis on numerical simulation, is provided.

In the second chapter, the DC06EK and DC05EK sheet materials are analyzed and subjected to mechanical testing. The experimental methods and procedures are

1

thoroughly described. Physicochemical characterization was performed using techniques such as spectrometry for chemical composition analysis and optical microscopy for metallographic examination. Tensile tests were conducted in three different orientations relative to the rolling direction, and a tribology test was performed to determine the coefficient of friction. To validate the numerical approach discussed in the third chapter, 3D and ultrasonic thickness measurements were conducted on a defect-free manufactured bathtub.

In the third chapter, the main goal is to conduct a numerical simulation of the bathtub forming process using the real industrial parameters used at EIMS. This involves controlling the non-uniform pressures generated by six actuators applied to the blank holder to manage the sheet metal (blank) flow between the die and the blank holder, aiming to produce a defect-free product. Additionally, it is essential to examine various scenarios that could result in rupture and wrinkling defects, including the influence of the blank holder pressure (BHP), the initial blank shape, and the die design using draw beads.

In the final chapter, our experimental investigation aims to analyze the occurrence of fish scale defects in enameled sanitary ware, focusing on the different levels of plastic strain and anisotropy induced during the deep drawing of DC06EK and DC05EK sheet metals. Additionally, we aim to examine the corrosion phenomena in these types of steel as they relate to different levels of deformation.

Chapter 1.   Deep Drawing and Enameling: Basics and Applications

1.1. **Introduction**

The deep drawing process shapes components from sheet metals. Typically, this technique is applied at room temperature, although it can sometimes be performed at elevated temperatures to enhance the metal's formability. This process involves the plastic strain of thin metal sheets using specialized tools to create complex parts. The sheet metals are generally obtained from rolling process and made from ductile metal alloys. Deep drawing processes are extensively used across nearly all mechanical industries.

The deep-drawing process holds significant industrial importance due to the high volume of parts it produces. Utilizing thin sheets in this process results in considerable weight and material savings. Additionally, the shaped parts are often very rigid due to their design, achieving an excellent strength-to-weight ratio that is highly valued in various industries. Consequently, this method is widely applied in the production of metal furniture, household appliances, metal packaging, aerospace components, and especially in the automotive industry. Another major benefit of this process is its suitability for continuous, mass production, with specialized tools allowing for production rates of approximately 60 parts per minute [1].

At the EIMS of Miliana, cold deep drawing is extensively used to create household appliances and sanitary products of varying complexity. This study focuses on enhancing the production quality of bathtubs because this product is the most complex in manufacturing. In a competitive industrial environment, EIMS aims to reduce manufacturing and development times and lower costs for new products. A key objective is to minimize the rejection rate of deep-drawn parts. The main issues causing these rejections are necking, rupture, and wrinkling in the final product. Additionally, the company faces a growing problem with excessive rejects in enameled products, particularly following the extra-deep drawing process using DC06EK steel sheets. The primary issue is the appearance of fish scales on sanitary products, which become visible a few days after the enameling process. This problem has become a significant concern for many industrial companies, especially during the "Coronavirus" pandemic, exacerbating challenges with increased costs, difficulties in sourcing DC06EK sheet

metal, and concerns about its quality. To address these challenges, EIMS strives to optimize its deep drawing processes and improve product quality, ultimately leading to greater efficiency and higher customer satisfaction.

After a brief introduction to EIMS, the steps involved in manufacturing bathtubs are presented. Subsequently, failure modes and rejection reasons for bathtubs are illustrated with real examples from EIMS. This aspect highlights the necessity of using numerical simulation to reduce rejection rates. Since the focus is on numerical simulation, a literature review is proposed in this area of research. And for defects occurring during the enameling process, such as fish scale, we have discussed the causes of this problem and how to manage the process to avoid it.

1.2.   EIMS Company presentation

The "Industrial Company of Sanitary Equipment", called "In French: Enterprise Industrielle de Matériel Sanitaire (EIMS)" is a joint-stock company with a share capital of 485,000,000.00 DA. Its social head office is located in Miliana, Wilaya, of AIN DEFLA. EIMS has been, since 2018, a subsidiary of "HOLDING ELEC EL DJAZAIR". Table 1-1 is company sheet identification [2].

The parent company of EIMS in its beginning was a production unit of SN METAL carried out under the 1974 quadrennial plan and put into operation in 1979. In 1983, it became a part of PROMETAL through the restructuring of SM METAL. Then, in 1998, PROMETAL was liquidated, and this unit was transferred to ENIEM. Finally, on January 1, 2018, it was transferred to the Industrial Group ELEC EL DJZAIR [2].

EIMS is specialized in the production and marketing of sanitary goods in enameled steel and stainless steel. The company manufactures and commercializes a range of sanitary articles with various dimensions and types. These products include:

Sanitary ware in enameled steel:

- Bathtubs: Available in three sizes – 1,70m x 0,70m, 1,60m x 0,70m, and 1,40m x 0,70m.
- Shower Trays: Sized at 0,70m x 0,70m.

- Washbasins: Offered in two sizes – 0,60m x 0,50m and 1,20m x 0,60m.
- Single-bowl Kitchen Sinks: Measuring 1,00m x 0,60m.
- Double-bowl Kitchen Sinks: With dimensions of 1,20m x 0,50m.

Household appliances and other products:

- Natural gas heater 9000 kcal.
- Flat two-burner enamelled steel stove.
- Electronic weighing scale.
- Wheelbarrow.
- Light pole reflector.
- Office ceiling light.
- Light pole caps.
- 770 L galvanized trash bin with PVC lid

With a production capacity of 70,000 units per year and an efficient work schedule of 8 hours per day and 5 days per week, the company can meet the demand for these various sanitary and steel products.

Table 1-1: Company sheet identification [2].

Company name	Sanitary Equipment Industrial Company "EIMS"
Share capital	485 000 000.00 DA
Legal form	Stock company
NRC	0763932 B05
Address	Hammam Road, BP 47 Miliana, Ain Defla Province
Parent company	Holding elec el djazair
CEO	Mr. HAMDI Benyoucef
Personnel	150 employees.
Creation date	1979

Currently, and over its 44 years of existence, the company has acquired extensive multidisciplinary experience in the fields of deep drawing, enameling, and thermoforming.

1.3. *General information on deep drawing*

1.3.1. Cold deep drawing process

The deep drawing process is a forming technique that involves the plastic strain of thin metal sheets at room temperature to produce parts with varying levels of complexity. Deep drawing operations are performed using mechanical or hydraulic presses. The tooling used with these presses typically consists of a punch, a die, and a blank holder. The shape of the part is achieved through the combined action of the punch on the die, which defines the final geometry of the part after deformation, and optionally a blank holder that controls the flow of the sheet metal (blank) (Figure 1-1). As a result, specific tooling is associated with each series of parts to be formed [3].

Deep drawing is carried out using hydraulic or mechanical presses, in which the following main tools are almost always installed:

- A die that roughly matches the outer shape of the desired part.
- A punch, having the inner shape of the part, which pushes into the die.
- A suitable blank sheet metal, commonly referred to as "blank"
- A blank holder that presses the blank against the outer side of the die to prevent the formation of wrinkles and regulate the flow of sheet metal into the tool.
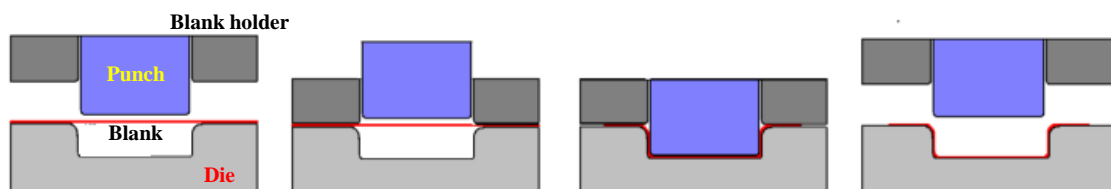
Figure 1-1 : Principle of the deep-drawing process[4]**.**

1.3.1.1. Die

The die is the largest component of the tool since the punch must push the sheet metal into it, and it needs to fully support the blank. When examining a die, one can observe a central cavity whose shape closely replicates that of the part to be manufactured, surrounded by a flat or contoured annular surface on which the blank rests at the start of the deep drawing process. This surface may have braking elements such as draw beads. Draw beads are features designed into the die to control the flow of material. These beads

create resistance during the drawing operation, which helps to prevent wrinkling and control the stretching of the material. By strategically placing draw beads in the die, manufacturers can ensure that the metal sheet flows uniformly into the die cavity, resulting in a smoother, more precise final product. [5].

In the realm of deep drawing, the die radius is an important aspect to consider. It refers to the curvature around the die cavity and can vary in value along its circumference. This deliberate variation allows for smoother material flow and facilitates metal flow during deformation [5]. Manufacturers strategically design the die radius to optimize the deep drawing process, ensuring efficient material transfer and minimizing potential defects. Properly adjusting the die radius enhances the overall performance and quality of the deep-drawn parts.

1.3.1.2. Blank -holder

The blank holder is an essential element in nearly all deep drawing tools, with very few exceptions. The blank holder can first be directly applied to the blank (the metal sheet) to hold it against the die. This opposes the formation of wrinkling, due to what we call the "confinement effect", and rupture. However, there is a different case, often used industrially with mechanical presses, especially when the tool includes ridges. In this case, the blank holder rests on stops, also known as compensation shims, located around the die to prevent its movement. Instead of controlling pressure on the sheet, a clearance is managed between the blank holder and the die. This clearance must be minimized to avoid the formation of wrinkles [5]. It is also important to design draw beads into the blank holder to control the flow of material. The latter helps to prevent wrinkles and control the stretching of the material.

In other industrial cases, a lubricant is used in the contact area between the sheet and the die. When the blank holder ensures this contact in the presence of the lubricant, it allows for better material flow within the die. This is particularly helpful in improving the formability of the sheet during the deep drawing process.

1.3.1.3. Punch

The shape of the die typically replicates the inner shape of the desired part, unless curvature corrections have been applied to compensate for springback. Unless the punch nose is perfectly flat and surrounded by a very small punch radius, the metal will experience expansion and slide over the punch. To prevent this, the punch must be carefully polished. However, expansion comes at the expense of material thickness, and in rare cases where the intended use of the part requires limiting thinning at the punch nose, sandblasting the punch nose may be employed. Sandblasting helps to reduce metal deformation and maintain the desired thickness [5].

1.3.2. Deformation modes in deep drawing in the bathtub

Deep drawing imposes different modes of deformation, which are cited below [5]:

- Zone A: corresponds to the s*hrink drawing* mode. In this case, the blank is stretched in one direction while shrinking in the other. Whereas: $\varepsilon_1 > 0$ and $\varepsilon_2 < 0$.

- Zone B: corresponds to the *plane deformation* mode. The major deformation (ε_1) is positive, while the minor deformation (ε_2) is equal to zero: $\varepsilon_1 > 0$ and $\varepsilon_2 = 0$.

- Zone C: corresponds to the *expansion* mode. The two deformations are positive: $\varepsilon_1 > \varepsilon_2 > 0$.

- Zone D: corresponds to the *equibiaxial expansion* mode. The two deformations are equal and positive: $\varepsilon_1 = \varepsilon_2 > 0$.
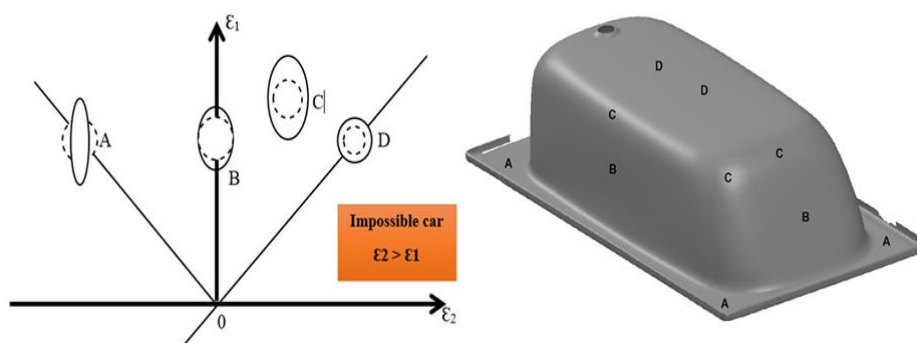
Figure 1-2 : Main mode of deformation of a deep-drawn part.

1.4.   General information on enameling

Enameling is a coating technique that consists of depositing a layer of slip, made up of a mixture of water and finely ground metal oxides (silica, alumina), on the substrate by englobing, conventional spraying or electrostatic spraying, this very old technique can be applied to stoneware, earthenware, cast iron and also steel. It produces a hard, smooth surface comparable to glass, which is easy to wash and therefore ideal for use in kitchens and sanitaryware [6].

Enamel refers to a predominantly glassy or vitreous inorganic coating adhered to various steel surfaces through high-temperature thermal fusion. Vitreous enamel exhibits numerous desirable qualities including resistance to corrosion, abrasion, wear, and chemical exposure, color stability, high hardness, and non-flammability. Enamel can be categorized into two types: enamel mass, which directly interfaces with the bathtub surface, and enamel cover, a synthetic coating [7].

The widest range of steels for enameling, adapted to the process used by enamellers [6]:

- Decarburized steels for direct enameling (ED).
- Steel for conventional enameling (EK).
- Titanium steel for enameling.
- Aluminized steel for low-temperature enameling.

1.4.1. Different types of enamel

Enamels vary in composition based on the type of substrate being coated and, for steel, depending on the enameling process employed.

1.4.1.1.   Enamel and substrate

The composition of enamels is adjusted to align the enamel firing temperature with the substrate. Higher firing temperatures typically enhance the quality of enameled parts. However, the metal limits the firing temperature due to the characteristics of the substrate; for instance, phase changes in steel must be considered. Additionally, the enamel's coefficient of expansion must be compatible with that of the substrate.

1.4.1.2. Different types of enamel for steel

- Ground-coat enamel

Ground-coat enamel includes metal oxides (such as Co and Cu oxides), which enhance adhesion to steel by forming alloys with the iron in the steel. Due to the dark color of these metal oxides, white ground-coat enamel is not available. There are also more reactive ground-coat enamels, which contain a higher proportion of metal oxides, eliminating the need to pickle the steel before enameling. These reactive enamels are typically used in the two-coat/one-fire enameling process [8].

Ground-coat enamel also protects the enameled part against corrosion. Additionally, depending on the type of part to be enameled, other components may be added to achieve specific properties:

- Acid-resistant properties (such as for oven cavities and drip pans) by adding TiO_2
- Alkali-resistant properties (such as for sanitary ware and washing machines) by adding ZrO_2
- Enhanced corrosion resistance for water heater applications by adding ZrO_2 and Al_2O_3

The composition of the ground coat layer used at EIMS will be provided in the Table 1-2:

Table 1-2 : Composition of mass enamel used by EIMS for coating bathtubs.

Code	Name
502 111 29	Frit 2299
502 11130	Frit 1102 tr
502 122 02	Quartz 200
502 121 05	Clay 02
502 121 00	Bentonite
502 125 01	Boric acid (borax)
502 124 02	Carbonate of k
502 124 05	K 12
502 125 02	Eraser 416

- Self-Cleaning Enamels

Self-cleaning enamels are used in domestic ovens to help eliminate fat produced during cooking. There are two types of self-cleaning enamels: catalytic and pyrolytic. Consequently, we have catalytic and pyrolytic self-cleaning ovens [8].

Catalytic Cleaning: This process occurs while the oven is operating normally, at around 200°C. The enamel contains oxides that catalyze the breakdown of fat into water and carbon dioxide. Additionally, this type of enamel is very refractory and porous, which increases the contact surface between the enamel and the fat, thus facilitating its elimination:

$$Cx\,Hy\,Oz + catalyst \rightarrow xH2O + yCO2 \qquad (a)$$
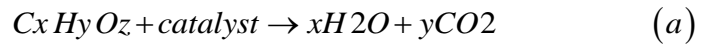
Efficiency decreases over time due to the progressive blockage of the pores.

Pyrolytic Cleaning: This process occurs while the oven is empty, at approximately 520°C. Fat and residues deposited on the walls during cooking are burned off at this temperature, leaving only a carbon deposit that can be wiped away:

$$Cx\,Hy\,Oz + heat \rightarrow xC + yH2O \qquad (b)$$
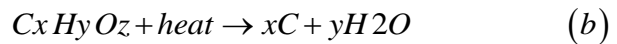
This type of enamel has a softening point higher than the pyrolytic temperature. It is glossy, non-porous, and highly resistant to acids and alkalis.

- Cover-coat enamels

Cover-coat enamels provide enameled parts with their aesthetic qualities and enhance their chemical resistance. However, because they do not contain any adhesion agents, they cannot be used alone on a metal substrate under any circumstances. The composition of the cover-coat enamels ground used at EIMS of sanitary is given as follow:

- T5964
- BENTONITE

- CLAY: 10

- SODIUM ALUMINATE

- POTTASSE CARBONATE

- RUBBER 416

- SODA NITRITE

- UREA

1.4.2. Grinding

Enamel frit cannot be used in its raw form. It must first be mixed with other ingredients and then ground. Grinding is a crucial step in the enamel preparation process as it ensures the production of a highly refined, perfectly homogeneous, stable, and uncontaminated product (Figure 1-3). The enamel slurry, composed of frit, clay, sand, and water, is ground in ball mills at the plant. The grinding process takes about 14 hours, depending on the nature of the ingredients and the desired fineness.

Figure 1-3 : Grinders used at EIMS to grind mass and covering enamel.

1.4.3. Enameling process

The enameling process involves applying and firing one or more layers of enamel on one or both sides of a suitable steel substrate.

Successful enameling is characterized by:

- Good adhesion of enamel to steel.
- Good surface appearance after firing the enamel.

The carbon content of the steel can impact the attainment of these two properties. Carbon is crucial for ensuring enamel adhesion. However, if its content is excessively high, it can negatively affect the surface appearance of the enamel due to the release of gaseous CO and CO_2 during firing. This contradiction explains the range of enameling processes available [8].

The enameling process typically involves several steps:

1- Preparation of the part surface after forming
2- Preparation of the enamel
3- Application of the enamel to the steel
4- Drying
5- Firing at high temperature

Several enameling processes are available, depending on the type of part and desired final appearance:

1- Enameling on hot rolled substrate
2- Conventional enameling (two coats/two firings)
3- Ground-coat enameling (one coat/one firing)
4- Direct-on white enameling
5- Two-coat/one-fire enameling
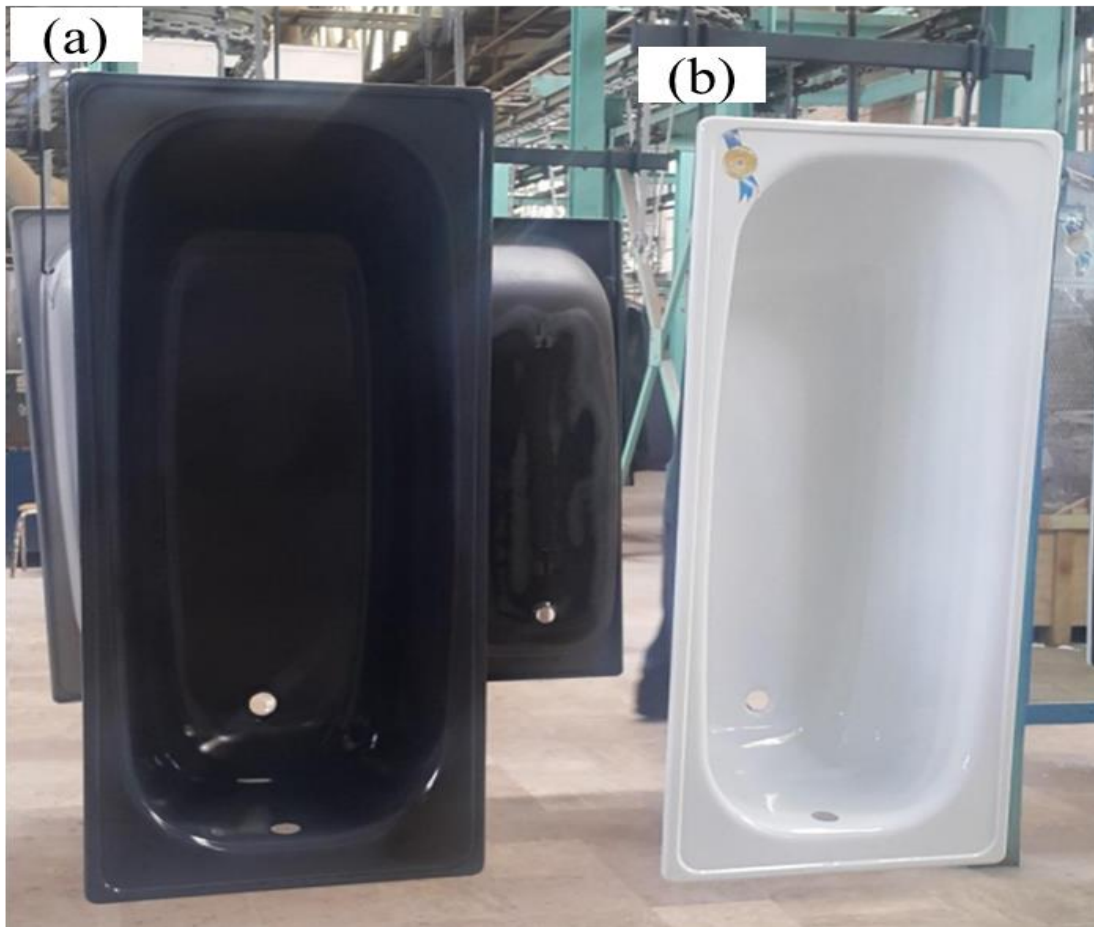
Figure 1-4 : Bathtubs after firing: (a) bathtub covered with the ground coat enamel; (b) bathtub covered with the Two-coat.

1.5.   Manufacturing of bathtubs

1.5.1. Sheet metals used in deep drawing

The materials of the sheet metal used by EIMS (Figure 1-5) in the bathtub deep drawing process are DC06EK and DC05EK (cold-rolled steel for cold forming, quality index 06 or 05, for conventional enameling (EK)). The Table 1-3 shows the chemical composition of the DC06EK and DC05EK materials, see Annex 3.

Table 1-3 : Chemical composition of DC05EK and DC06EK material [2].

Element	C	S	N	Mn	P	Si	Al	Ni	V	Ti	Cr
DC05EK	0.050	0.025	0.072	0.180	0.008	0.005	0.034	0.019	0	0.001	0.012
DC06EK	0.007	0.027	0.027	0.130	0.009	0.006	0.050	0.022	0	0.102	0.020

Figure 1-5 : Sheet metals purchased by EIMS.

1.5.2. Steps of manufacturing a bathtub at the EIMS

The production of bathtubs involves three main steps (03 chains):

- Deep-drawing Chain,
- Welding Chain,
- Enameling Chain.

1.5.2.1. Deep-drawing Chain

- Deep drawing:

At EIMS, the production of bathtubs primarily involves the deep drawing process. However, before the actual deep drawing operation, the metal sheet (blank) is loaded onto the press using a blank loader assisted by a vacuum pump that creates a vacuum between the suction cups and the blank (Figure 1-6). The blank is then transported to the deep drawing press (named BZE1600-32) using a motorized system with a rack and pinion mechanism. This loading process ensures proper placement and fixation of the blank

before the deep drawing operation begins. The vacuum-assisted blank loader enhances efficiency and accuracy, allowing for seamless production of high-quality bathtubs at the EIMS facility.

Figure 1-6 : BZE1600-32 press for deep-drawing bathtubs.

The BZE1600-32 press is a large hydraulic machine (Figure 1-6) with a force of 1600 tons (600 tons for the punch and 1000 tons for the blank holder). This type of press represents a significant investment and is typically purchased for a lifespan of around forty years of operation. The press consists of a slide controlled by seven cylinders: six cylinders for the blank holder, one cylinder for the punch, and one ejector cylinder for the bathtub located below the die. Three pumps are used to supply these cylinders. The pressure generated by each pump is as follows:

- The blank holder pump (0-1000 bar).
- The slide pump (0-600 bar).
- The ejector pump (0-50 bar).

The BZE1600-32 press is a heavy-duty machine designed to handle high-force deep drawing operations and is a crucial asset for the production of bathtubs and other products at EIMS.

In this same press, a lubricant type TORJAN 460 – G006 [9] is injected between the die and the blank via an electro-pneumatic lubrication system. Lubrication is also carried out manually between the blank and the blank holder given the aging of the deep drawing tools (die, punch and blank holder). The intention is to facilitate the flow of the blank under the clamping effect of the blank holder. This lubrication operation is crucial for the success of the deep drawing process.

Lubrication helps reduce friction between the blank and the die, preventing undesirable material sticking to the die and minimizing the risk of excessive wear. By facilitating the movement of the material, lubrication also improves the quality of the deep drawn parts, reduces stress on the tooling, and extends the lifespan of the die and other system components.

In summary, the electro pneumatic lubrication is a vital step to ensure an efficient deep drawing process, providing high-quality finished products, and increasing the durability of the equipment used in bathtub manufacturing at EIMS.

After lubrication operation, the blank holder presses the blank against the die with different pressures while simultaneously cutting the four corners. After the blank is securely held, the punch descends to give shape to the bathtub. When it reaches the end of its stroke, it ascends along with the blank holder, and the bathtub is automatically ejected by the ejector mechanism. This sequential process ensures the efficient and automated production of bathtubs, and the resulting products are ready for further processing or distribution.

- <u>Cutting, Clipping, Falling edges</u>:

After the deep drawing operation, an electrically controlled rack and pinion system, along with clamps (single-acting pneumatic cylinders), are used to transport the bathtub and position it onto the ejector of the second press (BZE 600-32). This transfer

system ensures smooth and precise handling of the deep drawn bathtubs, allowing them to be seamlessly moved to the next stage of the production process, where further operations or finishing touches may be carried out using the BZE 600-32 press.
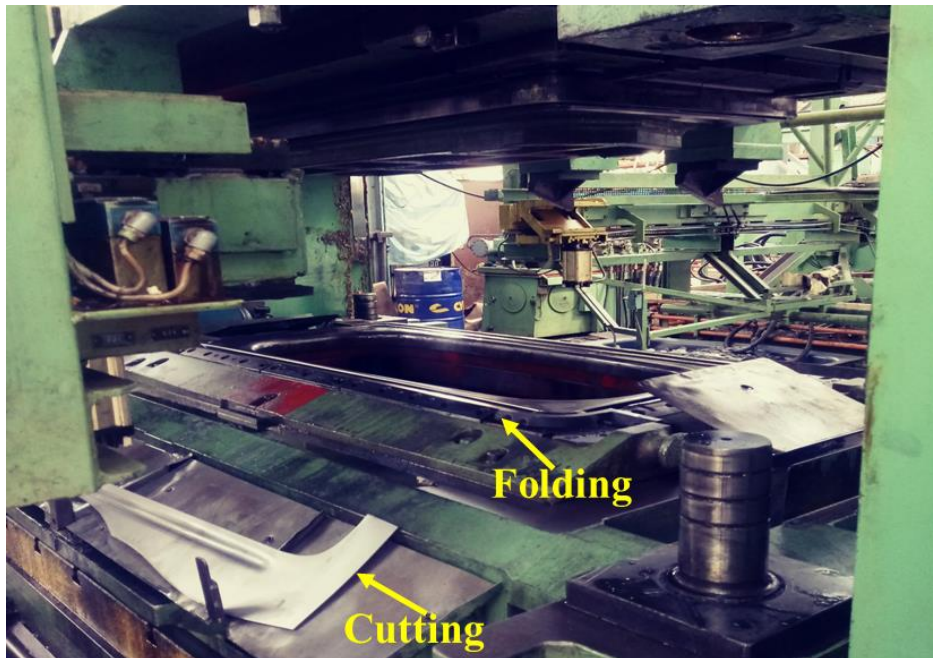
Figure 1-7 : BZE 600-32 press.

The BZE 600-32 press (Figure 1-7) is specifically designed for the cutting and edge clamping of the bathtub. This is achieved through the downward movement of a slide, which is controlled by a double-acting hydraulic cylinder operating at a pressure of 400 bar. Once the cutting process is completed, the slide ascends, and the bathtub is ejected from the press.

The cut-out pieces obtained from the cutting process will be used for manufacturing bathtub accessories. These accessories may include various components or additional features that complement and enhance the functionality of the bathtub. Recycling these cut-out pieces for accessory production helps optimize material usage and reduces waste, contributing to a more sustainable manufacturing process.

Edge folding, punching holes too full and emptying holes:

Once again, the bathtub is transported and positioned onto the ejector of the edge folding machine. This transfer is carried out using the same electrically controlled rack and pinion system and clamps (single-acting pneumatic cylinders) as mentioned before. This reliable and automated transfer system ensures a smooth and precise handling of the bathtub, enabling it to be accurately positioned for the edge bending process.

By utilizing the same transfer system, the manufacturing process maintains efficiency and consistency in handling the bathtubs, ensuring that they are properly positioned for the edge folding operation. This streamlined approach contributes to the overall productivity of the production line at EIMS.
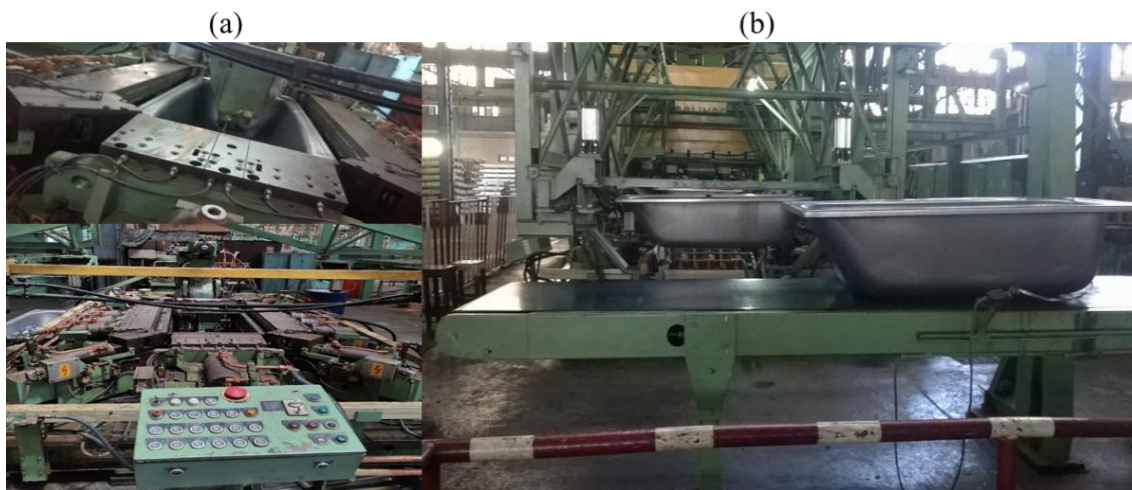
Figure 1-8 : (a) Edge folding machine, (b) Conveyor belt.

The edge bending and punching of the two (2) drainage holes in the bathtub are carried out by the machine illustrated in Figure 1-8 (a). This operation is performed using 12 hydraulic cylinders to form the edges of the bathtub and two punches to create the two drainage holes. Once these operations are completed, the bathtub is ejected again, and with the same transfer system, it is transported and positioned on a conveyor belt (Figure 1-8 (b)) for the welding of fixing tabs and lifting ears.

1.5.2.2. Welding Chain

The conveyor belt serves as a means to move the bathtubs to the welding station, where fixing tabs and lifting ears are securely welded onto the bathtub's structure. These welded components are essential for the proper installation and handling of the bathtub

during its usage. The use of a conveyor belt streamlines the process, allowing for efficient and continuous movement of bathtubs through the different stages of production at EIMS.

Figure 1-9 : Welding zone.

In the welding section (Figure 1-9), the various tasks to be performed are as follows:

- Welding of transport ears on the left and right sides of the bathtub.
- Welding of the fixation tabs for bathtub feet.
- Placing the bathtub, along with the welded components, onto the conveyor belt at the welding station's exit.
- Visual inspection and repair of any defects.

1.5.2.3. Enameling Chain

Once the manufacturing operations on the bathtub are completed, the bathtub is transported on the same conveyor belt to the enameling workshop. At the enameling station, the bathtub will undergo the enameling process, which involves the application

of a protective and decorative enamel coating to the surface, giving the bathtub its final appearance and enhancing its durability and aesthetic appeal.

The enameling workshop is divided into three (03) lines:

- Bathtub Cleaning Line:

In this enameling phase (Figure 1-10-a), the bathtubs undergo degreasing and cleaning to remove impurities, and finally, they are dried with hot air.

- Mass Coating Line (Ground-coat enamel):

After cleaning, the bathtubs are unhung and transferred to the transport conveyor to pass through the coating cabin. In this phase (Figure 1-10-b), both the front and back surfaces of the bathtub are coated with a layer of enamel with a tolerance between 80-120μ. The drying process follows, as the enameled bathtubs are transferred to the oven for baking. The baked surface condition is eventually checked at the end of this line.

- Covering Line (Cover-coat enamels):

In this phase (Figure 1-10-c), the front surface of the bathtub is coated with a covering enamel layer with a tolerance between 80 and 120μ. A drying operation follows in an oven at a temperature between 820 and 840°C to obtain the finished bathtub (Figure 1-10-d). The surface condition is checked at the end of this line.

Figure 1-10 : Enameling Chain.

After the enameling process is finished, the bathtubs are ready for quality control checks and any necessary final touch-ups before being prepared for distribution and sale.

Finally, the finished bathtub product is stored on wooden pallets for delivery to the commercial department. These well-organized lines ensure a smooth and efficient enameling process, resulting in high-quality bathtubs ready for distribution and sale.

1.5.3. Failure modes
1.5.3.1. Defects in deep drawing

In an increasingly competitive industrial context, manufacturing costs and lead times are two crucial factors. In the case of forming processes such as deep drawing, acceptance criteria can be diverse. They relate to issues of mechanical strength, dimensional tolerances, and surface quality. Due to the very principle of deep drawing, producing a part involves a compromise between shrinkage and expansion deformations, with their respective limits being the phenomena of wrinkling and those of striction and/or rupture, which are the fundamental rejection criteria. However, additional reasons for rejection can also be considered, including dimensional tolerances, springback, and surface appearance.

Figure 1-11 : Defects on the bathtubs.

Reducing the number of rejected pieces for time and cost savings is crucially important. In the manufacturing of bathtubs, various types of defects can be observed, as illustrated in Figure 1-8. These defects include:

Rupture: characterized by the presence of a fracture or tearing in the final deep drawn product (Figure 1-11-a). It is worth noting that, a visible striction essentially has the same meaning as a rupture, as both phenomena are closely related in terms of deformation. A rupture can originate from a local striction.

Both of these defects can occur due to tensile and compressive stresses. These stresses may become excessive in certain critical regions, leading to a rupture in those areas. Rupture can occur either at the beginning or during the forming operation. It is typically the result of poor control of blank holder pressure (or force) and/or ineffective

unlubricated contact, causing excessive frictional force and inappropriate deep drawing ratio that does not suit the formability of the material being used.

Wrinkling: refers to the appearance of undulations on the deformed part during forming processes (Figure 1-11-b). These are shape defects caused by one or more compressive stresses. Wrinkles can occur in both the elastic and plastic strain regions. They are often associated with deformations under compression and may appear in areas of the blank that are temporarily not in contact with the die or punch, as well as under the blank holder. They can result from the forming stresses themselves or from residual stresses released after the punch is withdrawn and the product is extracted from the die. In practice, wrinkles are more likely to occur when the material undergoes plastic strain during the forming process. It can also appear in areas of the part without contact with the tools of the deep drawing process (punch, die, and blank holder). Wrinkling occurs in the following situations [10]:

- Low blank holder pressure.
- Very small dimensions of the punch compared to the dimensions of the die (significant gap between the die and punch).
- Existing wrinkles or defects in the tools.
- Large distance between the blank holder and the die.
- Excessive lubrication.

Surface defects: can be classified into two categories (Figure 1-11-c) [11]:

Accidental defects (dents, scratches, various markings): These defects are related to incidents that occur during the setup of the sheet metal and/or during the forming operation. Prevention of these defects requires careful preparation and maintenance of all production tools (cleanliness of tools, appropriate manipulators, and storage pallets).

Systematic defects: These defects are related to non-uniform deformation or metal slippage on the entry radius of the die, directly resulting from choices made during the design of the process. The acceptability of these defects depends on their visibility on the finished product.

1.5.3.2. Defects during firing

During the vitreous enamel firing process, there is a phenomenon known as firing strain, where the steel sheet undergoes different degrees of distortion and strain. This is due to the transformation of the iron crystal structure from ferrite to austenite during firing. It is essential to be mindful of this occurrence. Firing strain can be observed in ultra-low carbon steel, but its effects are relatively less pronounced compared to low carbon steel [7].

1.5.3.3. Air bubbles - Black Spots

Figure 1-12 : Bathtub with air bubble defects.

Large air bubbles can form near the surface of the vitreous enamel layer, potentially compromising its corrosion resistance and surface quality. To prevent this defect (Figure 1-12), it is crucial to use steel that is suitable for enameling and to carefully manage the processes of degreasing, neutralization, firing, and ensuring the glaze is free from impurities.

1.5.3.4. Poor Adhesion

The bonding of enamel to bare steel is accomplished through chemical reactions occurring during the firing and cooling processes. This reaction involves the interaction between metal oxides in the enamel coating and the steel surface. Carbon plays a crucial role in securing enamel adhesion, but excessive carbon content can negatively impact the enamel's surface appearance due to the emission of gaseous CO and CO_2 during firing [8].

Poor adherence of the enamel significantly degrades the quality and can lead to the quick deterioration of the steel/enamel composite. Various factors can cause poor adherence, including unsuitable steel grades, inadequate pre-treatment, using enamels with insufficient cobalt or nickel oxide content, and incorrect firing times, whether too short or too long [12].

1.5.3.5. Fish scale defects

Fish scales are defects related to steel that manifest as half-moon-shaped cracks on the surface or cover coats, appearing immediately or even hours or days after the firing process. Several factors contribute to the occurrence of fish scales [8], [13]:

- The primary cause lies in the difference in coefficients of expansion between the enamel and the steel sheet. The coefficient of expansion for steel is higher than that of enamels, leading to compressive stress in the latter. Influencing factors include:

    - Enamel composition, which affects its coefficient of expansion.
    - Overfiring, causing volatilization of substances that maintain a high coefficient.
    - Lack of annealing for enameled ware, which should be treated as glass.

- Factors affecting enamel strength and adhesion to metal:

- The physical condition of the metal surface influenced by drawing, spinning, cold rolling, or other mechanical treatments.
- Glass composition impacting its elastic strength.
- Underfiring, where enamel does not fuse properly to metals.
- Surface cleanliness, regarding the removal of drawing compounds, grease, etc.

- Fish scales (Figure 1-13) can result from hydrogen diffusion through the steel and into the enamel layer, typically occurring on pieces enameled on both sides. Hydrogen forms at the steel surface during firing, leading to atomic hydrogen diffusion into the steel, eventually recombining as hydrogen gas (H_2). As the enamel solidifies, the solubility of hydrogen decreases, causing hydrogen molecular migration towards the enamel/steel interface, creating high local pressure spots. This results in enamel blisters and the appearance of fish scale defects [6]. The hydrogen formed at the steel surface during firing according to the reaction:

$$Fe + H_2O \rightarrow FeO + H_2 \qquad (c)$$
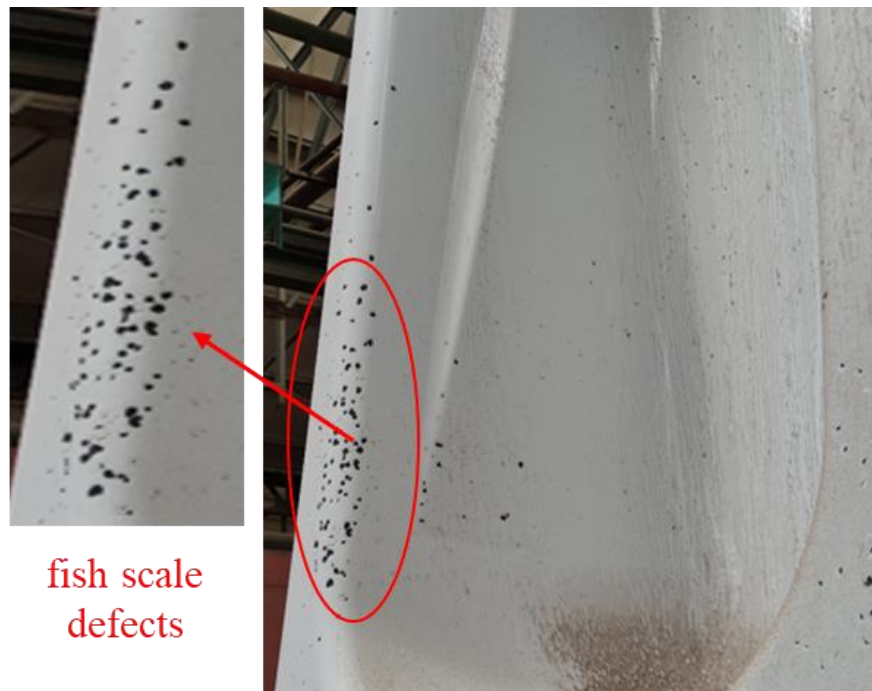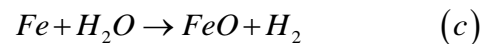
Figure 1-13 : Bathtub with fish scale defects.

Influencing factors:

- Humid chamber atmosphere.
- Insufficient drying of wet enamel.
- Steel not suitable for enameling.

Remedies:

- Use a steel suitable for enameling with sufficient hydrogen trapping capacity.
- Check enameling conditions.

Hydrogen trapping [6]:

- **Physical** micro cavities around large cementite precipitates (Fe_3C) or inclusions (MnS), during cold rolling.
- **Chemical** in steels containing titanium or boron.

Formation of hydrides:

Formation of hydrogen-trapping precipitates, the most effective being TiC (other: TiN, TiS, $Ti_4C_2S_2, ...$).

1.6.   *Problematic of the numerical simulation of the deep drawing of the bathtub*

Indeed, the application of the deep drawing process is becoming more appealing, and recent research aims to improve it by:

- Reducing production costs: Researchers strive to develop methods and techniques to optimize material usage, reduce waste, and minimize machine downtime, thereby reducing manufacturing costs.
- Increasing production rates: The objective is to enhance the speed and efficiency of deep drawing while maintaining high-quality output. This may involve using faster presses, automating the process, and enhancing tooling.

- Eliminating defects that may occur during or after forming: Defects like wrinkles, fractures, or surface imperfections are thoroughly studied. Researchers aim to identify the root causes of these defects and develop solutions to prevent or correct them.

- Obtaining lighter-weight components: Research focuses on designing components with optimal thickness and employing lighter materials while retaining required mechanical properties. This results in lighter products without compromising their strength and durability.

To successfully manufacture a deep drawn product, it is crucial to control all the elements and factors that influence the process. Finding the optimal combination of various process parameters remains a significant challenge for both industrialists and researchers. Experimental testing methods may not always lead to the desired success in the final product. To meet industrial requirements, researchers and engineers often turn to numerical simulation, which has become an indispensable tool to overcome encountered issues such as wrinkling, rupture, surface defects, etc.

Numerical simulation allows for the faithful reproduction of mechanical forming operations with high precision and efficiency, reducing time and cost in the design and development phases, leading to the production of new products and articles. Starting from the design stage and throughout the conception phase, numerical simulation serves as an analytical and design aid tool. It helps to qualitatively and even quantitatively evaluate the feasibility challenges of components, relative to the specifications.

To numerically simulate a forming operation like sheet metal deep drawing in a numerical calculation code (Figure 1-14), we must model not only the process itself (geometry, tool actions on the part, thermal aspects, etc.) but also provide the code with:

- Elastoplastic behavior laws describing the material's behavior when mechanically loaded during forming.

- A forming limit curve describing the material rupture during forming.

- A tribological behavior law expressing solid-solid contact, whether dry or lubricated.
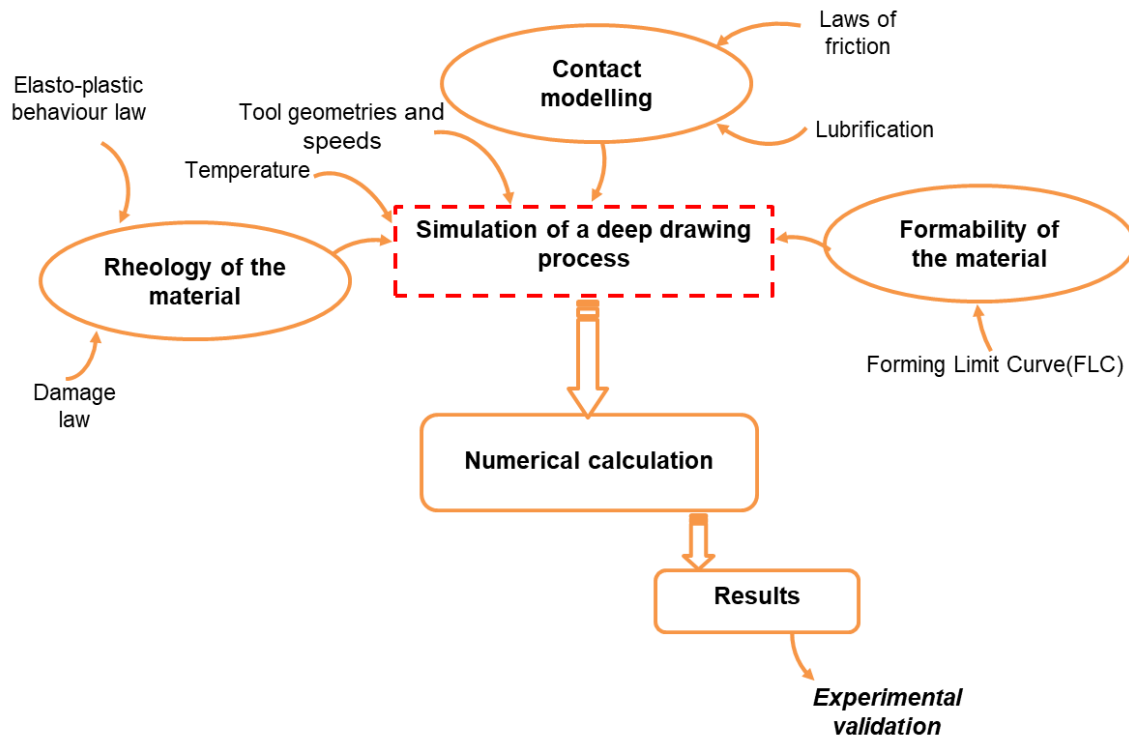
Figure 1-14 : Modelling of a deep drawing operation [10], [14]**.**

The objective is to conduct a numerical simulation of the bathtub extra-deep drawing process, using real dimensions and operating conditions. For this purpose, we have obtained a drawing of a bathtub produced by the EIMS company, with the operating conditions set directly on the deep drawing press, and some measurements that will be relevant for numerical simulation. However, the use of the numerical approach requires a good knowledge of the elastoplastic behavior laws of the sheet metal material and a good evaluation of its formability.

1.6.1. Elastoplastic behavior of sheet metals

The characterization of the elastoplastic behavior of a sheet metal first requires a good modeling of the hardening law and the yield criterion of its constitutive material. In the plastic domain, the hardening curve reflects the evolution of the stress level in the material as a function of the level of strain achieved. The yield criterion is a mathematical description of a yield surface in stress space. This yield surface represents the initial and

current boundary from which plastic flow can occur. Therefore, it is necessary to incorporate good modeling of the hardening curve and the yield criterion into the finite element code to ensure the reliability of the forming process simulation. The success of the forming operation will be particularly evaluated using a forming limit curve (FLC), specific to each material, which qualifies its formability and identifies areas that may be prone to necking prior to rupture. Several families of yield criteria and hardening curves are presented in this section, along with a brief literature review concerning FLC.

1.6.1.1. Elasticity

Elasticity refers to the ability of a material to regain its original shape after the removal of the force that caused the deformation. Hooke's Law, which defines the linear relationship between stress (σ) and elastic strain (ε), is the fundamental equation for describing the elastic behavior of a material. This law is given by the following equation:

$$\sigma = E \cdot \varepsilon \qquad \qquad 1\text{-}1$$

For an isotropic material, an axial stress generates an axial strain ε_{xx} and a transverse strain $\varepsilon_{yy} = \nu \times \varepsilon_{xx}$.

1.6.1.2. Plasticity

If the stress applied to a material exceeds a certain critical value, called the yield point or elastic limit, the deformation of the material becomes irreversible. To describe the plastic behavior of a material, a yield criterion and a hardening law are needed.

Several anisotropic yield criteria have been proposed to model metal sheets. The most commonly used criterion is Hill48. It was proposed by Hill in 1948 as a modified form of the Von Mises criterion. For a plane stress loading, the out-of-plane stress tensor components ($\sigma_{zz} = \sigma_{xz} = \sigma_{yz} = 0$) are neglected. In this case, the number of Hill's parameters is reduced to four, and the criterion becomes [10], [14]:

$$\overline{\sigma_H} = \sqrt{\sigma_{XX}^2 \left(H + G \right) + \sigma_{YY}^2 \left(H + F \right) - 2H\sigma_{XX}\sigma_{YY} + 2N\sigma_{XY}^2} \qquad \qquad 1\text{-}2$$

$\overline{\sigma}_H$ is the Hill equivalent stress, and F, G, H, and N are Hill's parameters that determine the shape of the yield surface and the degree of its anisotropy.

___

$$F = \frac{r_0}{r_{90}(1+r_0)} \quad , \quad G = \frac{1}{1+r_0}, \quad H = \frac{r_0}{1+r_0}, \quad N = \frac{(1+2r_{45})(r_0+r_{45})}{2r_{90}(1+r_0)} \qquad 1\text{-}3$$

The identification of the above parameters requires three tensile tests at angles of 0°, 45°, and 90° relative to the rolling direction to measure the three Lankford coefficients (r_0, r_{45} and r_{90}) [14].

The Lankford coefficients reflect the ratio between transverse plastic strain and that in the thickness and are calculated as follows:

$$r_\theta = \frac{\varepsilon_w}{\varepsilon_t} \qquad 1\text{-}4$$

Under the assumption of constant volume plastic strain, the principal strains in the uniaxial tensile specimen can be written as follows:

$$\begin{cases} \varepsilon_l = \ln\left(\dfrac{l_0}{l}\right) \\[2mm] \varepsilon_w = \ln\left(\dfrac{w_0}{w}\right) \\[2mm] \varepsilon_t = -\left(\varepsilon_1 + \varepsilon_2\right) \end{cases} \qquad 1\text{-}5$$

When a material is subjected to stresses beyond its elastic limit, it begins to exhibit plastic behavior. This means that the material deforms permanently and irreversibly and does not return to its original shape and size even after the load is removed. In this state, the relationship between stress and strain is no longer proportional. They are related by empirical laws, called hardening laws, which can take various forms. In the literature, there are numerous laws formulated with a highly variable number of parameters. The main hardening laws used are illustrated below [10], [14]:

- The Hollomon law (power law) is the simplest and most commonly used; it is given in the form:

$$\sigma = K \cdot \varepsilon^n \qquad 1\text{-}6$$

To identify the parameters K and n, the curve (σ-ε) is transformed into a linear curve ($\ln(\sigma)$-$\ln(\varepsilon)$). The slope of this curve gives the value of the coefficient n, called the hardening exponent. For cases of low plastic strain, this law has some limitations in describing hardening [15].

- The Ludwik law is given in the form:

$$\sigma = \sigma_0 + K \cdot \varepsilon^n \qquad \text{1-7}$$

- The Swift law (Krupkowski law) is expressed in the form:

$$\sigma = K \left(\varepsilon_0 + \varepsilon \right)^n \qquad \text{1-8}$$

- The Voce law is more suitable for describing aluminum alloys and brass. It is expressed in the form:

$$\sigma = \sigma_S - \left(\sigma_S + \sigma_0 \right)^{-\alpha s} \qquad \text{1-9}$$

For large deformations, the stress tends towards a limit $\sigma = \sigma_S$.

1.6.2. Forming limit curve

The FLC define the capacity of a material to be deformed in different stress modes (from "full sheet" deformation to deep drawing with forward forming). For each of these modes, the limit is marked by the appearance of localized thinning (necking prior to rupture) and wrinkling [16].

The FLC for the DC06EK sheet metal with 1,6 mm thickness, used for evaluating the formability of the deep-drawn bathtub, was established by Belguebli et al. [16] through the Keeler and Brazier model [17], [18]. Keeler and Brazier model is used for predicting the formability of DC06EK sheet metal. This model is expressed as a function of sheet metal thickness « t_0 » and work hardening coefficient « n » to determine the FLC for mild steels. The variable considered is the position of the lowest point of the FLC, located on the plane strain trajectory, denoted FLC_0. According to this model, the FLC is determined as follows:

FLC$_0$:

$$FLC_0 = \ln\left(\frac{n}{0.116}(0.2325 + 0.1413t_0) + 1\right)$$

1-10

Left side of the FLC:

$$\varepsilon_1 = FLC_0 - \varepsilon_2$$

1-11

Right side of the FLC:

$$\varepsilon_1 = (FLC_0 + 1)(\varepsilon_2 + 1)^{0.5} - 1$$

1-12
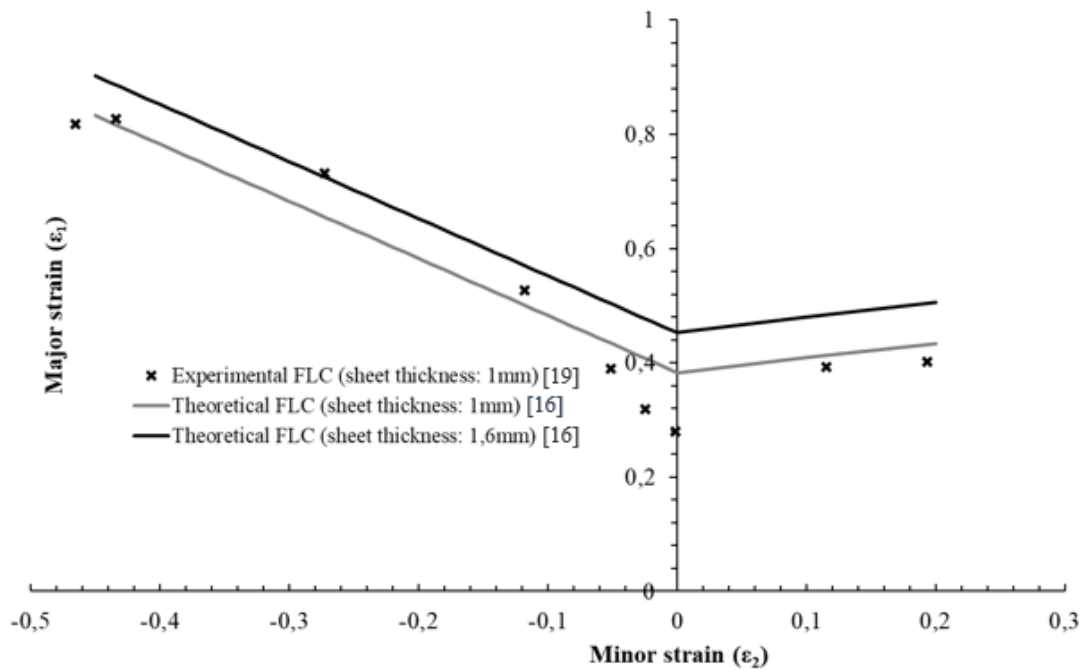
Figure 1-15 : Comparison between the theoretical FLCs of different thicknesses with that obtained experimentally by [19] for the DC06EK sheet metal.

Using the equations above, two theoretical FLCs are obtained for the both DC06EK sheet metal thicknesses of 1mm and 1,6mm. These latter are compared with the experimental FLC in the Figure 1-15. Punch stretch tests following the Nakazima method are used to obtain the experimental FLC of DC06EK with a sheet thickness of 1mm [19]. The comparison shows a good agreement between experimental and theoretical FLCs for

sheet thickness of 1mm. Note that the CLF increases for the thickness of 1,6mm which is used in this work.

1.7.   Conclusions

At the EIMS company, cold deep drawing is widely used to manufacture household appliances and sanitary products. However, scrap production has increased as a result of rupture and wrinkling defects during the deep drawing operation and the appearance of fish scale defects after enameling. These defects lead to significant losses in terms of cost and time. To mitigate these losses, researchers and engineers are turning to numerical simulation. Reproducing a deep drawing operation in a numerical model requires the integration of the elastoplastic behavior of the material, its formability and a law describing the contacts between the blank and the tool.

To contribute to the numerical simulation of the deep drawing operation of a bathtub with real dimensions and operating conditions, experimental characterization of the two sheet metals (DC06EK and DC05EK) and 3D measurements of tools and defect-free bathtub are needed.

The excessive number of rejects in enameled products, particularly bathtubs 1400, after manufacturing through extra-deep drawing of the DC06EK steel sheet, has become a significant issue. This problem is primarily attributed to the appearance of fish scales (or nail marks) on the sanitary products. The occurrence of this phenomenon occurs a few days after the enameling operation of the deep drawing product. Furthermore, the rising costs, acquisition challenges, and concerns about the quality of imported sheet metal (DC06EK) have further exacerbated the situation. An experimental study is required to analyze the occurrence of fish scales in enameled sanitary product by investigating induced strain heterogeneity and anisotropy in the deep drawing process of the DC06EK sheet. And we have also carried out experiments to discover the relationship between corrosion and fish scale According to the level of deformation that occurs during the deep-drawing process of the bathtub for the two materials DC05EK and DC06EK

.

Chapter 2.   Materials and Experimental Methods

2.1.   Introduction

In order to guarantee the durability and safety of sanitary products over a long period of time, it is necessary to improve the structural and mechanical properties of the material used for deep drawing in EIMS. In this chapter, the DC06EK and DC05EK sheet materials are analyzed and mechanically tested, and the experimental means and approaches are presented and detailed. A physicochemical characterization was carried out using techniques such as a spectrometer for the chemical composition of the materials, and optical microscopy for metallographic analysis. Tensile tests were then carried out for three orientations with respect to the rolling direction, and a tribology test to deduce the coefficient of friction. Finally, a corrosion test was carried out for both materials. To contribute to the numerical approach in Chapter 3, 3D and ultrasonic thickness measurements were carried out on a bathtub manufactured without defects.

2.2.   Analysis of the chemical composition

Table 2-1: Chemical compositions of DC05EK steel.

Element	C	S	N	Mn	P	Si	Al	Ni	V	Ti	Cr
Annex 3 (EIMS)	0.050	0.025	0.072	0.180	0.008	0.005	0.034	0.019	0	0.001	0.012
Sample 01	0.0334	0.0253	-	0.203	0.0002	0.0064	0.0169	0.0174	0.0057	0.0029	0.0150
Sample 02	0.0327	0.0185	-	0.201	0.0002	0.0059	0.0161	0.0169	0.0057	0.0024	0.0150

Table 2-2: Chemical compositions of DC06EK steel.

Element	C	S	N	Mn	P	Si	Al	Ni	V	Ti	Cr
Annex 3 (EIMS)	0.007	0.027	0.027	0.130	0.009	0.006	0.050	0.022	0	0.102	0.020
Sample 01	0.014	0.0119	-	0.280	0.019	0.012	0.030	0.050	0.0035	0.048	0.011
Sample 02	0.011	0.0156	-	0.305	0.021	0.013	0.036	0.048	0.0029	0.047	0.012

As part of laboratory testing, the determination of chemical composition by spark-source optical emission spectrometry is a quick and easy test to implement to validate the conformity of a part in relation to a product standard or a particular specification, or to determine the nature of the part. This technique is also widely used in industry. To obtain

the chemical components for DC05EK and DC06EK, we carried out a quantitative analysis using a spectrometer at ORSIM company in Oued Rhiou.

Chemical characterization has confirmed that a large quantity of uniformly dispersed particles containing (Ti, N), (Ti, S), (Ti, C, S), and (Ti, C), precipitate in the steel, acting as irreversible hydrogen traps and contributing greatly to its exceptional resistance to fish scaling [19]. Compared with DC05EK, it is richer in these chemical compounds, making it more resistant to the occurrence of this phenomenon (Table 2-1 and Table 2-2).

The roles of titanium (Ti), sulfur (S), carbon (C), and nitrogen (N) in influencing both corrosion resistance and the occurrence of fish scale defects in DC06EK and DC05EK steels are explained below [20], [21]:

The careful balance and control of titanium (Ti), sulfur (S), carbon (C), and nitrogen (N) in DC06EK and DC05EK steels lead to improved corrosion resistance and a significant reduction in fish scale defects. Titanium acts as a stabilizer, sulfur is minimized to prevent harmful inclusions, and carbon and nitrogen are controlled to avoid the formation of detrimental carbides and nitrides. This optimized composition ensures that the steels maintain their desired properties for applications requiring high formability, surface quality, and resistance to both corrosion and surface defects.

2.3. Optical microscope metallographic analysis

Once the chemical composition of DC05EK and DC06EK steel is known, conducting a metallographic analysis is crucial to identifying the material's phases. The samples undergo several steps in this process, as detailed below:

2.3.1. Sample preparation

Prior to polishing, the samples are obtained by cutting the two sheet metals. These samples are then encased in epoxy resin mixed with a hardener using 25-mm-diameter molds. It takes approximately 20 minutes for the resin to solidify. Once the resin is ready, two samples are prepared for polishing, ensuring they are perfectly flat for clear qualitative analysis. The embedded samples are depicted in Figure 2-1 (a).

2.3.2. Polishing samples

Polishing is an essential step in metallographic analysis in Figure 2-1 (b), as a smooth surface is needed to observe the structure's microscopic details. Scratches and residual defects from metal cutting must be eliminated. The goal is typically a "mirror finish," meaning defects and scratches should not be visible under an optical microscope, with residual defects smaller than a micrometer. However, depending on the application, a surface that appears smooth to the naked eye or under a binocular magnifier is often sufficient. Additionally, polishing can remove the surface layer to reveal the core of the material, which may have different properties.

In this study, samples were prepared using a Struers RotoPol-35 polisher, which is a fully automated machine. This device allows for the adjustment of:

- The holding force applied to the samples (measured in Newtons) across various sample holders, powered by a compressor providing up to 6 bars of pressure;
- The rotation speed of the platen, adjustable from 150 to 300 revolutions per minute, on which different types of paper (abrasive and felt) are placed;
- The rotational direction of the sample holder in relation to the platen;
- The polishing duration;
- The lubricant supplies.

The sample holder can accommodate cylindrical samples with diameters between 20 and 50 mm. It is essential to place an appropriate number of samples in the holder to maintain balance during the polishing process.

2.3.3. Optical microscope

The optical microscope is an instrument with which most scientists are familiar. Since the end of the nineteenth century, it has been widely used to study materials. The Leica DM4 M microscope (Figure 2-1 (c)) and its acquisition and processing software were used to visualize the samples. The optical microscope is located in the rheology and mechanics laboratory at Chlef University (UHBC).

To determine the mechanical properties of DC06EK and DC05EK steel, it is important to start with a metallographic analysis, which consists of determining the phases that make up the material. After the samples have been cut and before the optical microscope analysis, they are polished with a chemical attack of 3% nital.

Figure 2-1 : (a) Samples before polishing, (b) Polishing samples, (c) optical microscope<<LEICADM4M>>.

2.3.4. Metallographic analysis

After visualizing the samples under the microscope, we began by comparing the microstructure obtained in this study for the two materials DC06EK and DC05EK. Figure 2-2 illustrates the images obtained by the optical microscope, which show a different metallography between the two samples DC05EK and DC06EK:

With regard to structure DC05EK, after examining the sample under an optical microscope, it became clear that two distinct colors were present: the light colour corresponds to perlite grains, while the dark color is associated with ferrite grains. According to the iron-carbon curve, this material lies in the ferrite-perlite region, which suggests the presence of significant quantities of carbon, favoring a balance in the two processes (deep drawing and enameling).

Concerning the DC06EK structure, the microstructure of the DC06EK reveals a predominance of dark colors and a notable absence of light colors compared with its predecessor. These dark colors are mainly present in the ferrite granules, which suggests that they belong to the ferrite phase according to the iron-carbon diagram. This

observation suggests a very low percentage of carbon in this material, which has a considerable influence on the enameling process, but it has good formability.
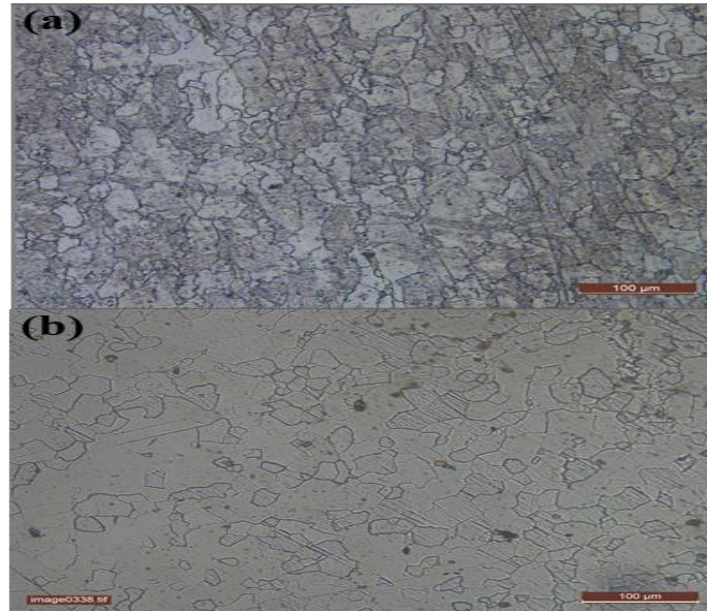
Figure 2-2 : Steel microstructure :(a) DC05EK, (b) DC06EK.

2.4. *Tensile tests*

2.4.1. Specimens used in tensile tests

The main aim of this work is to carry out mechanical tests with precision on the tensile testing machine, named "Gunt". Before carrying out this study, it is important to present the tensile tests and the mechanical characterization of materials based on these tests.

To characterize the behavior of DC05EK and DC06EK steel, uniaxial tensile tests were carried out in three directions relative to the rolling direction (0°, 45°, and 90°). The specimen was designed using SOLIDWORKS software in compliance with American standard ASTM E 08-2010 [22]. Then, the specimens were cut using the water-jet process following different rolling directions in a company based in Blida (Figure 2-3). The advantage of this process is the elimination of possible damage caused by heat, such as thermal stress, cracking, or structural hardening. The dimensions of the specimen are given (Figure 2-4).

Figure 2-3 : Cutting the test specimens with a water-jet.
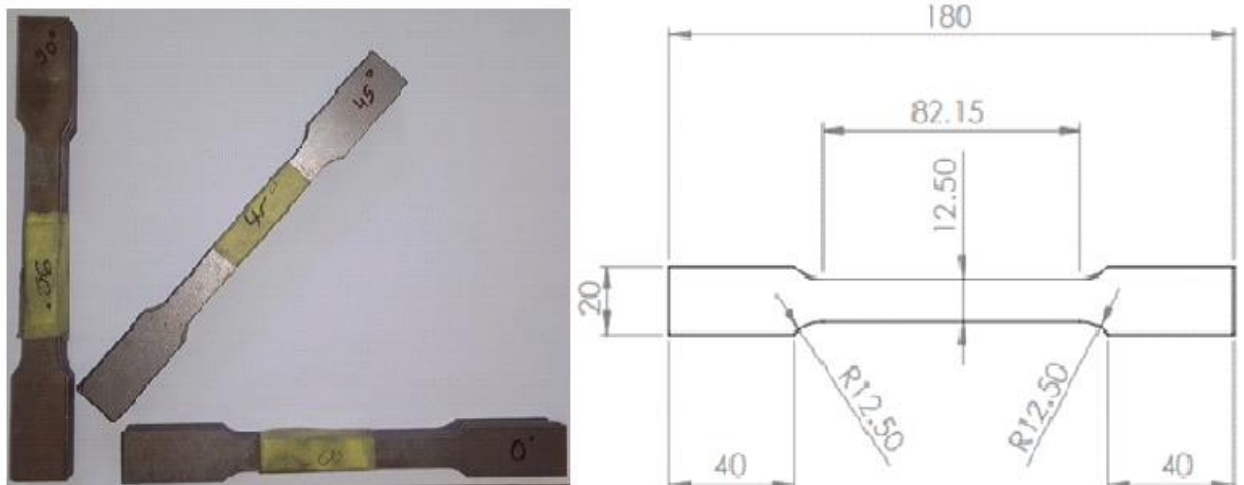
Figure 2-4 : Dimensions of specimens following ASTM E 08-2010.

2.4.2. GUNT WP 310 universal tensile test machine

The experiment involves installing the mooring system on the GUNT tensile testing machine at the strength of materials laboratory of Hassiba Benbouali University in Chlef. The GUNT WP 310 machine (Figure 2-5) is a versatile testing bench designed for conducting various mechanical tests, including tensile, compression, shear, three-point bending, and hardness tests. Its clear setup and user-friendly design enable detailed observation of each test phase. The machine is capable of performing tests that meet industrial standards.

The primary components of the machine include:

- 1 A hydraulic cylinder responsible for generating both tensile and compressive forces.
- 2 Operational areas equipped with the WP 310 accessory.
- 3 Force sensors incorporated into the system.
- 4 Adjustable lower crossheads with a locking mechanism for height adjustments.
- 5 Display and control elements for monitoring and managing the machine's functions.
- 6 Displacement sensors to track movement and position changes during testing.
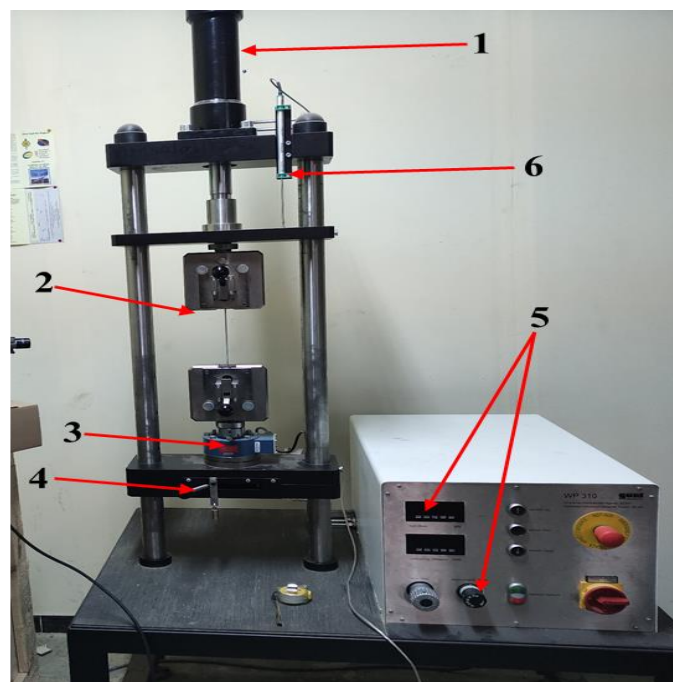
Figure 2-5 : Universal tensile test machine "Gunt".

2.4.3. Stress-Strain curve characterization

- **Elasticity**

The most obvious example of elastic deformation is a spring. Elastic deformation is reversible: the medium returns to its initial state when the stress is removed. Linear elasticity concerns small deformations proportional to the load. In this range, the elongation is proportional to the force in the case of stretching.

At higher strains, elasticity becomes non-linear for some materials (plastic strain). For others, fracture or creep occurs. Elastic deformation occurs at low stresses. If you increase the load, you change the mode of deformation:

- Plastic strain (irreversible and non-linear) followed by fracture for 'ductile' materials;
- Rupture (damage) for 'brittle' materials;
- Eventual creep for ductile materials if the rate of deformation is slow and/or the temperature is high [28].

Young's modulus

$$E = \frac{F}{\Delta L} \frac{L_0}{S_0} \quad = \quad \frac{\sigma}{\varepsilon} \qquad\qquad 2\text{-}1$$

The elastic limit (Re): Constraint beyond which Hooke's law is no longer valid.

- **Plasticity**

Plastic strain is the irreversible deformation of a part; it occurs through a rearrangement of the position of the atoms, when the stress exceeds elastic deformation and enters plastic strain. Some materials, known as 'brittle', break in this deformation mode if the stress is too great.

In the case of so-called 'ductile' materials, when the load is increased, the part is permanently deformed: when the load is stopped, the part remains deformed. This happens because the atomic planes slide over each other, like playing cards in a deck. This sliding of atomic planes is achieved by the displacement of localised linear defects called 'dislocations'.

The tensile strength (Rm): Stress corresponding to the maximum force on the tensile curve.

Relative elongation at break (in %):

$$A = \frac{\Delta L}{L_0} 100 \quad = \quad \frac{L_r - L_0}{L_0} \; 100 \qquad\qquad 2\text{-}2$$

Where L_r the breaking length measured by bringing the two pieces of the specimen together. Elongation is also defined as the elongation measured at the maximum of the tensile curve. It is of great interest; it is an essential parameter for assessing a sheet's suitability for forming.

- **Hardening curve**

The hardening curve based on the original or unchanged gauge length and cross-section is called the engineering stress-strain curve, while the hardening curve based on the instantaneous or variable gauge length and cross-section is called the true stress-strain curve.

In our study, the experimental force/displacement curves are transformed into true stress-strain curves using the classical analytical model based on the assumption of homogeneity of stress and strain in the central section of the specimen [23]:

- Engineering stress-strain curve

$$\sigma = \frac{F}{S} \qquad\qquad \varepsilon = \frac{\Delta L}{L_0} \qquad\qquad 2\text{-}3$$

Where: F is the measured force and $\dfrac{\Delta L}{L_0}$ is the relative elongation.

- True stress-strain curve

$$\sigma_{true} = \sigma(1+\varepsilon) \qquad\qquad \varepsilon_{true} = \ln(1+\varepsilon) \qquad\qquad 2\text{-}4$$

- Hardening coefficient

According to Ludwick's law

_____

$$\sigma = K \left(\varepsilon_p \right)^n \qquad\qquad \log \sigma = \ln K + n \ln \varepsilon_p \qquad\qquad 2\text{-}5$$

2.4.4. Analysis of results
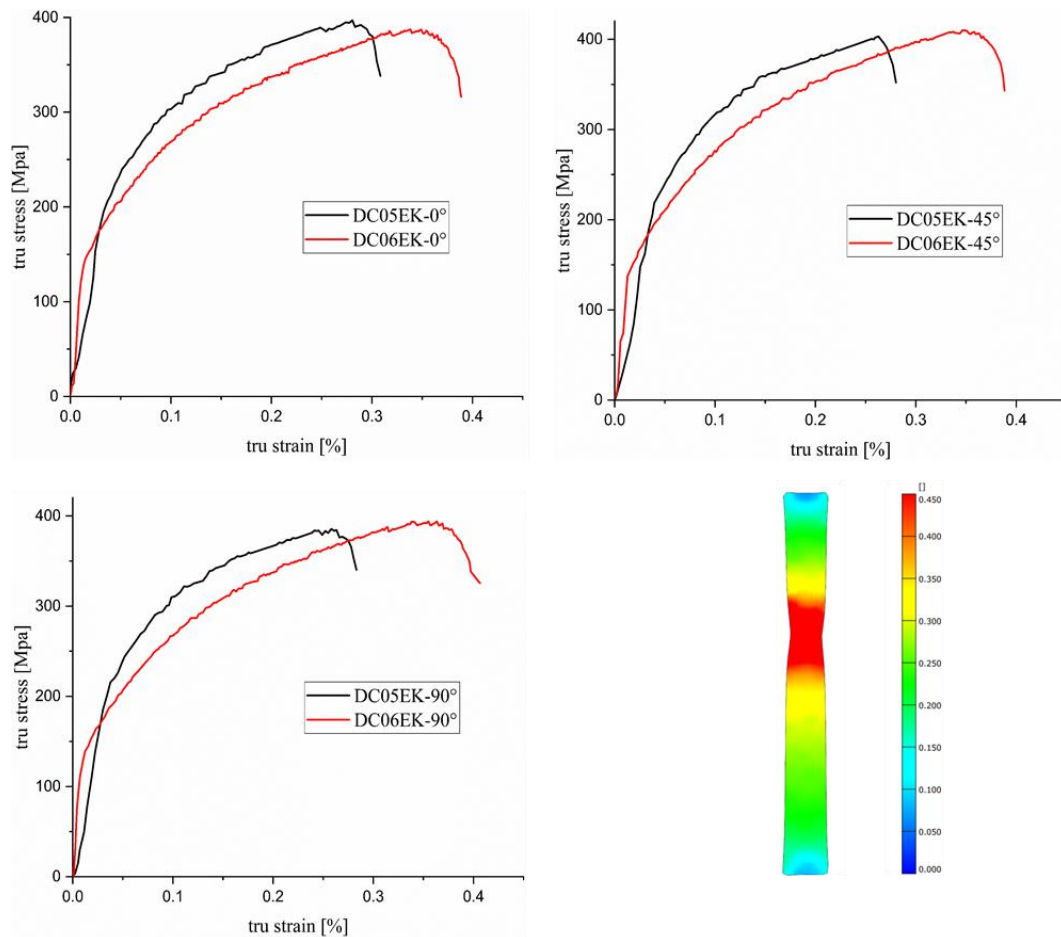
Figure 2-6 : Comparison of three true stress-strain curves for the DC05EK and DC06EK with respect to the different rolling directions (0°, 45° and 90°).

Figure 2-6 shows a comparison of three stress-strain curves selected for the three orientations (0°, 45° and 90°) for the two materials. It can be seen that there is a difference between the mechanical properties - elastic strength 'Re', maximum elongation 'A%', maximum strength 'Rm' and breaking points 'Rr' - for the two materials. This last parameter has a major influence on formability. **The DC06EK therefore has greater formability than the DC05EK**. These parameters are reported in Table 2-3.

Hardening curves are gathered for each material in Figure 2-7 for the three rolling directions. It can be seen that there is reproducibility of parameters for each material.

However, there is a difference in yield strength and fracture points for specimens at 0° and 45° to the rolling direction. There is no difference between the strain-hardening curves for 0°RD and 90°RD, but there is a difference between the strain-hardening curve for 45°RD and the other two curves. This material therefore appears to have a more or less pronounced anisotropy. We also note that there is a difference between the fracture points for the three curves. This difference can be explained in terms of the anisotropy and heterogeneity of the material.
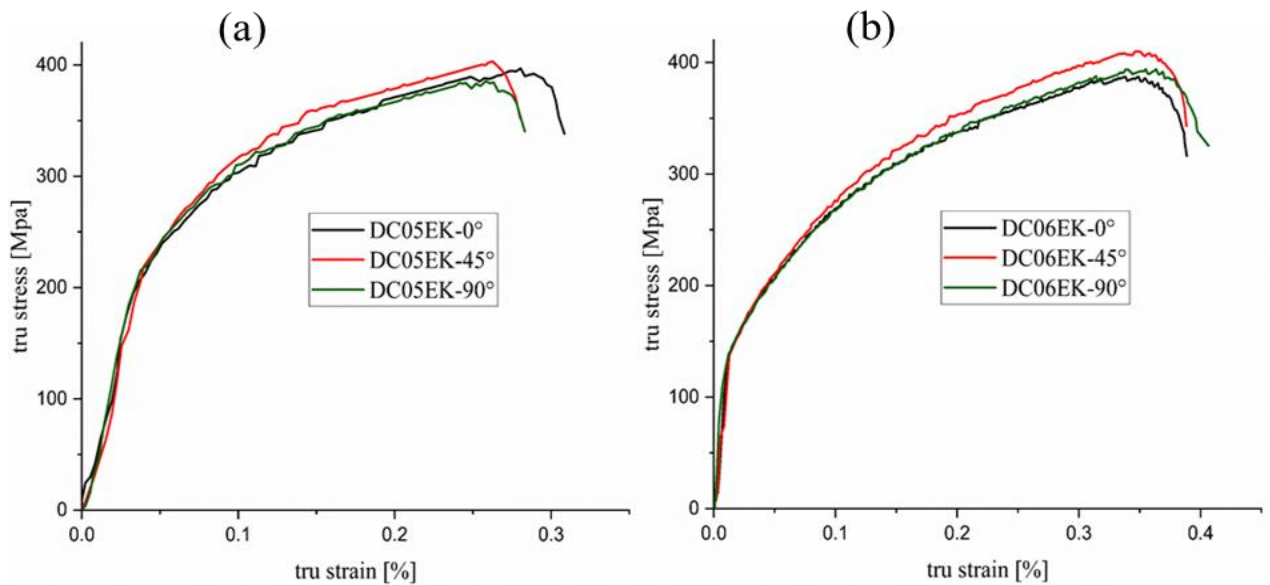

Figure 2-7 : (a) True stress-strain curve for DC05EK, (b) True stress-strain curve for DC06EK.

Table 2-3: Mechanical properties of DC05EK and DC06EK sheet metals.

Materials	DDL	Re [Mpa]	Rm [Mpa]	Rr [Mpa]	Elongation [%]
DC05EK	0%	160	380	375	30
DC06EK		130	375	360	36
DC05EK	45%	155	380	375	27
DC06EK		130	390	380	35
DC05EK	90%	160	375	370	28
DC06EK		130	375	375	37

2.5.   *Ball-on-disc tribometer*

A mineral oil-based type, TORJAN 460-G006, is used in the bathtub EDD process more precisely at the tool-blank contacts. The intention is to facilitate the flow of blank between the blank holder and the die. The coefficient of friction was determined according to the contact conditions encountered in the bathtub EDD process and was

evaluated using a ball-on-disc tribometer device (Figure 2-8-a). A specimen in disc form cut out from the received DC06EK sheet metal undergoes a rotary motion with a linear velocity of 1.5 mm/s while being brought into contact with a stationary ball of 6 mm in diameter to which an axial compressive load of 1 N was applied. The test was carried out in the same lubricated medium at room temperature. The coefficient of friction represents the ratio between the tangential force and the normal force. This coefficient as a function of a 200 mm contact distance is shown in Figure 2-8-b. The coefficient of friction at the tool-blank contacts is estimated to be approximately 0.13 based on this result.
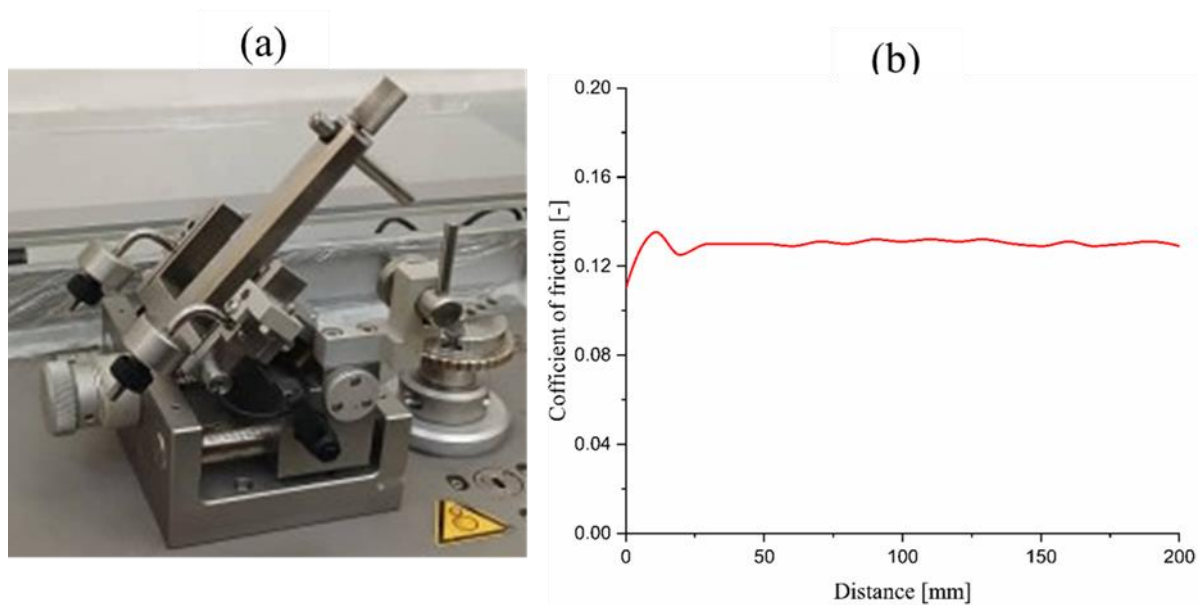

Figure 2-8 : (a) Ball-on-disc tribometer device, (b) Coefficient of friction vs. contact distance.

2.6. Measurements

2.6.1. 3D measurements

In recent decades, geometric modeling has become a valuable tool for various industrial applications such as the design of cars, boats, aircraft wings, etc. One of the methods of geometric modeling is reverse engineering or three-dimensional (3D) measurement. This method consists of making CAD (computer-aided design) drawings from a physical object. More precisely, reverse engineering is the fundamental concept of manufacturing a part based on its original or physical model without the use of a technical or industrial drawing. Reverse engineering is an activity that can be used in

several fields such as mechanical, electrical, civil, computer, medical, aeronautical, naval engineering [24], [25].

The 3D reverse engineering of part surfaces, by Coordinate Measuring Machines (CMM), makes it possible to give in a relatively short time an image of the 2D or 3D surfaces in the form of sets of points. From this set of points, geometric modeling software is used to form 2D and 3D surfaces and build the final shape of the desired object.

The objective is to scan a defect-free bathtub type "1400" with the reverse engineering method using a Romer Arm 3D laser scanner. This device is available at the CDTA (Center for Development of Advanced Technologies) situated at Baba Hassen, Algiers. This measurement method will be useful for deducing the real shape of the punch.

The important steps of the 3D measurement and scanning operation are illustrated in the following points:

Step 01: Cleaning and degreasing the bathtub using sandpaper to remove small grains and achieve a clean surface before proceeding with the scanning of the bathtub. It is important to note that this operation requires special care to avoid damaging the surface of the bathtub and reducing its thickness since this geometric parameter will be used as a reference for comparison with an ultrasonic thickness measurement, as illustrated in the "Experimental validation" section (§2.6.3).

Step 02: Spraying the surface of the bathtub to be measured with a liquid product such as SHERWIN (Figure 2-9). The purpose of this operation is to achieve good reflection of laser rays towards the data reception sensor of the device (ROMER scanner).

Figure 2-9 : SHERWINE liquid.

Step 03: This step consists of two parts:

The first part involves the scanning operation using the ROMER device. A reference plane, table (Figure 2-10), is used to initiate the scanning operation of the bathtub surface.
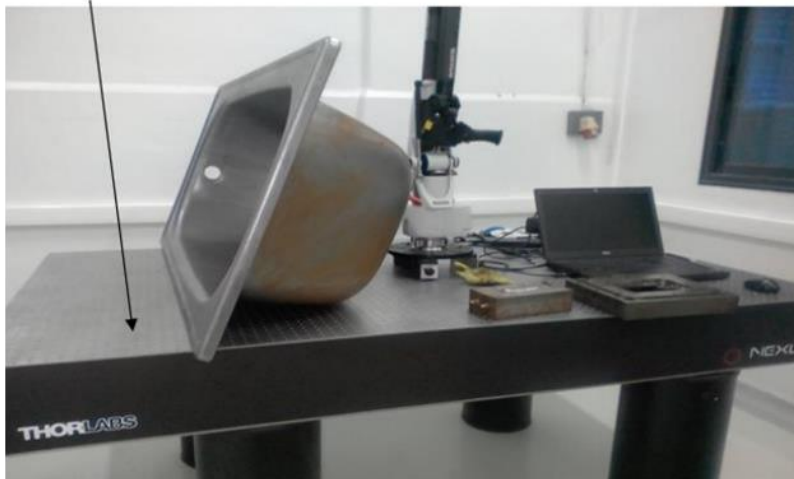

Figure 2-10 : Reference table.

The second part involves using Hexagon Metrology and the ROMER scanner software "3D-Reshaper" to establish the reference plane. The chosen plane must be validated to obtain a text file that aggregates the acquisition data in the form of three coordinates: x, y, and z.

Step 04: The operator, who manually manipulates the scanner, scanned the entire surface of the bathtub with the lights turned off. The presence of light had an undesirable effect on measurements since the bathtub surface had significant light reflection and prevented the capture of the point clouds. The operator starts from an initial point, typically preferred at the bottom right of the object. The measurement operations were divided into two parts: internal and external scanning of the bathtub. The 3D representation of the measured bathtub, both externally and internally, is generated using the "3D-Reshaper" software, which provides images in the form of point clouds (Figure 2-11).
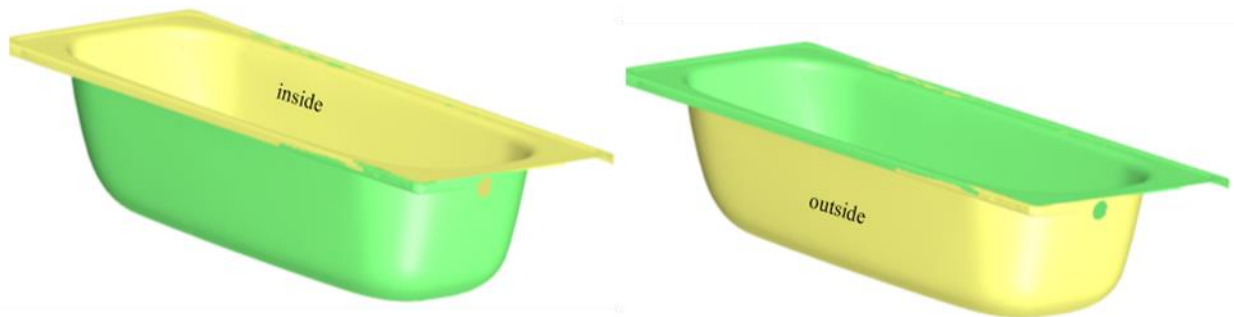

Figure 2-11 : Point clouds measured inside and outside the bathtub.

3D-Reshaper is an affordable and powerful software solution for point cloud processing, 3D modeling, 3D inspection and comparison, reverse engineering, and texturing. This software solution can function as a standalone program or as a complementary tool to certain 3D scanners or software solutions through a dedicated plugin. Reshaper's interface with ROMER scanner (with integrated or external 3D scanner) provides a solution for a wide range of applications, from 3D inspection to reverse engineering.

- Data Processing

The Geomagic Studio 2014 software is used to construct the scanned geometric shape of the bathtub. GEOMAGIC is a brand of professional engineering software from 3D Systems. These software programs focus on CAD, with an emphasis on 3D scanning and other non-traditional design methodologies. The point clouds from the external and

_____

internal scanning are assembled to form a single piece and obtain the complete 3D geometric shape of the bathtub. This procedure is explained by following the steps below:
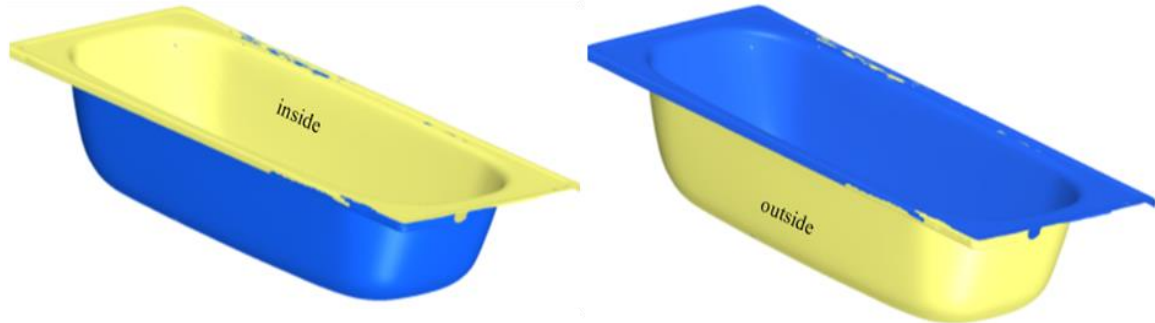
Figure 2-12 : Internal and external mesh of the bathtub.

      Step 01: Both the external and internal point cloud files are imported into the GEOMAGIC studio software. Subsequently, the geometry of the point clouds from each file is meshed (Figure 2-12). After meshing, the solid shape of the exterior and interior parts of the bathtub is obtained (Figure 2-13).
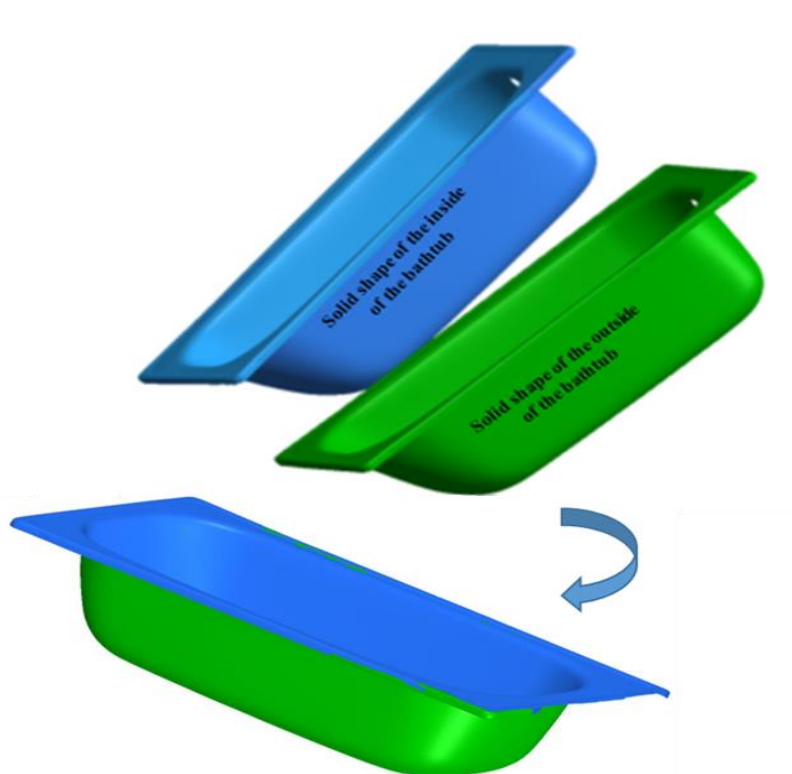

Figure 2-13 : Assembling the external and internal parts to obtain the final shape of the bathtub.

Step 02: After the meshing operation and obtaining the two solid shapes, external and internal, the assembly of the two parts is performed using GEOMAGIC studio software by aligning points of rounds, planes, and similar geometric shapes to obtain a single piece of the bathtub (Figure 2-13).

Step 03: This step involves creating the surfaces of the bathtub. To do this, the "Quick Surface Reconstruction" module in the GEOMAGIC studio software was used. Figure 2-14 represent the reconstructed external and internal surfaces of the bathtub.
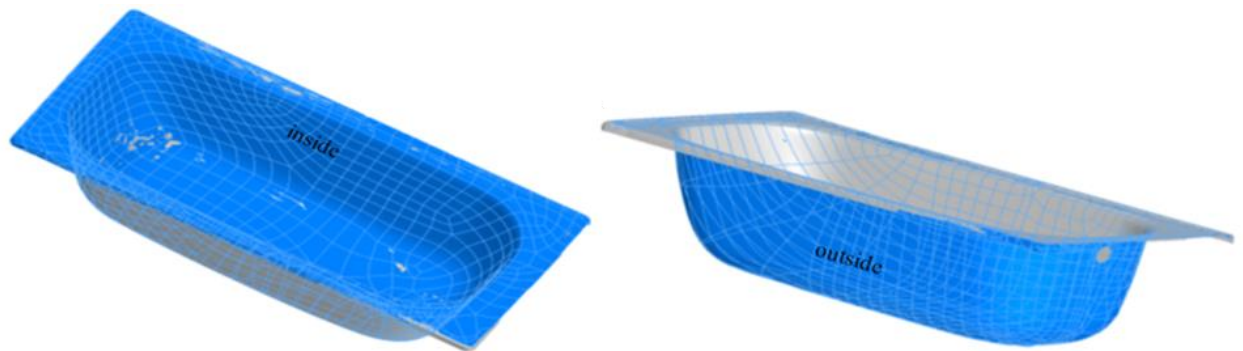

Figure 2-14 : Internal and external surfaces of the bathtub.

Step 04: After creating the surfaces of the bathtub, we saved the geometric model of the bathtub with a CAD extension (*.prt; *.sldprt). This is the final step, which involves transferring the 3D measurements to the SolidWorks geometric modeling software (Figure 2-15).

Figure 2-15 : Final CAD shape of the bathtub.

_____

- Checking the 3D measurements of the bathtub

To check the last measurement result. In the same software (GEOMAGIC), a comparison is made between the two-point cloud files (Figure 2-11) and the CAD geometric model (Figure 2-15). Figure 2-16 shows this comparison. It can be seen that the error is estimated at less than 10%.

As depicted in Figure 2-16. These 3D measurements revealed an absence of symmetry in the bathtub being measured. Notably, one side features a right angle (90°), while the other side displays an inclined angle (115°). Additionally, there are slight variations in the radii and inclinations at the four corners of the measured bathtub. For example, at the right angle, on one side there is a radius of 86 mm and on the opposite side a radius of 81 mm. This axisymmetric quality is inherent in the punch shape. This lack of symmetry is a critical factor to consider when performing numerical modeling with real parameters.
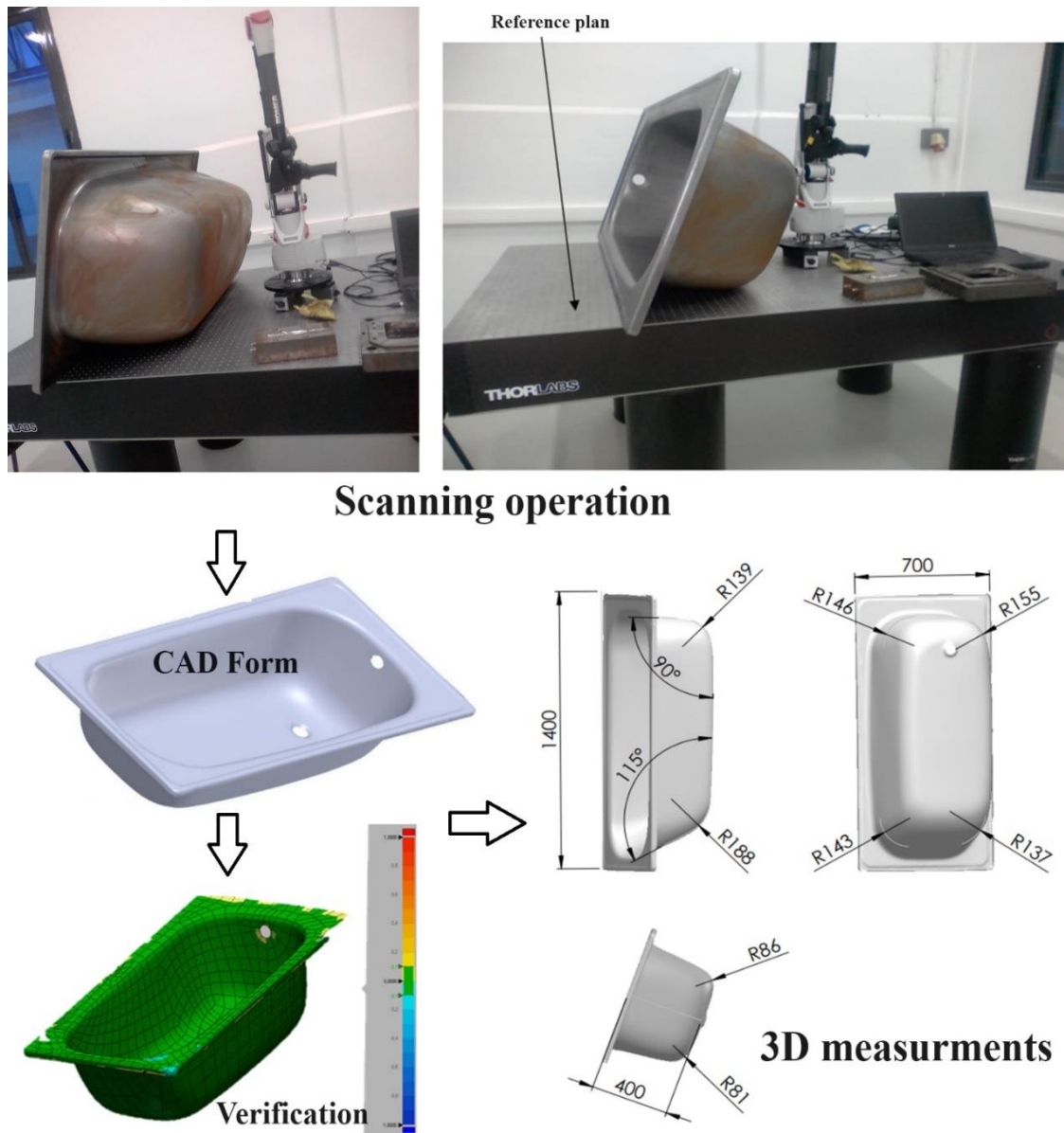
Figure 2-16 : 3D measurements of the "1400" bathtub model.

2.6.2. Ultrasonic thickness measurements

Using 3D measurements for assembling inner and outer surfaces may not provide accurate measurements when considering the bathtub thickness. For this reason, precise ultrasonic thickness measurements were conducted, as shown in Figure 2-17. The thickness changes following different sections of the bathtub were measured manually three times at the same point using the Sofranel EHC 09B ultrasonic device. The measuring range of this device is 0.2 to 508 mm with a resolution of 0.01 mm.

Figure 2-17 : Defect-free bathtub thickness measurement using the Sofranel EHC 09B ultrasonic device.

2.6.3. Experimental validation

The ultrasonic thickness measurements were compared with 3D measurements following different sections: longitudinal (A-A), transversal (B-B), and diagonal (C-C and D-D), as illustrated in Figure 2-18. The comparison of the thickness reduction reveals a good correlation between the two results with a root mean square error of 6%. The bathtub dimensions are approximately 1400 x 700 x 400 mm³. If the Romer Arm 3D laser scanner produces good results for the thickness, which is in the range of 1,6 to 0,8 mm, it can be concluded with confidence that highly accurate surface measurements are provided for both the inner and outer surfaces. The 3D measurement method proves to be valuable particularly in precisely defining the real geometry of the punch for the numerical modeling section. This is crucial as the punch represents a highly complex geometry.
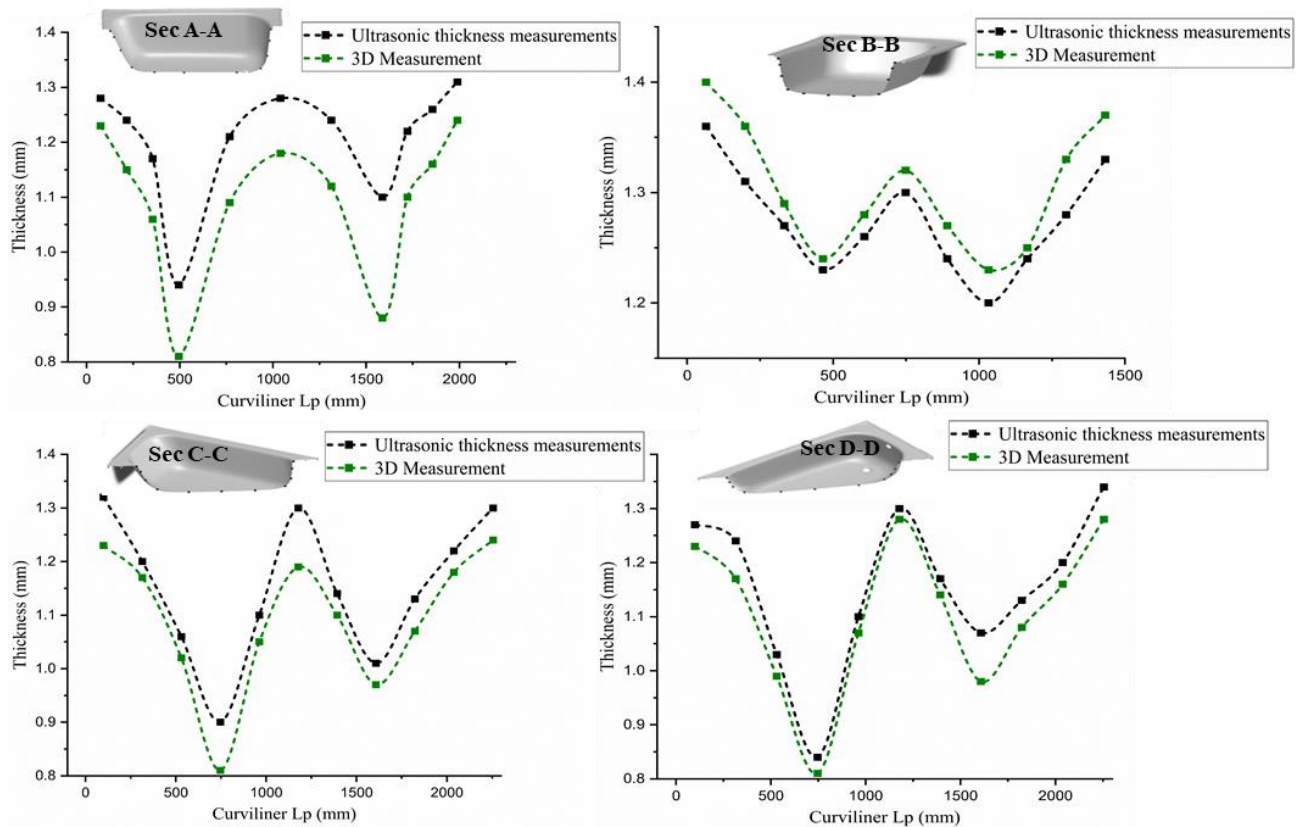
Figure 2-18 : Experimental comparison of the thickness reduction between the ultrasonic and 3D measurements.

2.7. Conclusions

Chemical and microstructural analysis showed that the carbon percentage of DC05EK is higher than that of DC06EK, indicating that the enameling process will be successful for DC05EK. However, tensile tests have shown that DC06EK has a better mechanical quality than DC05EK. In conclusion, DC05EK steel is more resistant to fish scale than DC06EK, while DC06EK has better formability. So, it is important to investigate the level of deformation achieved in the deep drawing process before choosing one of the two materials.

The comparison of the thickness reduction between 3D and ultrasonic measurements reveals a good correlation between the two results, with a root mean square error of 6%. The 3D measurements showed that the bathtub lacks symmetry. After these measurements, the bathtub's geometric shape was saved in a CAD format (*.prt; *.sldprt). This step was crucial for developing the punch tool's geometric profile for the "Finite element modeling" section (§3.3) because of its intricate design.

Chapter 3.   Simulation of Extra-Deep Drawing for Bathtubs with Industrial Parameters

3.1. *Introduction*

Sheet metal forming through extra-deep drawing (EDD) is a widely utilized technology across various industries, such as automotive, household appliances, aerospace, and appliance manufacturing. This process has gained significant development due to its extensive industrial application. At the local industrial EIMS Company for sanitary equipment in Miliana, Algeria [2], this process plays a vital role in the manufacturing of sanitary products with relatively complex shapes, such as bathtubs and kitchen sinks. Most products are obtained from cold-rolled steels (DC0xEK) dedicated to enameling by vitrification. The company specific objective is to minimize scrap resulting from defects, thereby saving time and costs. These defects are wrinkling and rupture, more specifically in the fabrication of bathtubs (Figure 3-1). The manufacturing of this product is extremely sensitive to changes in process parameters. To successfully manufacture this product, it is necessary to control all elements and factors that influence the process. Finding the optimal combination between the different process parameters remains the main challenge. In general, among the parameters that have a major influence on the EDD process are the punch, die, and blank geometries, the blank holder pressure (BHP), and the friction at tool-blank contacts [26]–[28].

Figure 3-1 : Visual representation of rupture and wrinkling defects in bathtubs manufactured by the EDD process.

At the EIMS Company, it has been noticed that machine operators rely on their experience to adjust the BHP by manipulating the pressures of six actuators on the machine to avoid rupture and wrinkling defects. The same remark was reported by [29] on a deep drawing of the "spare wheel well of the Opel Insignia". This trial-and-error

approach often results in increased scrap and press line downtime, incurring unnecessary time and cost. Furthermore, experimental testing methods often do not lead to a successful final product. To investigate the influence of BHP and other factors on the EDD process, numerical simulation is generally used. To simulate the deep drawing operation in numerical calculation software, it is necessary not only to model the process itself (geometries, tool actions, speeds, temperature, etc.) but also to feed the calculation software with [30], [31]: Elastoplastic behavior laws describe the behavior of the used sheet material; a forming limit curve or damage law describes the necking and/or rupture of the used sheet material; and a tribological behavior law expresses tool-blank contacts, whether dry or lubricated.

In this part, a numerical simulation of the bathtub EDD process was conducted using the Abaqus/Explicit finite element software. The "1400" bathtub model, manufactured from DC06EK cold-rolled steel sheet with 1,6 mm thickness, was chosen for this study. The 3D and ultrasonic thickness measurements, performed on the bathtub, was helpful, on the one hand to extract the geometric shape of the punch since the latter is geometrically complex, and on the other hand to validate the numerical approach. The objective is to control the non-uniform pressures generated by six actuators and exerted on the blank holder in order to control the blank flow between the die and the blank holder and to obtain a defect-free manufactured product. Additionally, it is crucial to investigate various scenarios that could lead to rupture and wrinkling defects, including the impact of the BHP, the initial blank shape, and the die design using draw beads.

3.2.   Previous research work

Deep-drawn bathtubs have a complex geometry and are pushed to the limits of the material formability. This application has been the subject of a few numerical investigations [32]–[34]. In previous research, the numerical simulation of the bathtub EDD process was primarily centered around the optimization of draw bead distribution on the die face [32], as well as investigating the impacts of constant BHP, friction on rupture, and wrinkling occurrences [33]. The exploration of the bathtub model EDD process involved a multiscale model that aimed to capture the real system through similarity conditions. Notably, Tomáš et al. [34] introduced a numerical modeling

approach for a "1600mm" bathtub model with a reduced scale of 1/5. While this method was experimentally validated in terms of thickness reduction in various directions of the bathtub, the specific phenomenon of wrinkling has yet to be thoroughly examined. In the numerical investigations conducted in these research works, it was assumed that the BHP remained constant throughout the bathtub EDD process. This simplifying assumption was made in their numerical simulations of the process, but it differs from the actual process as explained in the "Deep-drawing Chain" subsection. In reality, non-uniform pressures are applied to the blank holder and vary in different zones to prevent wrinkling and rupture defects. After dimensional verification, M. Hojny et al. [33] noted that the flatness of the blank holder and the die used for deep drawing of a "1200" bathtub model were not perfect. They indicated that this is the reason why rupture and wrinkling occurred during the manufacturing process. This lack of tool flatness was compensated by non-uniform pressures during the actual technological process.

In several research works and industrial applications of deep drawing, there is a common assumption that the pressure exerted on the blank holder remains constant and uniform. However, to prevent issues such as wrinkling and rupture defects, it has become necessary to apply variable pressure as a function of time or punch displacement [35], [36]. Another method involves applying different pressures simultaneously, i.e., non-uniform pressures, to the blank holder, as seen in the industrial case under study in this research. Some studies introduced the concept of variable blank holder force (VBHF) to optimize the process and consequently obtain defect-free deep-drawn products. Kitayama et al. [35] conducted a case study that specifically focused on the simultaneous optimization of the blank shape and VBHF trajectory in deep drawing. Meanwhile, Feng et al. [36] proposed a method for optimizing VBHF as a function of punch stroke in deep drawing, utilizing a trust region algorithm to predict and control the accuracy of the support vector regression approximate model of VBHF. This approach was validated through numerical and experimental comparisons. Klaus M. Wurster et al. [37] presented a procedure for the automatic optimization of the BHF distribution in a deep drawing process using numerical simulation. The blank holder was divided into 10 segments to exert different pressures simultaneously on the blank. This segmentation allowed for the identification of an optimized distribution of non-uniform pressures applied to the blank and VBHF during deep drawing, i.e., as a function of time. Zhong-Qin et al. [38]

introduced a new strategy to optimize VBHF and determine the drawing limit under both constant and variable BHF conditions. Their optimization approach, rooted in the analysis of BHF formability windows, was seamlessly integrated into the finite element method code to derive the optimal BHF applied in both temporal and spatial dimensions. Also, in this numerical simulation aiming to apply varying pressures simultaneously to the blank, the blank holder was divided into 10 rigid segments. These innovative methods exemplify ongoing efforts to improve the efficiency and reliability of deep drawing processes through advanced optimization techniques.

As previously stated, it is not only the BHP that has a role in preventing wrinkling and rupture defects in EDD processes. The latter can also be influenced by punch, die, and blank geometries. In fact, in specific industrial contexts, mechanical presses often incorporate strategically positioned draw beads around the die. The latter are employed to precisely manage and predict material flow in the deep drawing process. It has been demonstrated that various material characteristics, such as tensile strength and fracture strain, are significantly changed after passing through a draw bead [39]. These beads serve to impede the movement of the blank, allowing precise control over the applied pressure and maintaining the proper gap between the blank holder and the die [40], [41]. When the BHP is low, the draw bead effectively restricts the blank, necessitating its minimization to prevent wrinkling. Regarding the blank geometry, Gharehchahi et al. [42] pointed out that optimal blank design has the advantage of reducing costs and waste and enhancing process quality and thickness distribution in the resulting product. The mentioned research studies [32]–[34] carried out their work on the bathtub EDD process, where the blank was cut at the four angles to obtain a defect-free product. Ghennai et al. [43], [44] utilized a blank cut from these four sides in the numerical simulation of deep drawing for a waterproof case in a truck. This indicates the significance of cutting the blank along these four sides or in other words, using the initial geometry of the sheet metal.

As for friction, it has a great influence on the EDD process. Exploring this parameter, Neto et al. [45] examined, using a numerical approach, the impact of pressure-dependent friction on wrinkling during the deep drawing process. In a comprehensive study involving both numerical simulations and cold deep drawing experiments, Bahanan et al. [46] highlighted the significant influence of friction on the process, demonstrating

that smoother flow near the die surface compared to the punch area can help reduce the occurrence of ruptures during forming. Kim et al. [47] evaluated various lubricants, highlighting the central role of effective lubrication in reducing problems such as localized thinning, rupture, and wrinkling, as well as reducing tool wear in high-volume production.

3.3. *Finite element modeling*

The extra-deep drawing operation of the bathtub, described in "Deep-drawing Chain" subsection (§1.5.2.1), is modeled by FE using the ABAQUS/Explicit. The flowchart of the process simulation is illustrated in Figure 3-2.
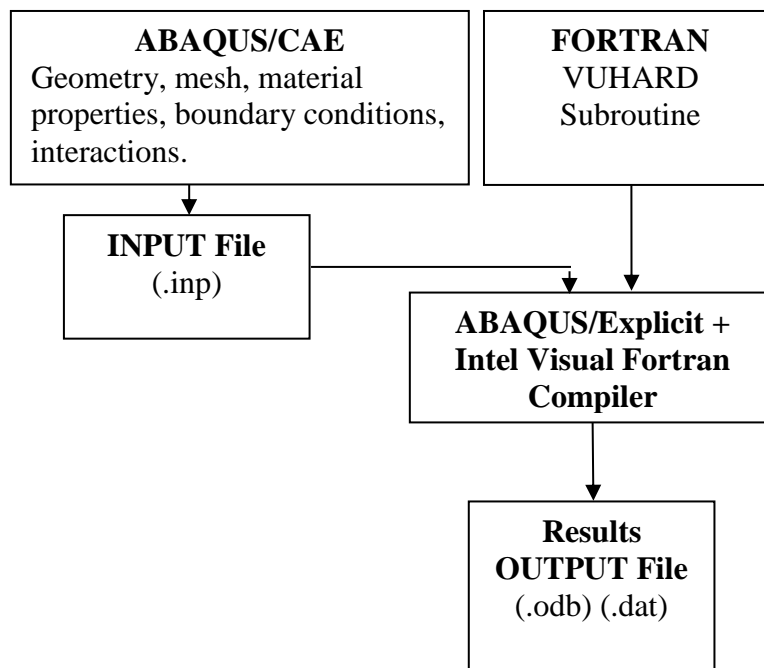

Figure 3-2 : Flowchart of the numerical simulation of the bathtub extra-deep drawing process.

The different stages of numerical modeling are presented as follows:

3.3.1. Geometry and Mesh

Numerical modeling of the EDD operation of the bathtub (Figure 3-3) was carried out using Abaqus/Explicit finite elements software. The assembly of different tools with the blank is illustrated in Figure 3-3(a). The punch is the most geometrically complex part. Upon analyzing the 3D measurements of the bathtub, disparities were noted in the inclinations of its sides. Furthermore, subtle variations in radii and inclinations were

discernible at the four corners of the measured bathtub, as described in the "Measurements" section. Consequently, axisymmetry was not considered in this numerical modeling. Following the 3D measurements, the bathtub geometric shape was saved in a CAD extension (*.prt; *.sldprt). This step was imperative for constructing the geometric profile of the punch tool due to its complex geometry. The design of this tool was derived from the geometric model of the bathtub, utilizing the option to generate a mold or imprint in SolidWorks software. The geometric construction of the blank and other tools was performed directly in Abaqus.
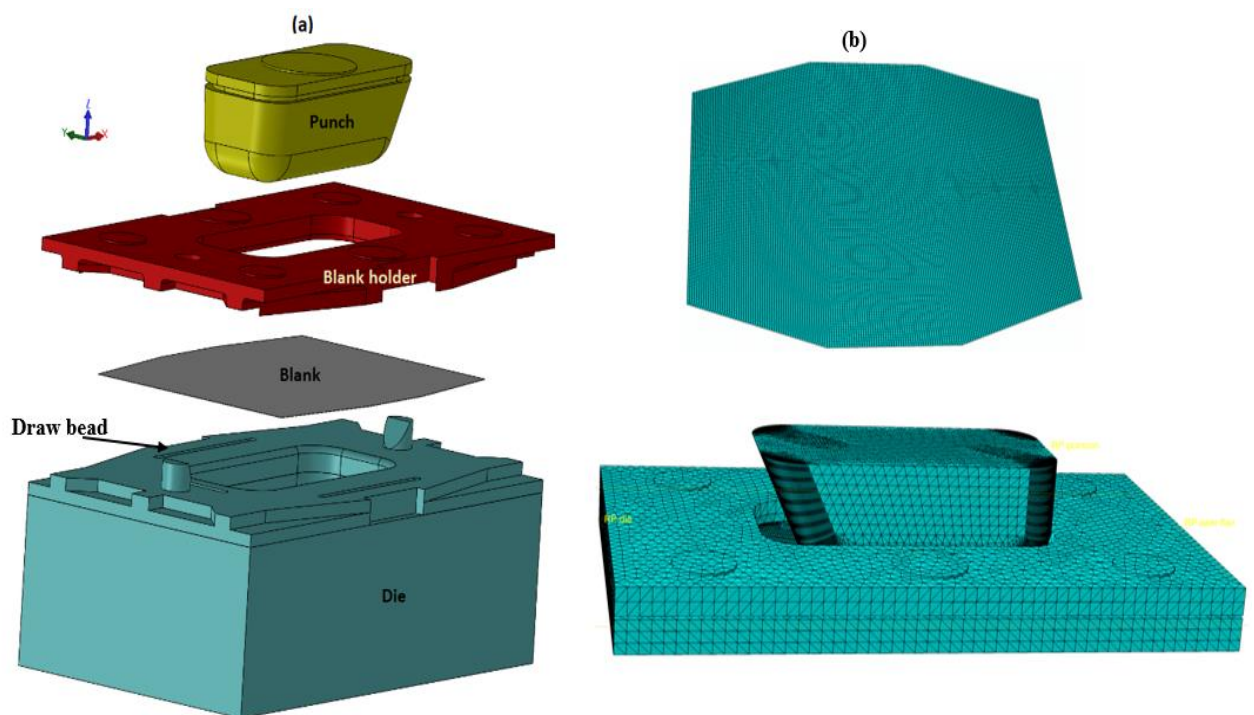

Figure 3-3 : (a) Different parts of the bathtub EDD process, (b) Finite element mesh.

In the context of the numerical simulation of the EDD process, the distinction between rigid and deformable components plays an important role. Generally, the blank is considered deformable, susceptible to exhibiting elastoplastic behavior or even to being damaged under mechanical loads. However, the discrete rigid option is generally chosen to represent tools that are treated as rigid entities resistant to deformation, especially in our case where:

1. The punch is the stiffest tool since it has a significant volume and inertia.

2. The die and the blank holder are also stiff and reinforced by ribs to have better flatness without there being elastic deformation during the EDD process.

In Abaqus software, a discrete rigid part is similar to a deformable part in that it can be any arbitrary shape. A discrete rigid part is used in contact analyses to model bodies in which the tooling elements, composed of nodes, elements, and surfaces, have constant relative positions throughout the simulation which makes them resistant to deformation. This means that when any of the conditions below are applied, Abaqus software takes them into account, depending on the borders and regions in which they are applied [48].

The blank was meshed using the S4R element type, a four-node quadrilateral shell element, which can deform in a transverse shear plane [49], [50]. The three-dimensional triangular (R3D3) rigid elements type was selected to mesh the tools (Figure 3-3(b)), which can be used to define the surfaces of rigid bodies for contact and to be attached to deformable elements [48].

As shown in Figure 3-4, a mesh sensitivity analysis was performed for the blank using six different mesh sizes. The blank was the only object of this analysis as it was considered to be deformable. Mechanical properties, tool-blank contacts, and boundary conditions are detailed in the paragraphs below. It is observed that the coarse meshes produced slightly different punching force curves compared to the others (Figure 3-4(b)), whereas the normal and fine meshes yielded similar outcomes. Relying solely on global data like punching force doesn't allow for accurate mesh selection in this analysis. Hence, local data was examined, specifically the equivalent plastic strain (shown in Figure 3-4(a), and (c)). From the latter, it is noticed that the results stabilize with an element size of 15 x 15. Consequently, the mesh with element size 10 x 10 is chosen in the numerical simulation due to its better convergence and lower CPU usage compared to other mesh sizes.
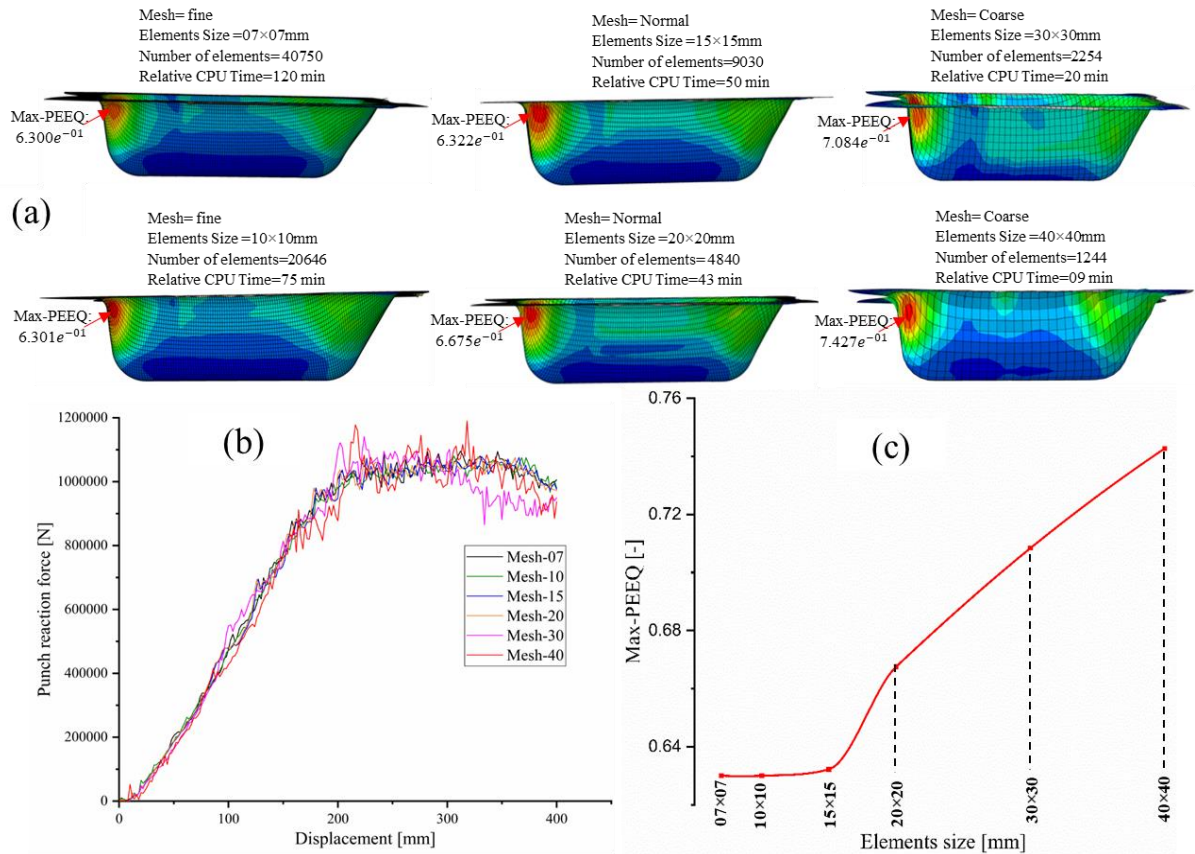
Figure 3-4 : Mesh sensitivity analysis: (a) Illustration of different mesh sizes, (b) Punch load vs. displacement results for different mesh sizes, and (c) Equivalent plastic strain results for different mesh sizes.

Table 3-1 lists the element count and mesh type for every component used in the numerical modeling.

Table 3-1: Number of elements and nodes in each part.

Parts	Number of elements	Number of nodes	Mesh type
Blank	20646	10674	Quadrilateral « S4R »
Punch	4874	2439	Triangular « R3D3 »
Die	28912	14456	Triangular « R3D3 »
Blank holder	19380	9477	Triangular « R3D3 »
Total	73812	37046	

3.3.2. Material

The deep-drawing steel DC06EK was modeled with an anisotropic elastoplastic behavior. The elastic part is described by Hooke's model with a Young's modulus E = 203000 MPa and a Poisson's ratio ν = 0,3. Regarding the plastic part, the anisotropic yield

criterion proposed by Hill48 [51] was adopted. The Hill48 criterion, operating under the assumption of plane stresses, is written (Equation 1-2).

The parameters were calculated using the following formulas:

$$F = \frac{r_0}{r_{90}(1+r_0)}, G = \frac{1}{1+r_0}, H = \frac{r_0}{1+r_0}, N = \frac{(1+2r_{45})(r_0+r_{45})}{2r_{90}(1+r_0)} \qquad \text{3-1}$$

r_0, r_{45} and r_{90} represent Lankford's r-values.

Table 3-2: Parameter values of Hill48 anisotropic plasticity model.

F	G	H	N
0,258	0,324	0,675	1,156

Where R11, R22, R33 and R12 are four material parameters to apply Hill48 in Abaqus. There are other parameters, R13 and R23, who's assumed to be equal to one.

$$r_{11} = \sqrt{\frac{1}{G+H}}, \quad r_{22} = \sqrt{\frac{1}{F+H}}, r_{33} = \sqrt{\frac{1}{F+G}} \quad, r_{12} = \sqrt{\frac{3}{2N}} \qquad \text{3-2}$$

Table 3-3: Parameter values of Hill48 anisotropic plasticity model "Yield stress ratios".

r_{11}	r_{22}	r_{33}	r_{12}	r_{13}	r_{23}
1,00050	1,03528	1,31080	1,13911	1	1

The Hill48 anisotropic yield criterion was coupled with Ludwick's hardening law (equation 3-3) in the numerical modeling. The hardening law was implemented into the Abaqus/Explicit via a VUHARD subroutine. While the Hill48 parameters were introduced directly in Abaqus/Explicit. The mechanical properties of the same DC06EK sheet metal were determined by Belguebli et al. [16] and illustrated in Table 3-4.

$$\sigma = \sigma_0 + K\left(\varepsilon_p\right)^n \qquad \text{3-3}$$

_____

Table 3-4: Mechanical properties of the DC06EK [16].

Rolling direction [°]	0° RD	90° RD	45° RD
Lankford's r-values [-]	2,826	2,689	1,959
Yield stress Rp0.2 [Mpa]	149,61	142,95	145,15
Material consistency K [-]		517.64	
Hardening exponent n [-]		0.423	

3.3.3. Tools-blank contacts

In the finite element model, the blank was assembled in direct contact with different tools (Figure 3-5). A 'Surface to Surface' type contact was used with the 'Slave-Master' concept to describe the interaction between a rigid surface and a deformable surface [52]. This concerns the contacts: blank-die, blank-punch, and blank-blank holder. Coulomb's law was used to describe the friction of the tool-blank contacts. Based on the results of the ball-on-disc tribological tests, a coefficient of friction with a uniform value of "0,13" was assumed for all tool-blank contacts.
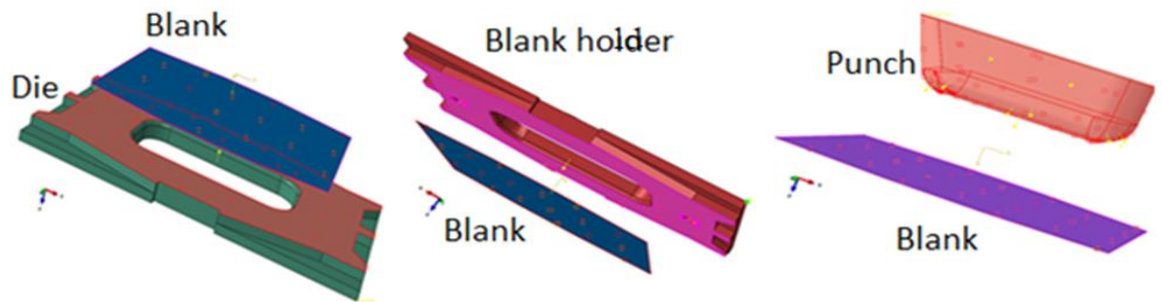

Figure 3-5 : Tools-blank contacts.

3.3.4. Boundary conditions and loading

Tool movements, blank holder pressure, and different loads were defined in boundary conditions, as presented in Figure 3-6. These parameters introduced in the numerical modeling were exactly like the real bathtub EDD process at the company, allowing them to manufacture a defect-free "1400" bathtub model. A punch reference point was used to obtain the reaction force versus displacement during the numerical simulation. The main boundary conditions and loading imposed on the various EDD tools are as follows:

1. A displacement of 400 mm with a constant speed of 50 mm/s was applied to the punch.

2. Blank Holder Pressures:

   a. The BHP is composed of six independently controlled actuators (Figure 3-6).

   b. The pressures, illustrated in Table 3-5, were applied in the numerical modeling, reflecting the pressures adjusted by the machine operator on each actuator to achieve a defect-free bathtub during manufacturing.

Table 3-5: Applied pressure on each actuator in the numerical modeling.

Actuators	Act 1	Act 2	Act 3	Act 4	Act 5	Act 6	Total
Pressures (MPa)	08	09	09	07	12	11	56

(A)- Machine   (B)- Numerical modeling
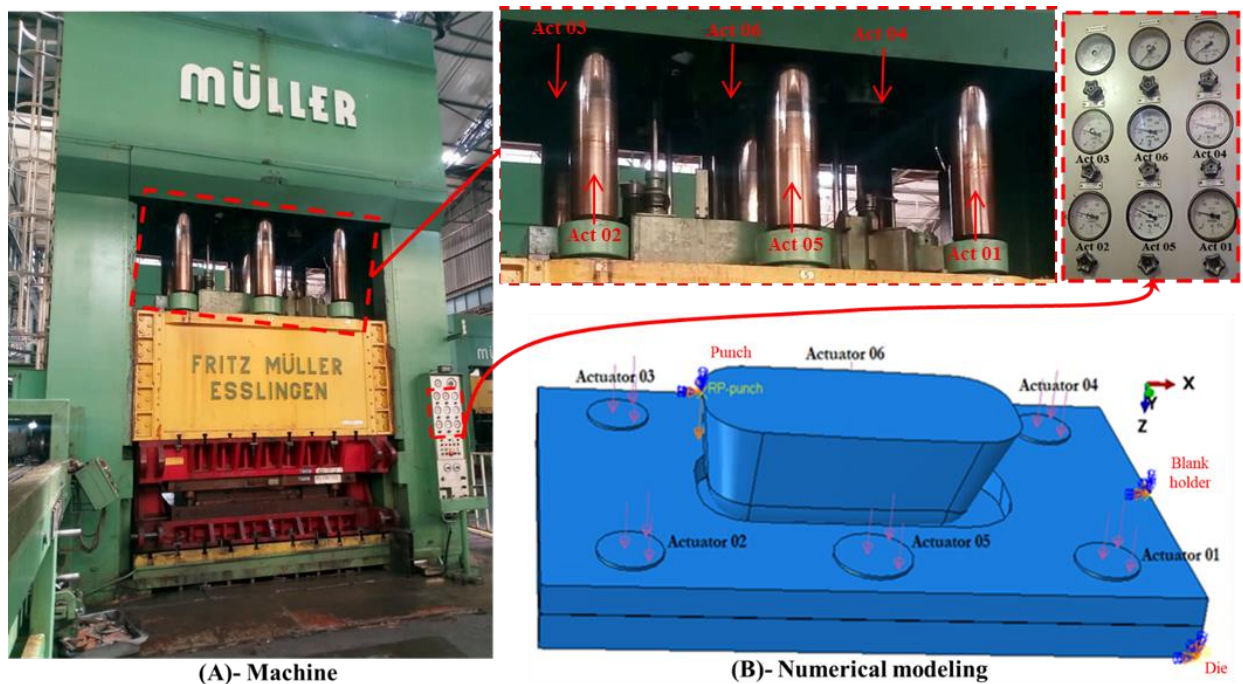
Figure 3-6 : Loading and boundary conditions applied to the different tools exactly like the real EDD process of a bathtub manufactured in the industrial company.

   c. Various pressures are tested to examine and assess the occurrence of ruptures and wrinkling defects. The objective is to determine the optimal range of pressures, both lower and higher applied to the blank holder to achieve a defect-free product.

> d. The diverse pressures are kept consistent throughout the entire EDD operation.

3. The die was fully fixed.

3.4. Results and discussion

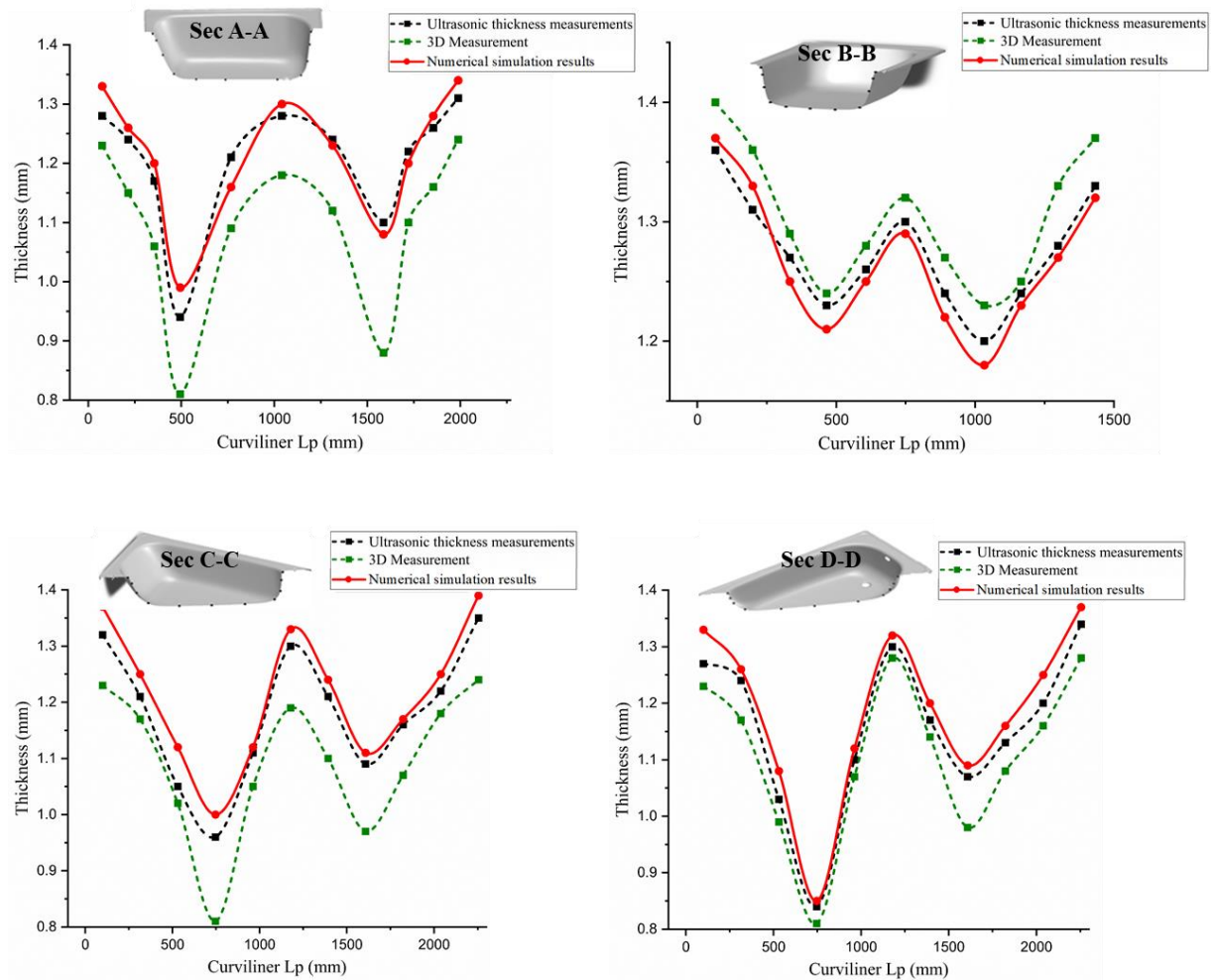### 3.4.1. Experimental and numerical validation

Figure 3-7 : Numerical/experimental comparison of thickness reduction following different paths in the bathtub.

The ultrasonic thickness measurements were compared with 3D measurements and numerical simulation results following different sections: longitudinal (A-A), transversal (B-B), and diagonal (C-C and D-D), as illustrated in Figure 3-7. The comparison of the thickness reduction reveals a good correlation between the two results with a root mean square error of 6%. The bathtub dimensions are approximately 1400 x

700 x 400 mm³. If the Romer Arm 3D laser scanner produces good results for the thickness, which is in the range of 1,6 to 0,8 mm, it can be concluded with confidence that highly accurate surface measurements are provided for both the inner and outer surfaces. The 3D measurement method proves to be valuable particularly in precisely defining the real geometry of the punch for the numerical modeling section. This is crucial as the punch represents a highly complex geometry.

To validate the numerical simulation, another comparison of the thickness reduction was conducted between the ultrasonic thickness measurements and the numerical results (Figure 3-8). The comparison shows very good concordance following the different sections, with a root mean square error of 3%. This result allows us to conclude that the bathtub EDD process numerical simulation corresponds to this manufactured at the EIMS Company.
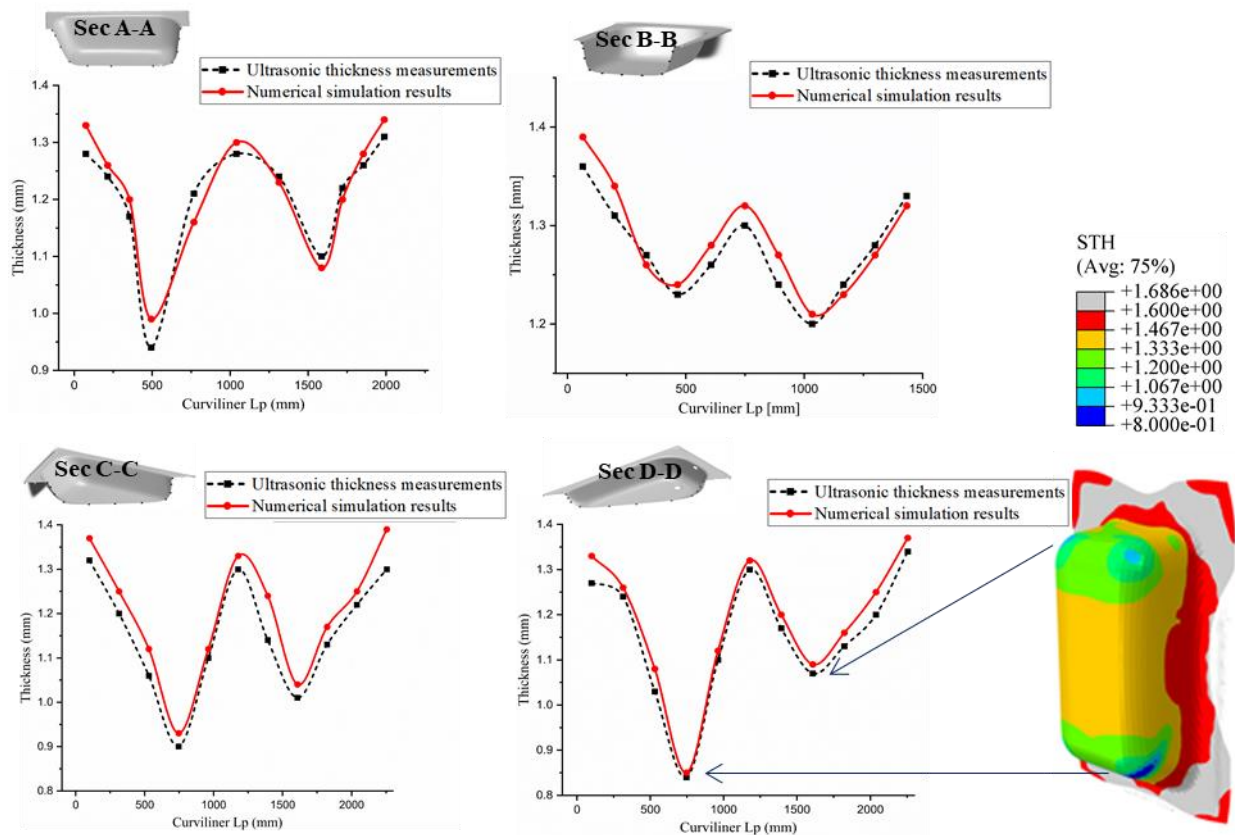

Figure 3-8 : Numerical simulation / the ultrasonic thickness measurements comparison of thickness reduction following different paths in the bathtub.

It should be noted that thickness reduction is more pronounced in regions that align with the corners of the bathtub. These significant deformations occur due to the

contact between the blank and the radii of the punch corners. In these specific areas, the thickness decreases from 1,6 mm to approximately 0,8 mm (see Figure 3-8, section D-D). Several studies also indicate that the minimum thicknesses were identified at the punch corner radii, both in simulations and experiments [16], [34], [53]. It is noteworthy that the observed thicknesses consistently remain above 0,8 mm, implying that the deformation in thickness does not exceed 50%. These findings are corroborated by the thickness reduction map in the bathtub shown in the same Figure 3-8 after the forming operation with a final punch travel of 400 mm, revealing a thickness reduction from 1,6 mm to ~ 0,8 mm.

3.4.2. Formability

The FLC for the DC06EK sheet metal with 1,6 mm thickness, used for evaluating the formability of the deep-drawn bathtub, was established by Belguebli et al. [16] through the Keeler and Brazier model [17], [18], as represented in the "Forming limit curve" subsection (§1.6.2). The predicted limit strains taken from the numerical simulation of the bathtub EDD process must remain constantly lower than the FLC so that the drawn bathtub does not undergo necking or rupture with a safety margin of approximately 10% [54]. These limit strains not only pertain to necking or rupture but can also predict wrinkling. The latter phenomenon tends to occur when the blank is subjected to low BHP or extensive lubrication. The risk of wrinkling becomes particularly pronounced when the material is exposed to strain limits varying from pure shear to uniaxial compression.

First, the formability analysis was conducted on the specific case to align with the parameters set by the machine operator on the press for defect-free bathtub manufacturing, as depicted in Figure 3-9 (a). This case corresponds to the non-uniform pressures applied to different actuators, as presented in Table 3-6. The results of the numerical simulation show that all limit strains are in the safe area, with no evidence of necking, rupture, or wrinkling. These findings indicate that the material exhibits an excellent formability.
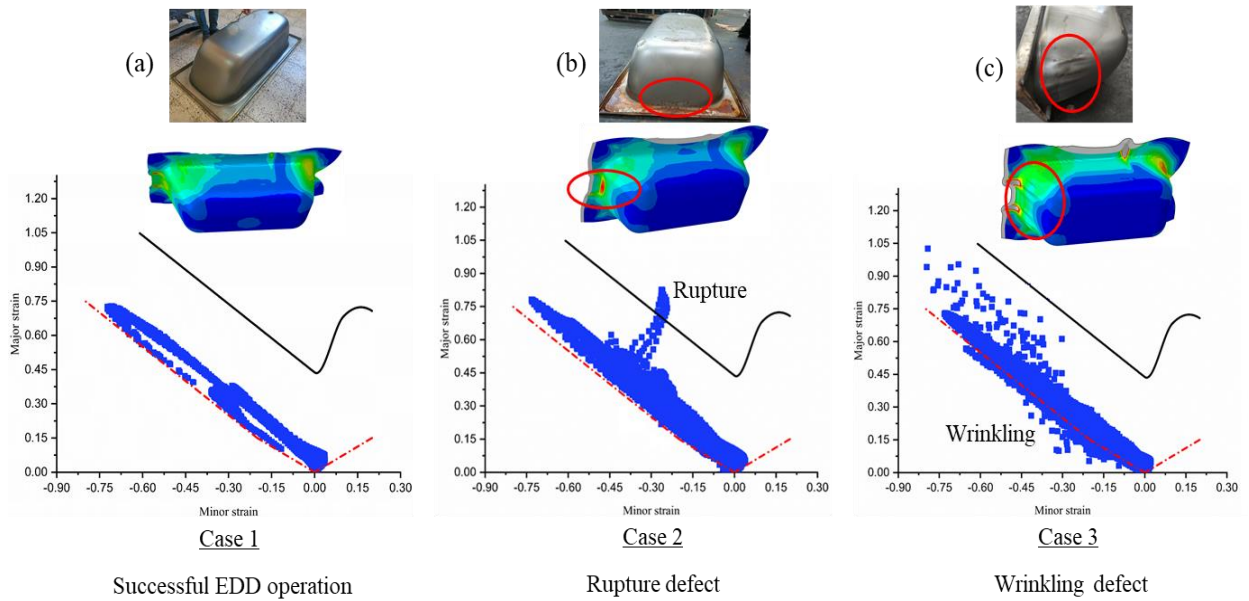
Figure 3-9 : Forming limit diagram for different cases of non-uniform pressures applied to the blank holder (cases 1 to 3).

When the pressures are adjusted, either increased or decreased by a value of 3 MPa across all BHP actuators in the numerical simulation (see Table 4), defects such as necking or wrinkling emerge, as depicted in Figure 3-9 (b) and (c). This observation aligns with the findings at the EIMS Company, where similar defects occurred in identical locations in deep-drawn bathtubs. This correlation is evident through the comparison of figures captured at the company and the equivalent plastic strain cartographies in the same Figure 3-9. Consequently, the optimal pressures applied to actuators lie within the range of these last two cases (2 and 3) to obtain a defect-free bathtub.

Table 3-6: Three different blank holder pressure cases for deep drawing of the bathtub.

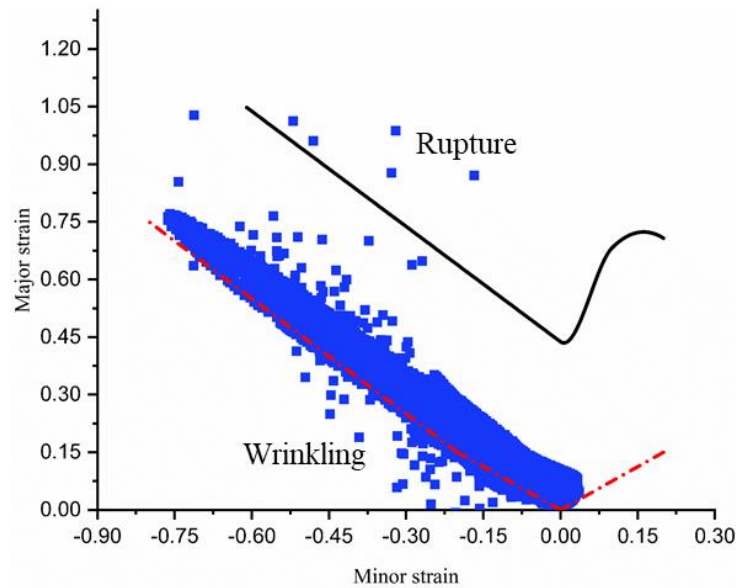|	Actuators BHP cases	Act 1	Act 2	Act 3	Act 4	Act 5	Act 6	Total pressure
Non-uniform pressures	Case 1: Successful EDD operation	08	09	09	07	12	11	56 Mpa
	Case 2: Rupture defect	11	12	12	10	15	14	74 Mpa
	Case 3: Wrinkling defect	05	06	06	04	09	08	38 Mpa
Uniform pressure	Case 4: Rupture and Wrinkling defects	9.33	9.33	9.33	9.33	9.33	9.33	56 Mpa

Figure 3-10 : Forming limit diagram for uniform pressures applied to the blank holder (case 4).

Applying uniform pressure (as in case 4, Table 3-6) to the blank holder results in both rupture and wrinkling defects in the final product as illustrated in Figure 3-10. Some points on the limit strains surpass the FLC of the DC06EK, indicating rupture, while others fall below the line of uniaxial compression, indicating wrinkling. It is worth noting that even though the numerical simulation assumes perfect flatness of the blank holder and the die in the bathtub EDD process, uniform pressure applied to the blank holder does not lead to a defect-free bathtub.

3.4.3. Displacements

Figure 3-11 illustrates displacement maps depicting the deep-drawing of bathtubs in the deep-drawing direction for the four BHP cases, as outlined in Table 3-6. Among these cases, three involved non-uniform pressures applications, resulting in successful EDD operation (case 1), rupture (case 2), and wrinkling (case 3). The fourth case corresponds to pressures imposed uniformly, which led to both rupture and wrinkling defects. It is evident from the maps that a punch displacement of 400 mm was reached during deep drawing for all four cases.
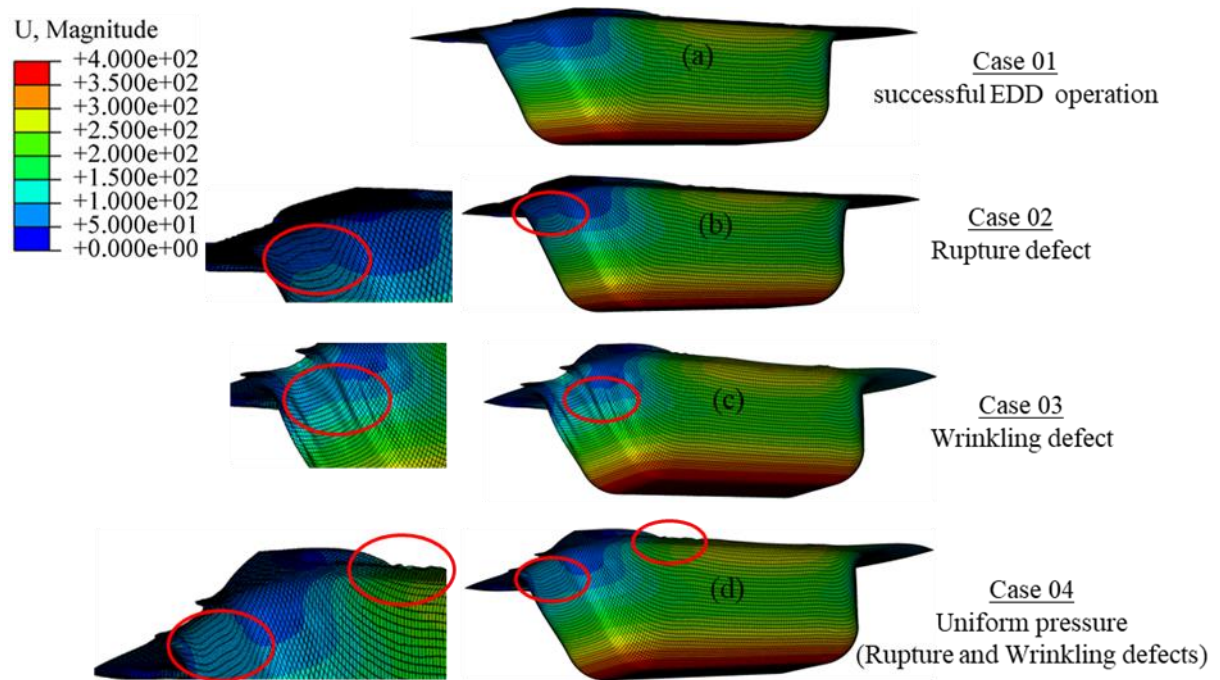
Figure 3-11 : Displacement maps depicting deep-drawn bathtubs for the four BHP cases.

The wrinkling defect can be clearly visualized in the displacement maps. These latter affirm that no wrinkling is observed for case 1 (Figure 3-11-a) which corresponds to the scenario of the defect-free product. Similarly, case 2 (Figure 3-11-b) shows no wrinkling; however, this lack of wrinkling is explained by limit strains that surpass formability limits and result in rupture defects. On the other hand, pronounced wrinkles are clearly visible in both cases 3 and 4 (Figure 3-11-c and (d)). These results support the remarks drawn in the "Formability" section.

This highlights the central role of BHP as a critical operational parameter to achieve a defect-free product. Effective control of the blank flow between the blank holder and the die during EDD operations depends on the carefully selected pressures applied to the blank holder. This idea reinforces the importance of careful pressure management for optimal production results.
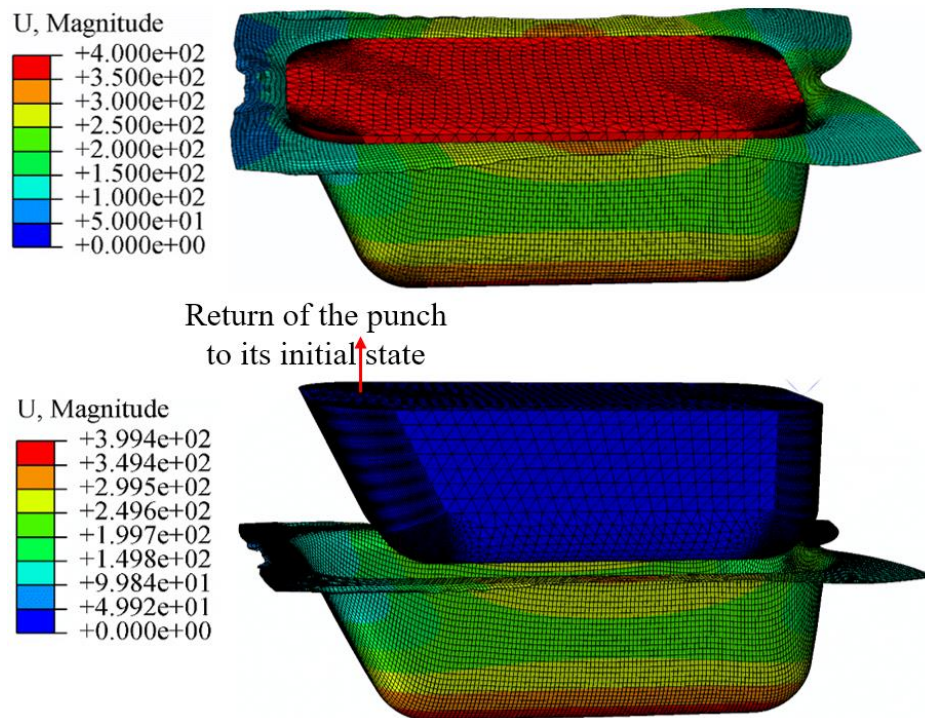
_____

Figure 3-12 : Springback process results from numerical simulation of the extra-deep drawing bathtub.

Springback, the geometric alteration that occurs in a part after forming, is a critical consideration in sheet metal manufacturing as it directly influences dimensional accuracy post-forming, especially in deep-drawn and stretch-drawn parts [55]. In our case study, we anticipated minimal springback due to the nature of extra-deep drawing, given that the plastic strain reached the formability limits of the material. This observation aligns with the absence of springback issues noted in the company operations. Subsequent inspection of numerical simulation results (Figure 3-12) confirmed this expectation, revealing low springback values with a displacement amplitude of only 0,6 mm after raising the punch.

3.4.4. Punching force

The punching force is a very important parameter in the study of the numerical simulation of deep-drawing processes. This parameter is influenced by the friction at the sheet-tool contacts, the mechanical properties of the blank, the BHP, and punch speed [56]–[58]. The variation of punching force according to its displacement for different BHP cases is illustrated in Figure 3-13. For cases 1, 2, 3, and 4, the punching force increases to approximately 1100 kN, 1200 kN, 900 kN, and 1070 kN, respectively, at a

punch displacement of about 200 mm. At this stage, the force exerted by the punch must overcome multiple factors. These include:

- the strength of the sheet metal,

- the resistance from friction at the points where the blank interacts with the tools, particularly at the punch corner radii and the cavity die shoulder radii,

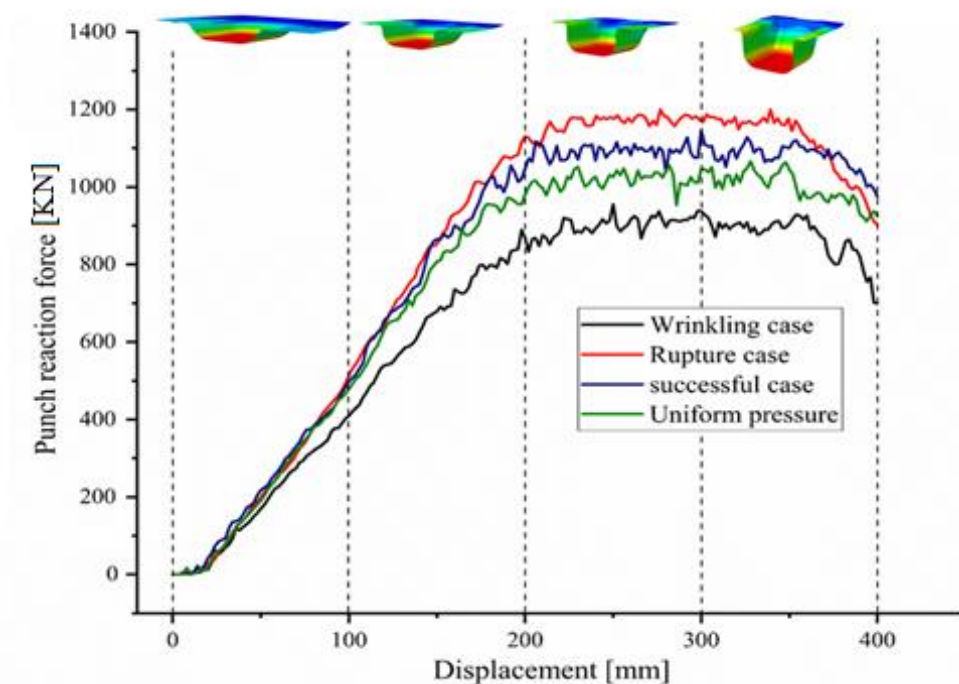- and the pressures exerted on the blank holder.

Figure 3-13 : Punching force vs punch displacement for different values of BHP.

The highest force occurs precisely when the blank is completely shaped within the die shoulder radii and the punch corner radii. After this point, the punching force stabilizes or decreases because the frictional resistance decreases.

Uniform and non-uniform pressures have the same punch reaction force as a function of punch displacement, but as seen previously, the uniform led to both rupture and wrinkling defects in the bathtub final product. Hence, there is a need to take into account applying different pressures simultaneously to avoid these defects.

Examining the punching force curve can assist engineers and manufacturers in optimizing the EDD process for optimal energy efficiency [16]. The work done on the material during the EDD process is represented by the area under the punching reaction force/displacement curve. This energy expenditure encapsulates the total energy consumed in the entire process. As a result, the control margin for BHP within the range observed in cases 2 and 3 can be exploited to optimize the punching force versus displacement curve, ultimately reducing energy consumption.

3.4.5. BHP, blank shape, and draw beads investigation

Beyond the four BHP cases discussed earlier, this subsection conducts a numerical simulation investigation on the presence or absence of draw beads in the die and/or the cutting of the sheet metal before forming. Different results and remarks from this investigation are depicted in Figure 3-14.

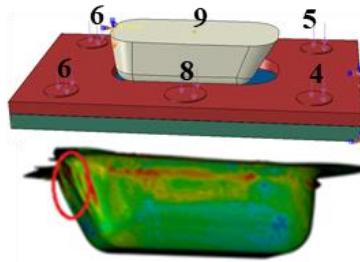## *Non-uniform pressure*

Case 1: successful EDD operation

This case corresponds to the actual manufactured scenario <u>without defects</u>, for which real parameters were used in the numerical simulation of the bathtub extra-deep drawing process.
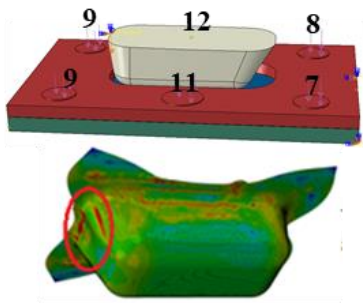

Case 2: rupture defect

This case leads to <u>rupture</u> initiation in the bathtub after a 3 MPa increase in all pressures applied to the BHP of case 1.

Case 3: wrinkling defect

<u>Wrinkling</u> in the bathtub took place by reducing the pressures by 3 MPa compared to case 1.
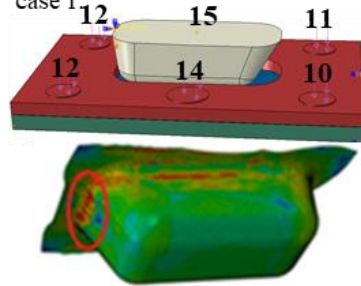
Case 4: without draw beads

The absence of draw beads in the die leads to the presence of <u>wrinkling</u> in the bathtub at the end of the EDD operation.

Case 5: with no cutting of the corners of the blank

The absence of cutting the sheet metal at these four angles before the EDD operation, i.e., using a rectangular blank, leads to a bathtub with an appearance of <u>wrinkling and rupture</u>.
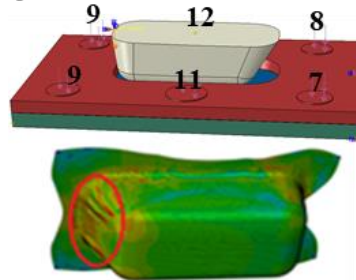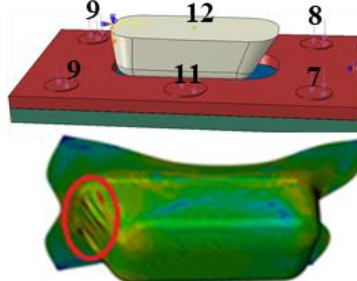

Case 6: without draw beads with no cutting of the corners of the blank
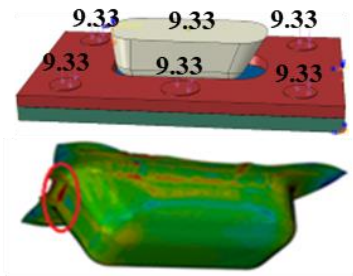
The absence of both draw beads in the die leads and the cutting of the sheet metal at these four angles contribute to the presence of <u>wrinkling</u> in the bathtub at the end of the EDD operation.
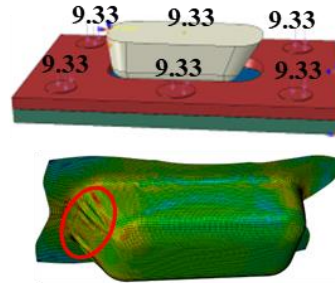
Uniform pressures

Case 7: rupture and wrinkling defects

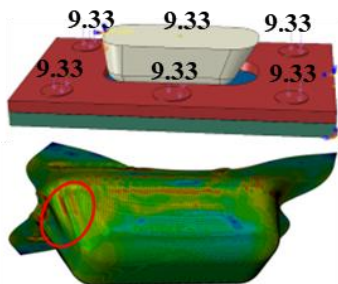Equal pressures of 56 MPa/06 applied to the blank holder lead to both rupture and wrinkling.

Case 8: without draw beads

Equal pressures in the absence of draw beads lead to the presence of wrinkling in the bathtub.

Case 9: with no cutting of the corners of the blank

Using a rectangular blank with equal pressures results in wrinkling in the tub.

Case 10: without draw beads and with no cutting of the corners of the blank

The absence of both draw beads in the die leads and the cutting of the sheet metal at these four angles contribute to the presence of wrinkling in the bathtub.
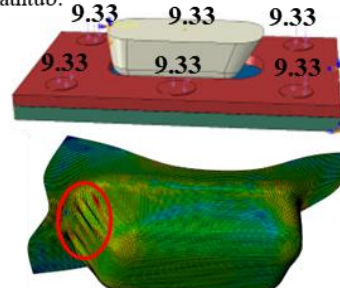
Figure 3-14 : Exploring potential causes of rupture and wrinkling defects, examining the influence of BHP, the initial blank shape, and draw bead.

3.5.   Conclusions

In this research, a successful investigation of a bathtub EDD process using numerical simulation based on the Abaqus/Explicit finite element software. The numerical approach was validated through ultrasonic thickness measurements. The agreement between the numerical and experimental results demonstrated the accuracy and reliability of the numerical approach.

Upon analyzing the formability of various scenarios of BHP, it was concluded that the bathtub EDD process is pushed to its formability limits. Even with the assumption of perfect flatness in the blank holder and die, applying uniform pressures to the blank holder does not ensure a defect-free bathtub. Both uniform and non-uniform pressures result in

approximately the same curve of punching reaction force versus punch displacement, i.e., consume approximately the same amount of energy during the EDD process, but the uniform BHP results in both rupture and wrinkling defects in the bathtub final product. In this case, it is difficult to analyze the success or failure of the final product from punching force results.

Applying non-uniform pressures to the blank holder is necessary to control the blank flow between the blank holder and the die due to the complex geometry of the final bathtub product. It was found that the optimal pressures applied to the actuators fall within the range observed in cases 2 and 3. Consequently, the control margin for BHP is very restricted, allowing only a maximum variation of ± 3 MPa to achieve a defect-free product. This finding can be exploited to optimize the punching force versus displacement curve, ultimately reducing energy consumption.

Additionally, after exploring potential causes of rupture and wrinkling defects, it is crucial to consider the sheet metal cutting angles and the presence of draw beads. These factors play a significant role in achieving a deep-drawn bathtub without defects.

Chapter 4.   Experimental Analysis of Enameling Resistance to Fish Scale and Corrosion in Sanitary Products

4.1. *Introduction*

In the industry, ceramic enamel coating is widely utilized to safeguard steel products from environmental conditions such as corrosion, heat and abrasion resistance, high hardness, hygiene, and easy cleaning [59]. Sanitary products, for instance, are employed in moist environments like bathtubs.

Enameling involves fusing a thin layer of ceramic or glass onto a metallic substrate, shielding it against chemical attacks or physical damages while enhancing its aesthetic appeal [60]. The typical production process for enameled steel involves two stages: forming the desired shape of a steel substrate in the first stage and enameling in the second stage [61]. Client enameling processes vary, including conventional enameling (EK) with mass enameling and direct white enameling with two high-temperature firings, and direct enameling (ED) using a single covering enamel and one high-temperature firing. These processes necessitate high temperatures, potentially causing austenitic transformation and significant thermal substrate deformation, along with enamel fusion and bonding reactions. Enamel steel requires low carbon concentrations, typically below 0.12%, translating to low carbon content, which results in low strength and high metal elongation. The carbon content in enamel steels can decrease to 0.018% with the addition of Ti, Nb, Zr, or B [62], [63]. Enamel steel characteristics post-enameling resemble those of bimetals, leading to unexpected deformations and excessive residual stresses on final enameled products. These issues exacerbate as steel thickness decreases and enamel-bound part shapes become more complex. Typical enamel part defects include chipping, cracking, warping, and enamel layer peeling. Most of these problems arise post-firing or final assembly due to residual stress distributions in enameled parts. The enamel-steel system exhibits compression stresses at room temperature, with enamel frits having lower thermal expansion than steel. However, enamel expansion becomes more significant than steel when it reaches its glass transition point, leading to enamel tension during initial cooling post-firing [64], [65].

Fish scaling, the primary enamel product defect, relates to excess diffusible hydrogen accumulation at the steel-enamel interface. Increasing the number of hydrogen trapping sites is a method to mitigate scaling occurrence, sometimes appearing in IF steel

due to inadequate and uneven precipitate distribution [19]. Higher sulfur, nitrogen, and titanium contents have been added to facilitate precipitate formation, enhancing scaling resistance. Nickel oxide in enamel can result in larger gas bubbles at the steel-enamel coating interface, increasing scaling resistance due to gas bubble trapping capacity. TiC particles, with strong hydrogen trapping effects, have been used in hot-rolled enameled steels to improve scaling resistance. Additionally, hydrogen storage capacity of TiC particles significantly depends on their size, with smaller TiC particles contributing to higher hydrogen storage capacity [19], [66].

Hot-rolled enamel steels are typically fired at temperatures ranging from 850 to 900°C, modifying microstructure and scaling resistance inevitably. However, there's limited research on the effect of enamel firing on microstructure and scaling resistance of enameled steel [67], [68]. Hydrogen permeation value (TH) is a crucial parameter characterizing scaling resistance, determined by $TH = t_b/d^2$, where t_b is the permeation time and d is the hydrogen permeation sample thickness. A higher TH value corresponds to higher scaling resistance. The determination method of t_b has been described in references [19].
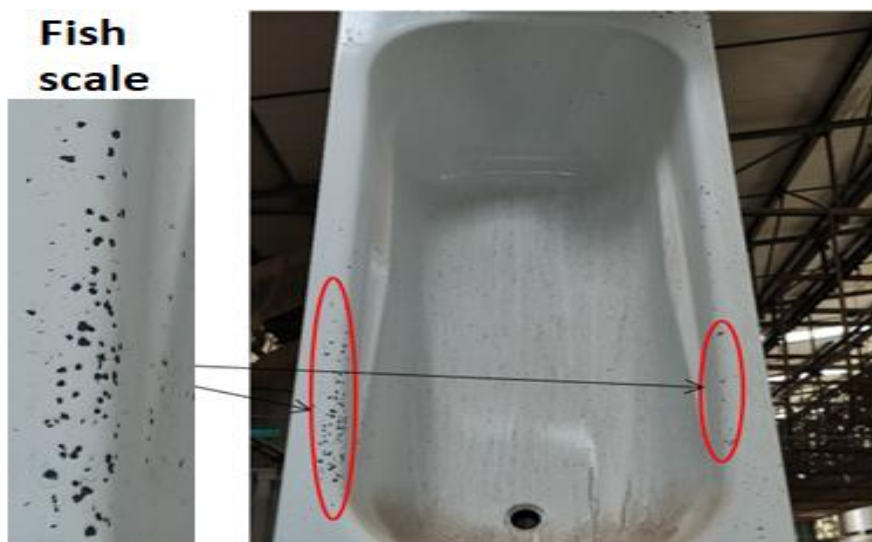

Figure 4-1 : Appearance of fish scales in a bathtub after enameling.

In this study, conducted at the EIMS company, we addressed the escalating rejection rates of enameled products, particularly bathtubs, due to fish scale appearance after deep drawing of DC06EK steel sheets (Figure 4-1). The objective of our

experimental investigation is to analyze fish scale occurrence in enameled sanitary ware concerning induced plastic strain and anisotropy during DC06EK and DC05EK sheet deep drawing. And also, to analyze corrosion phenomena in these type of steel as a function of different levels of plastic strain.

4.2.   Material and experimental methods

4.2.1. Tensile test

In this work, deep-drawing steel DC06EK (DIN EN10209:1998, Material No. 1.0869) with a plate thickness of 1,6 mm was used to carry out the experiments. This sheet is a low-carbon steel designed for vitrification enameling. We carried out uniaxial tensile tests on a set of samples with dimensions of $250{\times}25{\times}1{,}6$ mm^3 from this specimen in the three orientations with respect to the rolling direction (RD): 0°, 45°, and 90° to the RD (Figure 4-2). This was done using the GUNT tensile testing machine with a capacity of 50 kN at a constant speed of 1 mm/min. The aim was to obtain different levels of plastic strain encountered in the forming operation of bathtubs. We did these tests using digital image correlation technique to achieve with precisely plastic strains 0% (no stretched), 2%, 10%, 20%, and 40%.

4.2.2. Preparation of test samples

In the first case, we cut the samples from the sheet in three directions (0°, 45°, and 90°) relative to the RD as follows:

Figure 4-2 : Test samples cut in three directions.

But before going to tensile experiments, speckles were created on the surface of samples in order to use the digital image correlation. Using paint in the sample on one side in white color and after a while we sprayed the surface in black color (Figure 4-3).
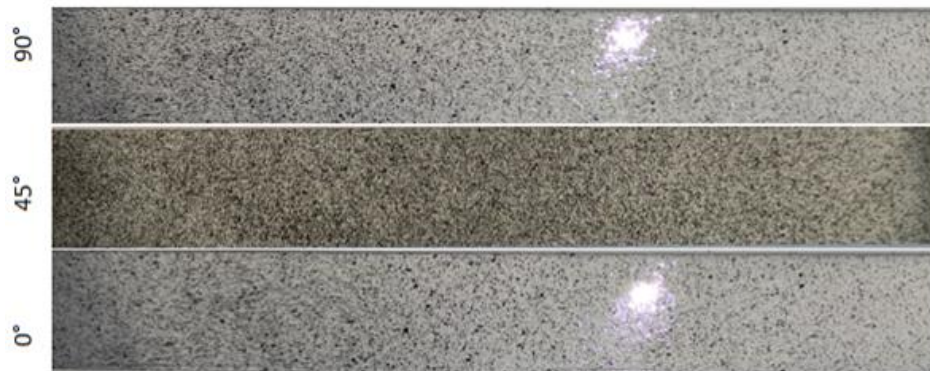

Figure 4-3 : Test samples with a random speckle pattern.

4.2.3. Digital image correlation

Digital Image Correlation (DIC) is an advanced optical technique used in tensile testing to measure full-field displacement and strain on a specimen's surface. It involves applying a high-contrast speckle pattern to the specimen, capturing images at various load stages, and using correlation algorithms to track the movement of speckle subsets from the undeformed to deformed states. This process generates detailed displacement and strain fields, enabling precise, non-contact analysis of material deformation. DIC offers high accuracy and spatial resolution, making it ideal for studying mechanical properties and identifying localized strain concentrations and potential failure points in diverse materials [69], [70].

For processing the images taken during the tensile test, we used GOM software to accurately analyze and determine the true plastic strain in the various stretched samples.

1. Import Images (Load Images into Software): Import the reference image along with all subsequent deformed images into the GOM Correlate software.
2. Define Region of Interest (Select Analysis Area): Define the region of interest on the specimen where the deformation analysis will be conducted. This can include the entire specimen or a specific section.
3. Correlation Analysis:

___

a. Subset Selection: The software automatically divides the region of interest into small subsets or interrogation windows based on the speckle pattern.

b. Tracking and Correlation: GOM Correlate tracks the movement of each subset from the reference image to each deformed image using advanced correlation algorithms. It then calculates the displacement and deformation of each subset.

4. Strain Calculation: The displacement data is used to calculate the strain field. GOM Correlate computes both normal and shear strain components, providing a detailed strain map of the samples.

The strain levels obtained in each orientation with respect to the rolling direction are shown in Figure 4-4.
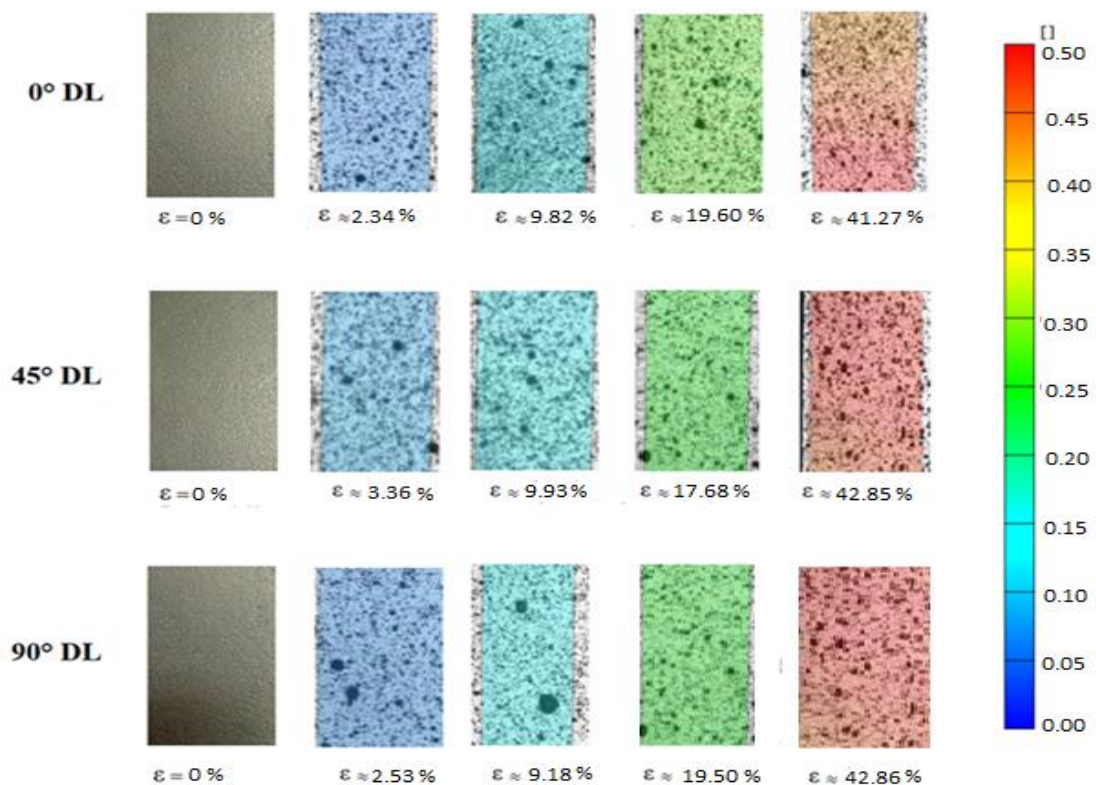

Figure 4-4 : Equivalent plastic strain cartographies of the pre-stretched samples at 0°, 45° and 90° to the RD.

4.2.4. Enameling processes

The pre-stretched were enameled, crossing the same process steps as the bathtubs. The pre-stretched samples are then enameled following the same process used in the Miliana EIMS:

- Test specimen cleaning line:

The first phase of enameling is dedicated to cleaning the samples of impurities and then drying them with hot air.

- Mass coating line:

After cleaning, the samples are unhooked and transferred to the transport conveyor for passage into the coating booth. In this phase, both the front and back surfaces of the samples are glazed with a black layer with a tolerance of $80 \sim 120\,\mu$. The polished samples are transported to the oven for firing (Figure 4-5).

Figure 4-5 : Mass coating line.

- Cover line:

In a final phase, a white covering enamel layer is applied to one of the two surfaces of the sample with a tolerance between 80 and 120 μ, followed also by a drying operation in a box oven at a temperature of between 820 and 840°c (Figure 4-6).

Figure 4-6 : Ligne de couverture.

4.2.5. Electrochemical tests for corrosion detection

This study followed a structured process as outlined below. Corrosion measurements were conducted using a potentiostat. This electronic device regulates the voltage difference between the working and reference electrodes in an electrochemical cell. For this experiment, a computer-controlled potentiostat equipped with Versa Studio software was utilized. The potentiostat has several functions, such as applying potential, monitoring current, storing and analyzing data, and generating trends. Figure 4-7 illustrates the components involved in the corrosion measurement.
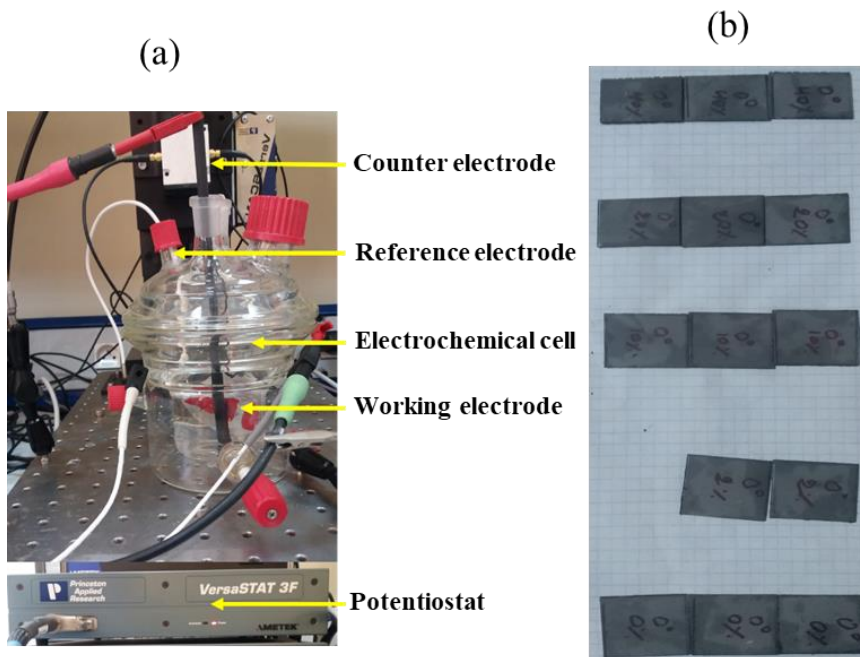

Figure 4-7 : Experimental setup for electrochemical tests.

After conducting the tensile tests with image correlation, we identified the most deformed areas on the samples. We cut these samples into 2 cm sections according to their length (Figure 4-7-b), after removing the enamel, to perform electrochemical experiments to determine the percentage of corrosion on the various samples.

The aim of this study was to evaluate the corrosion resistance of steel DC05EK and DC06EK and in a 3% NaCl solution using potentiodynamic polarization and electrochemical impedance spectroscopy (EIS).

4.3.   Results and discussion

Following the chemical composition tests for the two materials, DC05EK and DC06EK, detailed in the "Analysis of the chemical composition" section (§2.2), certain elements play a crucial role in the enameling process, particularly in preventing the appearance of fish scale defects and corrosion in the final products. Specifically, titanium (Ti), sulfur (S), carbon (C), and nitrogen (N) significantly influence both the corrosion resistance and the occurrence of fish scale defects in DC06EK and DC05EK steels [20], [21]:

- **Titanium (Ti):** Improves both corrosion resistance and reduces fish scale defects by stabilizing carbon and nitrogen as TiC and TiN, preventing chromium carbide/nitride formation and reducing hydrogen traps.
- **Sulfur (S):** Low levels enhance corrosion resistance by minimizing MnS inclusions, which also reduces potential sites for hydrogen accumulation, thus preventing fish scale defects.
- **Carbon (C):** Low carbon content prevents chromium carbide formation, maintaining the protective oxide layer for better corrosion resistance, and reduces hydrogen trapping, which helps prevent fish scale defects.
- **Nitrogen (N):** Controlled nitrogen levels prevent the formation of chromium nitrides, maintaining corrosion resistance, and reduce hydrogen traps, thus minimizing fish scale defects.

After tensile test and enameling operation for the different samples as the same process of enameling of the bathtub in EIMS company, we noticed after 20 days the

beginning of the appearance of fish scale on the undeformed to weakly deformed samples: 0~3% plastic strain (Figure 4-8). This indicates that the appearance of fish scale is more pronounced in areas that are not subject to significant plastic strain.
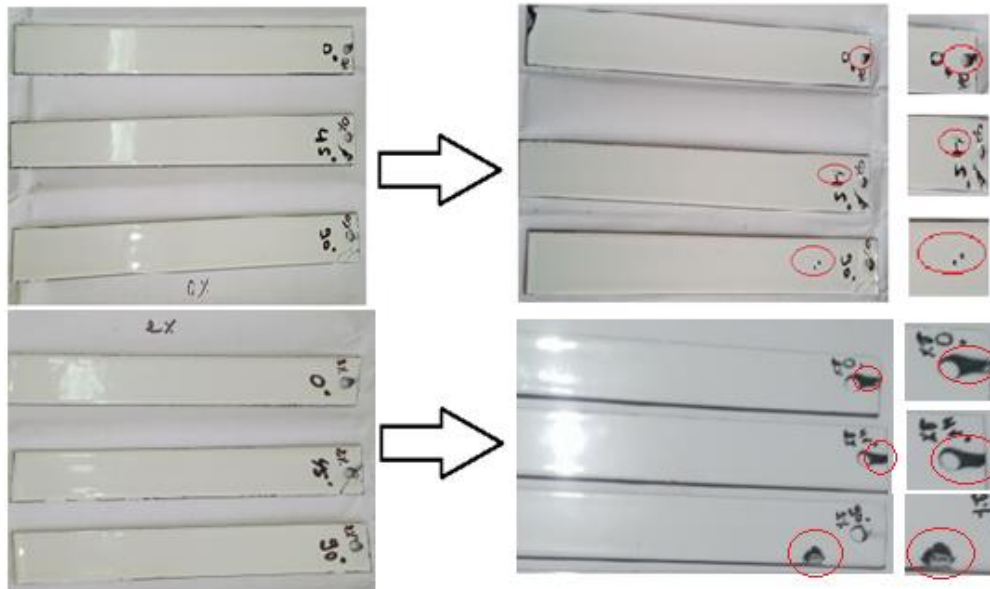

Figure 4-8 : Appearance of fish scale on undeformed samples.

In the bathtubs, these defects in the in the fish may appear after 3 months. However, they also frequently appear in areas of low plastic strain (Figure 4-1). As for the samples, these defects can appear after a long period of time, and this is due to their small size compared to the dimensions of the bathtub. The main reason for the appearance of fish scales is hydrogen (H). Moisture (H_2O), previously present in the furnace, enters the enamel and migrates to the interface with the steel. Oxygen is involved in the adhesion of the enamel to the steel (formation of an iron oxide layer Fe_2O_3 at the enamel/steel interface) [71]. Hydrogen penetrates the steel and concentrates in the small cavities in the sheet. This means that the greater the number of cavities, the higher the concentration of hydrogen in these cavities, but if this decreases (i.e. the smooth surface), this increases the likelihood of these crusts appearing as the hydrogen has nowhere to hide in the bathtub and remains on its surface, then on cooling the solubility of the hydrogen in the steel decreases, and on leaving the furnace, the enamel starts to freeze (hardening of the enamel), and increases in hardness, which puts pressure on the amount of hydrogen concentrated on the surface of the bathtub, which causes the plate to look for a way to get out of this pressure and from the search for weak points in the enamel and the exit to the

_____

outside, the hydrogen pressure at the interface increases and creates the fluctuations in the enamel: **fish scale**.

Also, surface roughness can play an important role depending on the level of plastic strain. From tensile experiments, it has been shown that surface roughness decreases with plastic strain up to 4% and then increases rapidly where high levels of roughness are reached [72]. When the roughness is low, the surface becomes smooth and the enamel is weakly bonded (case of plastic strain between 0~4%). However, enamel bonding becomes significant when the roughness is high (case of plastic strain above ~ 4%).

The polarization curves showed that DC05EK has a slightly higher corrosion potential (Ecorr) and a lower corrosion current density (Icorr) than DC06EK. Electrochemical impedance spectroscopy data revealed that DC05EK has a higher polarization resistance (Rp), indicating better corrosion resistance. The higher Ecorr and lower Icorr for DC05EK imply that it corrodes more slowly in the NaCl solution compared to DC06EK. EIS results support this finding, as the higher Rp for DC05EK corresponds to a lower corrosion rate. The slight passivation behavior observed in DC05EK suggests the formation of a somewhat protective oxide layer. The differences in corrosion behavior are due to slight variations in the composition and microstructure of DC05EK and DC06EK. With its higher polarization resistance, DC05EK demonstrates better overall corrosion resistance. These results are consistent with the losses observed over time in EIMS, so we have noted that DC05EK steel products are more resistant to corrosion than DC06EK products. The results indicate that DC05EK shows superior corrosion resistance compared to DC06EK in a saline environment, making it more suitable for applications exposed to such conditions.

Additionally, the experimental results indicate that the corrosion resistance of DC0xEK steel is significantly influenced by the degree of deformation. The findings show that the corrosion rate is primarily affected by the extent of deformation, with higher deformation leading to increased corrosion. Experimental studies have demonstrated that as the amount of strain increases, the corrosion rate of the steel sheet also increases [73].
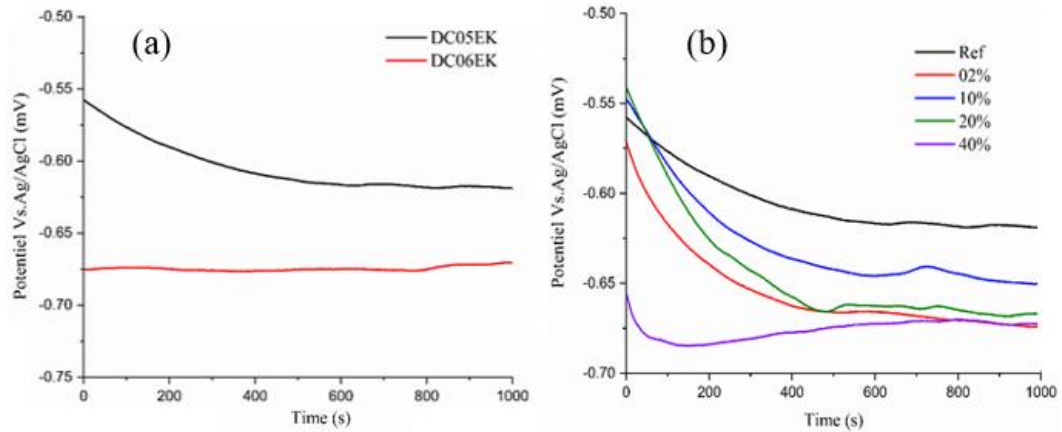
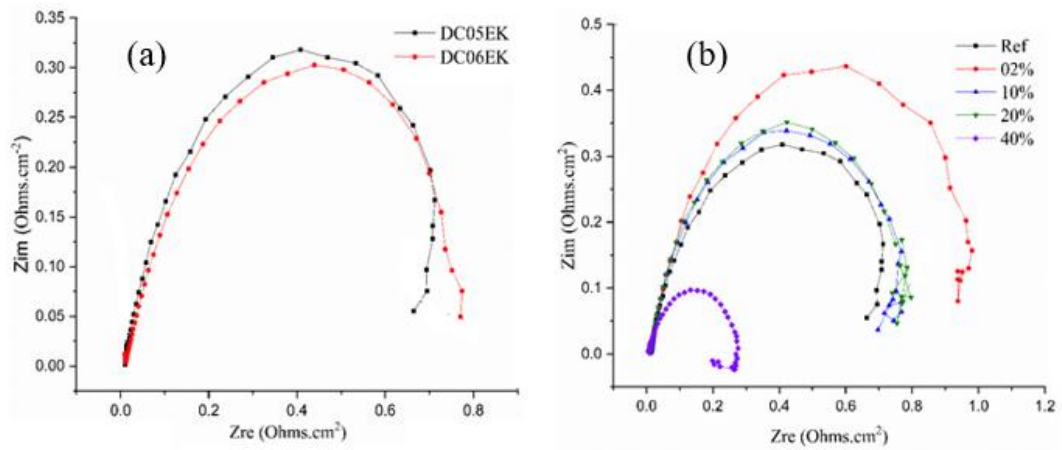**Figure 4-9 : OCP curves: (a) for both steels DC05EK and DC06EK, (b) for pre-stretched samples.**

Figure 4-10 : Electrochemical impedance spectroscopy: (a) for both steels DC05EK and DC06EK, (b) for pre-stretched samples.
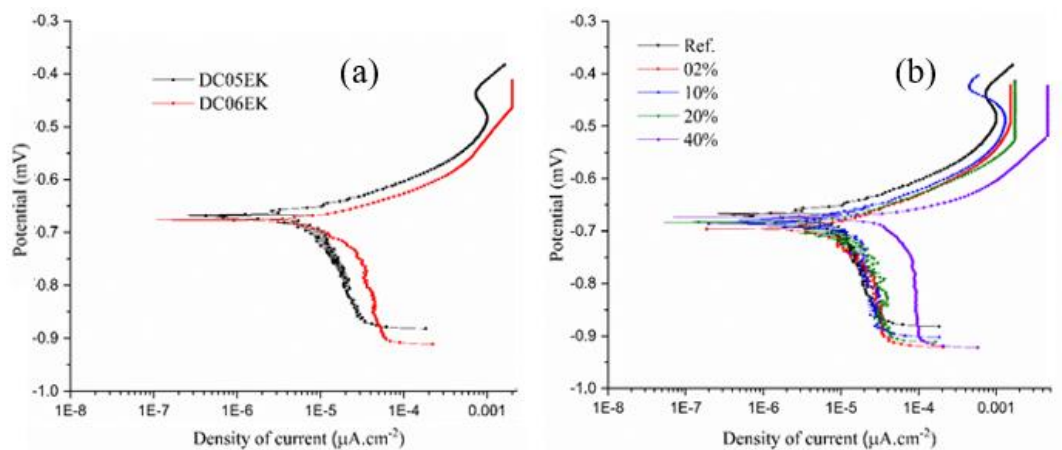

Figure 4-11 : Potentiodynamic curves: (a) for both steels DC05EK and DC06EK, (b) for pre-stretched samples.

_____

4.4.   Conclusions

Different samples are prepared to analyses the occurrence of fish scale in sanitary products. From this experimental analysis, it can be concluded that the occurrence of fish scale in the enamel on the DC06EK sheet is more pronounced in areas of low plastic strain. This is due to the release of the chemical hydrogen component and the low roughness.

The second type of steel (DC05EK), is more resistant to this phenomenon (fish scale), due to the presence of important chemical elements such as C, Ti, N and S, which make a significant contribution to the resistance and adhesion of the enamel.

The results electrochimique indicate that DC05EK shows superior corrosion resistance compared to DC06EK in a saline environment and also the experimental results indicate that the corrosion resistance of DC0xEK steel is significantly influenced by the degree of deformation, with higher deformation leading to increased corrosion.

General conclusions & Perspective

The aim of this thesis was to investigate the suitability of DC0xEK steel sheets for enameling and deep drawing. Two types of materials used in the production of sanitary products at the EIMS company were selected, namely DC05EK and DC06EK. The focus of the work revolves around two main elements: the deep drawing operation and the enameling operation.

First, physical and chemical experiments and analysis were performed on the DC05EK and DC06EK. Chemical and microstructural analyses revealed that the carbon percentage in DC05EK is higher than in DC06EK, indicating better enameling performance for DC05EK. However, tensile tests showed that DC06EK has better mechanical quality than DC05EK. In conclusion, DC05EK steel is more resistant, particularly to fish scale phenomena, compared to DC06EK, which has better formability. Therefore, the level of strain must be considered when choosing between the two materials.

The chemical compositions of the two steels, DC05EK and DC06EK, differ from the data provided by the company EIMS (Annex 03). This discrepancy affects the extent of losses, highlighting the importance of verifying and ensuring the authenticity of the supplier's documents.

Concerning the deep drawing process, numerical simulation was discussed and performed using real characteristics utilized within the company, aiming to save time, costs, and aid production development. In this context, the EDD process of bathtub type "1400" was simulated using Abaqus/Explicit finite element software. The validation of this numerical approach was conducted through ultrasonic thickness measurements, confirming its accuracy and reliability. Analysis of various scenarios of BHP revealed that the EDD process approaches its formability limits. Even with uniform BHP, defects still occur in the final product, emphasizing the complexity of controlling blank flow. Non-uniform BHP is essential for controlling flow due to the bathtub's complex geometry, with optimal pressures falling within a narrow range. Sheet metal cutting

angles and draw beads are critical factors in achieving defect-free deep-drawn bathtubs. Optimizing BHP control can reduce energy consumption during the process.

For testing purposes, the focus lies on the enameling process, specifically analyzing the occurrence of fish scales in enameled sanitary appliances based on the plastic strain and anisotropy induced during the deep drawing of DC06EK and DC05EK steel sheets. Subsequently, the corrosion phenomena in this type of steel are analyzed based on different levels of strain. This experimental analysis leads to the conclusion that the appearance of fish scale in the enamel of DC06EK sheets is more pronounced in areas of low plastic strain. This is attributed to the release of chemical hydrogen and low roughness.

The second type of steel (DC05EK) exhibits greater resistance to this phenomenon (fish scales) due to the presence of significant chemical elements such as C, Ti, N, and S, which contribute significantly to the strength and adhesion of the enamel. The electrochemical results show that DC05EK has better corrosion resistance than DC06EK in a saline environment. Additionally, experimental results indicate that the corrosion resistance of DC0xEK steel sheets is significantly affected by the degree of deformation, with greater deformation resulting in increased corrosion.

This study offers valuable insights into the extra-deep drawing and enameling process. Future research could explore extending this study to other sheet metals and more complex geometries, enhancing our understanding of the deep drawing process and its applications across various industrial sectors. Collaborating with industrial partners and conducting real-world trials would help integrate research findings into practical manufacturing processes, increasing productivity and reducing costs.

Regarding enamel, to prevent defects and ensure strong adhesion to the steel, alternative enamel types could be considered, or adjustments could be made to the enamel's thickness applied to the steel.

Références

[1]   H. Abichou, "Simulation de l ' emboutissage à froid par une méthode asymptotique numérique Hammadi Abichou To cite this version : HAL Id : tel-01775454 soutenance et mis à disposition de l ' ensemble de la Contact : ddoc-theses-contact@univ-lorraine.fr," 2018.

[2]   EIMS, "Entreprise industrielle de materiel sanitaire (EIMS-Miliana), Algeria," 2024.

[3]   H. A. L. Id, "Contribution à la modélisation de l ' emboutissage de tôles minces par l ' approche inverse . Frédéric Mercier To cite this version : HAL Id : tel-01123948," 2015.

[4]   B. Ouzine, "Mise au point d'un critère de striction pour l'emboutissage des tôles et validation par simulations numériques," Université Badji Mokhtar ANNABA, 2010.

[5]   C. Alain and M. Colombié, "L'emboutissage des aciers," Dunod, 2010.

[6]   F. Apev, "Les aciers pour émaillage Contenu," pp. 0–23, 2014.

[7]   Y. K. Son, K. H. Lee, K. S. Yang, D. C. Ko, and B. M. Kim, "Prediction of residual stress and deformation of enameled steel," Int. J. Precis. Eng. Manuf., vol. 16, no. 7, pp. 1647–1653, 2015, doi: 10.1007/s12541-015-0216-9.

[8]   A. Europe and F. Products, "Steel for enamelling and enamelled steel User manual ArcelorMittal Europe-Flat Products 3 User manual-Steel for enamelling and enamelled steel-ArcelorMittal User manual Steel for enamelling and enamelled steel".

[9]   Exol-lubricants Company, "Website of Exol-lubricants Company," 2022.

[10]   M. ABBADENI, "Simulation de l'Interaction Fluide-Structure Pour le Procédé d'Hydroformage," Université Hassiba Benbouali de Chlef, 2018.

[11]   M. Azaouzi, "Modélisation et optimisation numérique de l ' emboutissage de pièces de précision en tôlerie fine Mohamed Azaouzi To cite this version : HAL Id : tel-01752909 soutenance et mis à disposition de l ' ensemble de la Contact : ddoc-theses-contact@univ-lorrain," 2018.

[12]   Ö. Işıksaçan, O. Yücel, and A. Yeşilçubuk, "Vitreous Enamel Coating Surface Defects and Evaluation of the Causes," Int. Adv. Res. J. Sci. Eng. Technol. ISO, vol. 5, no. 5, pp. 6–11, 2018, doi: 10.17148/IARJSET.2018.552.

[13]   R. R. Danielson and W. H. Souder, "the Causes and Control of Fish Scaling of Enamels for Sheet Iron and Steel," J. Am. Ceram. Soc., vol. 4, no. 8, pp. 620–654, 1921, doi: 10.1111/j.1151-2916.1921.tb17363.x.

[14]   I. Zidane, "Developpement d'un banc d'essai de traction biaxiale pour la caractérisation de la formabilité et du comportement élastoplastique de tôles métalliques," Rennes, INSA, 2009.

[15]   M. Ben Tahar and M. Ben Tahar, "Contribution ` a l ' ´ etude et la simulation du proc ´ e l ' hydroformage To cite this version :," 2005.

[16]   A. Belguebli, I. Zidane, A. Hadj Amar, and A. Benhamou, "Numerical

investigation of an extra-deep drawing process with industrial parameters: formability analysis and process optimization," Frat. ed Integrità Strutt. (Fracture Struct. Integrity, F&SI), vol. 18, no. 68, pp. 45–62, 2024, doi: 10.3221/IGF-ESIS.68.03.

[17]   S. P. Keeler, "Relationship between laboratory material characterization and press-shop formability," 1977.

[18]   S. K. Paul, "Controlling factors of forming limit curve: A review," Adv. Ind. Manuf. Eng., vol. 2, p. 100033, 2021, doi: 10.1016/j.aime.2021.100033.

[19]   Z. Liu, W. Li, X. Shao, Y. Kang, and Y. Li, "An Ultra-low-Carbon Steel with Outstanding Fish-Scaling Resistance and Cold Formability for Enameling Applications," Metall. Mater. Trans. A, vol. 50, no. 4, pp. 1805–1815, Apr. 2019, doi: 10.1007/s11661-018-05101-z.

[20]   D. H. Stamatis, "TQM Engineering Handbook," TQM Eng. Handb., 1997, doi: 10.1201/9781482269826.

[21]   P. Cunat, "and Other Chromium-Containing Alloys," pp. 1–24, 2004.

[22]   American Society for Testing and Materials, ASTM E8/E8M – 22: Standard Test Methods for Tension Testing of Metallic Materials. Volume 3.01. ASTM standards, 2022. doi: 10.1520/E0008_E0008M-22.

[23]   I. Zidane, "Développement d'un banc d'essai de traction biaxale pour la caracterisation de la formabilité et du comportement élastoplastique de tôles métalliques." Rennes, INSA, 2009.

[24]   N. Vukašinović and J. Duhovnik, "Introduction to reverse engineering," Springer Tracts Mech. Eng., pp. 165–177, 2019, doi: 10.1007/978-3-030-02399-7_7.

[25]   X. Zexiao, W. Jianguo, and Z. Qiumei, "Complete 3D measurement in reverse engineering using a multi-probe system," Int. J. Mach. Tools Manuf., vol. 45, no. 12–13, pp. 1474–1486, 2005, doi: 10.1016/j.ijmachtools.2005.01.028.

[26]   M. Colgan and J. Monaghan, "Deep drawing process: analysis and experiment," J. Mater. Process. Technol., vol. 132, no. 1–3, pp. 35–41, Jan. 2003, doi: 10.1016/S0924-0136(02)00253-4.

[27]   R. Padmanabhan, M. C. Oliveira, J. L. Alves, and L. F. Menezes, "Influence of process parameters on the deep drawing of stainless steel," Finite Elem. Anal. Des., vol. 43, no. 14, pp. 1062–1067, Oct. 2007, doi: 10.1016/j.finel.2007.06.011.

[28]   C. Singh and G. Agnihotri, "Study of Deep Drawing Process Parameters: A Review," in International Journal of Scientific and Research Publications, 2015, p. Vol. 5-2.

[29]   J. Heingärtner, D. Bonfanti, D. Harsch, F. Dietrich, and P. Hora, "Implementation of a tribology-based process control system for deep drawing processes," IOP Conf. Ser. Mater. Sci. Eng., vol. 418, p. 012112, Sep. 2018, doi: 10.1088/1757-899X/418/1/012112.

[30]   L. Leotoing, D. Guines, I. Zidane, and E. Ragneau, "Cruciform shape benefits for experimental and numerical evaluation of sheet metal formability," J. Mater. Process. Technol., vol. 213, no. 6, 2013, doi: 10.1016/j.jmatprotec.2012.12.013.

[31]   I. Zidane, D. Guines, L. Leotoing, and E. Ragneau, "Development of an in-plane

biaxial test for forming limit curve (FLC) characterization of metallic sheets," Meas. Sci. Technol., vol. 21, no. 5, p. 55701, 2010.

[32]   F.-K. Chen and B.-H. Chiang, "Analysis of die design for the stamping of a bathtub," J. Mater. Process. Technol., vol. 72, no. 3, pp. 421–428, Dec. 1997, doi: 10.1016/S0924-0136(97)00205-7.

[33]   D. Woźniak, M. Głowacki, M. Hojny, K. Żaba, M. Nowosielski, and M. Kwiatkowski, "Analysis Of Die Design For The Stamping Of A Bathtub," Arch. Metall. Mater. DOI - 10.1515/amm-2015-0189, no. No 2 June, 2015.

[34]   M. Tomáš, E. Evin, J. Kepič, and J. Hudák, "Physical Modelling and Numerical Simulation of the Deep Drawing Process of a Box-Shaped Product Focused on Material Limits Determination," Metals (Basel)., vol. 9, no. 10, p. 1058, Sep. 2019, doi: 10.3390/met9101058.

[35]   S. Kitayama, H. Koyama, K. Kawamoto, T. Noda, K. Yamamichi, and T. Miyasaka, "Numerical and experimental case study on simultaneous optimization of blank shape and variable blank holder force trajectory in deep drawing," Struct. Multidiscip. Optim., vol. 55, no. 1, pp. 347–359, Jan. 2017, doi: 10.1007/s00158-016-1484-4.

[36]   Y. Feng, Z. Hong, Y. Gao, R. Lu, Y. Wang, and J. Tan, "Optimization of variable blank holder force in deep drawing based on support vector regression model and trust region," Int. J. Adv. Manuf. Technol., vol. 105, no. 10, pp. 4265–4278, Dec. 2019, doi: 10.1007/s00170-019-04477-5.

[37]   K. M. Wurster, M. Liewald, and C. Blaich, "Procedure for Automated Virtual Optimization of Va- riable Blank Holder Force Distributions for Deep- Drawing Processes with LS-Dyna and optiSLang," 2011.

[38]   L. Zhong-qin, W. Wu-rong, and C. Guan-long, "A new strategy to optimize variable blank holder force towards improving the forming limits of aluminum sheet metal forming," J. Mater. Process. Technol., vol. 183, no. 2–3, pp. 339–346, 2007, doi: 10.1016/j.jmatprotec.2006.10.027.

[39]   H. Schmid and M. Merklein, "Influence of a drawbead passage in deep drawing processes on surface values and the tribological system," IOP Conf. Ser. Mater. Sci. Eng., vol. 967, no. 1, 2020, doi: 10.1088/1757-899X/967/1/012008.

[40]   G. Sun, G. Li, Z. Gong, X. Cui, X. Yang, and Q. Li, "Multiobjective robust optimization method for drawbead design in sheet metal forming," Mater. Des., vol. 31, no. 4, pp. 1917–1929, Apr. 2010, doi: 10.1016/j.matdes.2009.10.050.

[41]   G. Sun, G. Li, Z. Gong, G. He, and Q. Li, "Radial basis functional model for multi-objective sheet metal forming optimization," Eng. Optim., vol. 43, no. 12, pp. 1351–1366, Dec. 2011, doi: 10.1080/0305215X.2011.557072.

[42]   H. Gharehchahi, M. J. Kazemzadeh-Parsi, A. Afsari, and M. Mohammadi, "Blank shape optimization in the deep drawing process by sun method," Prod. Eng., vol. 15, no. 5, pp. 735–750, 2021, doi: 10.1007/s11740-021-01049-z.

[43]   W. Ghennai, O. Boussaid, H. Bendjama, B. Haddag, and M. Nouari, "Experimental and numerical study of DC04 sheet metal behaviour—plastic anisotropy identification and application to deep drawing," Int. J. Adv. Manuf. Technol., vol. 100, no. 1–4, pp. 361–371, 2019, doi: 10.1007/s00170-018-2700-8.

[44]   W. Ghennai, O. Boussaid, H. Bendjama, and N. Guersi, "Pressure and friction effects on the mechanical behaviour of a ductile material during deep drawing," Int. J. Eng. Res. Africa, vol. 41, pp. 8–19, 2019, doi: 10.4028/www.scientific.net/JERA.41.8.

[45]   D. M. Neto, M. C. Oliveira, A. D. Santos, J. L. Alves, and L. F. Menezes, "Influence of boundary conditions on the prediction of springback and wrinkling in sheet metal forming," Int. J. Mech. Sci., vol. 122, pp. 244–254, 2017, doi: 10.1016/j.ijmecsci.2017.01.037.

[46]   W. Bahanan et al., "A Finite Element Analysis of Cold Deep Drawing of Al Alloy Considering Friction Condition and Corner Design of Plunger," Lubricants, vol. 11, no. 9. 2023. doi: 10.3390/lubricants11090388.

[47]   H. Kim, J. H. Sung, R. Sivakumar, and T. Altan, "Evaluation of stamping lubricants using the deep drawing test," Int. J. Mach. Tools Manuf., vol. 47, no. 14, pp. 2120–2132, 2007, doi: 10.1016/j.ijmachtools.2007.04.014.

[48]   DASSAULT SYSTEMES, "Abaqus 6.14 Theory Guide," Rigid body definition, 2014.

[49]   E. Önder and A. E. Tekkaya, "Numerical simulation of various cross sectional workpieces using conventional deep drawing and hydroforming technologies," Int. J. Mach. Tools Manuf., vol. 48, no. 5, 2008, doi: 10.1016/j.ijmachtools.2007.06.012.

[50]   Y. S. Kim, M. K. Jain, and D. R. Metzger, "Determination of pressure-dependent friction coefficient from draw-bend test and its application to cup drawing," Int. J. Mach. Tools Manuf., vol. 56, 2012, doi: 10.1016/j.ijmachtools.2011.12.011.

[51]   R. Hill, "A user-friendly theory of orthotropic plasticity in sheet metals," Int. J. Mech. Sci., vol. 35, no. 1, pp. 19–25, 1993, doi: 10.1016/0020-7403(93)90061-X.

[52]   DASSAULT SYSTEMES, "Abaqus/CAE User's Guide (2016)," Understanding interactions, 2016.

[53]   B. Şener and H. Kurtaran, "Modeling the deep drawing of an AISI 304 stainless-steel rectangular cup using the finite-element method and an experimental validation," Mater. Tehnol., vol. 50, pp. 961–965, 2016, doi: 10.17222/MIT.2015.278.

[54]   S. Holmberg, B. Enquist, and P. Thilderkvist, "Evaluation of sheet metal formability by tensile tests," J. Mater. Process. Technol., vol. 145, no. 1, pp. 72–83, 2004, doi: 10.1016/j.jmatprotec.2003.07.004.

[55]   D. Briesenick and M. Liewald, "Efficient net shape forming of high-strength sheet metal parts by Transversal Compression Drawing," Int. J. Adv. Manuf. Technol., vol. 130, no. 5, pp. 3053–3063, 2024, doi: 10.1007/s00170-023-12880-2.

[56]   A. Shafiee Sabet et al., "Tribological investigations on aluminum alloys at different contact conditions for simulation of deep drawing processes," J. Manuf. Process., vol. 68, pp. 546–557, Aug. 2021, doi: 10.1016/j.jmapro.2021.05.050.

[57]   M. Abbadeni, I. Zidane, H. Zahloul, A. Fatu, and M. Hajjam, "Finite element analysis of fluid-structure interaction in the hydromechanical deep drawing process," J. Mech. Sci. Technol., vol. 31, no. 11, 2017, doi: 10.1007/s12206-017-

1043-y.

[58] J. Venema, J. Hazrati, E. Atzema, D. Matthews, and T. van den Boogaard, "Multiscale friction model for hot sheet metal forming," Friction, 2021, doi: 10.1007/s40544-021-0504-6.

[59] A. Zucchelli, G. Minak, and D. Ghelli, "Low-velocity impact behavior of vitreous-enameled steel plates," Int. J. Impact Eng., vol. 37, no. 6, pp. 673–684, 2010, doi: 10.1016/j.ijimpeng.2009.12.003.

[60] F. Russo, S. Rossi, and A. M. Compagnoni, "Porcelain Enamel Coatings," Encyclopedia, vol. 1, no. 2, pp. 388–400, 2021, doi: 10.3390/encyclopedia1020032.

[61] Y. K. Son, C. J. Lee, J. M. Lee, and B. M. Kim, "Deformation prediction of porcelain-enameled steels with strain history by press forming and high-temperature behavior of coating layer," Trans. Nonferrous Met. Soc. China (English Ed., vol. 22, no. SUPPL.3, pp. s838–s844, 2012, doi: 10.1016/S1003-6326(12)61813-5.

[62] X. Yang, A. Jha, S. Ali, and R. C. Cochrane, "Mass-transport processes at the steel-enamel interface," Metall. Mater. Trans. B Process Metall. Mater. Process. Sci., vol. 37, no. 1, pp. 89–98, 2006, doi: 10.1007/s11663-006-0088-6.

[63] K. Y. Frolenkov, L. Y. Frolenkova, and I. F. Shadrin, "High-temperature oxidation of low-alloyed steel under glass coatings," Prot. Met. Phys. Chem. Surfaces, vol. 46, no. 1, pp. 103–109, 2010, doi: 10.1134/S2070205110010156.

[64] D. Wang, "Effect of crystallization on the property of hard enamel coating on steel substrate," Appl. Surf. Sci., vol. 255, no. 8, pp. 4640–4645, 2009, doi: 10.1016/j.apsusc.2008.12.007.

[65] M. Shirasaki, T. Shimizu, and Y. Iizawa, "Evaluation method for the adhesion strength of vitreous enamel," J. Mater. Sci., vol. 34, no. 1, pp. 209–212, 1999, doi: 10.1023/A:1004475204579.

[66] J. Takahashi, K. Kawakami, Y. Kobayashi, and T. Tarui, "The first direct observation of hydrogen trapping sites in TiC precipitation-hardening steel through atom probe tomography," Scr. Mater., vol. 63, no. 3, pp. 261–264, 2010, doi: 10.1016/j.scriptamat.2010.03.012.

[67] M. B. Lupescu, M. Zaharescu, and A. Andrei, "Electron spectroscopy studies of the steel/enamel interface," Mater. Sci. Eng. A, vol. 232, no. 1–2, pp. 73–79, 1997, doi: 10.1016/s0921-5093(97)00095-6.

[68] M. Jiang, X. Yang, S. Pan, B. W. Krakauer, and M. Zhu, "Correlation between Microstructures and Yield Strength of a High Strength Enameling Steel," J. Mater. Sci. Technol., vol. 28, no. 8, pp. 737–744, 2012, doi: 10.1016/S1005-0302(12)60123-6.

[69] Z. Jorge, P. Ronny, and O. Sotomayor, "On the digital image correlation technique," Mater. Today Proc., vol. 49, pp. 79–84, 2022, doi: 10.1016/j.matpr.2021.07.476.

[70] G. M. Hassan, "Deformation measurement in the presence of discontinuities with digital image correlation : A review," Opt. Lasers Eng., vol. 137, no. June 2020, p.

106394, 2021, doi: 10.1016/j.optlaseng.2020.106394.

[71] A. Europe and F. Products, "ArcelorMittal Europe-Flat Products Enamelled steel A traditional material for modern living".

[72] R. Haar, "Friction in sheet metal forming, the influence of (local) contact conditions and deformation," Enschede Univ. Twente, p. 151, 1996.

[73] J. Brezinová, J. Slota, M. Tomáš, and J. Koncz, "The effect of strain amount on corrosion behavior of EDDQ steel sheet," Koroze a Ochr. Mater., vol. 60, no. 4, pp. 128–131, 2016, doi: 10.1515/kom-2016-0020.

Annex 1

EIMS SPA Structure : Études C.F : 453 Doc. N° : 453 / 1 . 03	FICHE TECHNIQUE DU PRODUIT BAIGNOIRE 1400

DESIGNATION : BAIGNOIRE 1400 EN ACIER EMAILLE **NF D 11-112*****
CODE: 61 113 01* 4
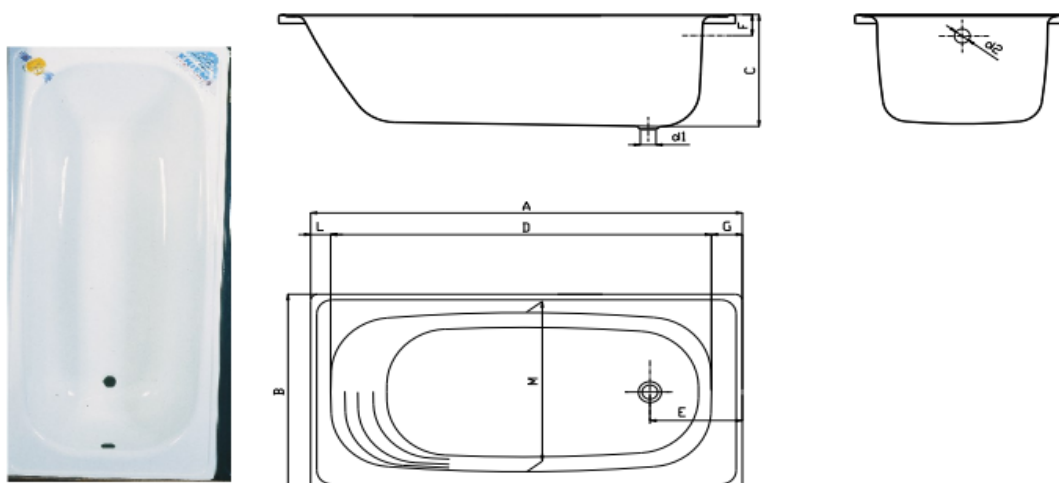
DIMENSION : toutes les dimensions en mm

	A	B	C	D	E	F	G	L	M	d1	d2
PO CO	1400	700	400	1229	278	153	100	75	570	51	52

NATURE DE REVETEMENT : Email sous forme vitrifiée en deux couches (masse et couverture),
Epaisseur 120 µ pour chaque couche .
RESISTANCE DE L'EMAIL : Essais aux choc à 4 Kg/cm² satisfaisant , Résistance aux acides alcalins
et détergents

* : Le 01 indique la couleur blanche
*** : Selon Norme française homologuée par décision du directeur général de L'AFNOR le 5 avril 1987 pour prendre effet le 05 mai 1987

Annex 2

Scale: 1/20		Name:HADJ AMAR
	Blank holder	First name:Adel
		Date:13/06/2024
Hassiba Benbouali University, Chlef		

Scale: 1/20		Name:HADJ AMAR
	Die	First name:Adel
		Date:13/06/2024
Hassiba Benbouali University, Chlef		

Scale: 1/10		Name:HADJ AMAR
	Punch	First name:Adel
		Date:13/06/2024
Hassiba Benbouali University, Chlef		

Scale: 1/20		Name:HADJ AMAR
	Blank	First name:Adel
		Date:13/06/2024
Hassiba Benbouali University, Chlef		

ArcelorMittal

ArcelorMittal Belgium NV
ArcelorMittal Gent

John Kennedylaan, 51
9042 Gent (België)

Tel.: +32 9.347.31.11
Fax: +32 9.347.49.07

A01

A02 CERTIFICAT
CERTIFICAT DE RECEPTION SUIVANT EN10204-3.1
OU EQUIVALENT.

A03 211565852 P. 01/01

A05 AUTEUR DU DOCUMENT
AM GENT/ DEPARTEMENT QUALITE

A09 AVIS D'EXPEDITION 3763790 **A06.1** CLIENT
DATE 09-11-2021
TOLCOLOR S.A.
25, RUE DES ECOLES - BP8P 839
F-95508 LE THILLAY
FRANCE
6574362

A08 NO DE COMMANDE
DATE 99552
A06.2 DESTINATION
TOLCOLOR S.A.
25, RUE DES ECOLES - BP8P 839
F-95508 LE THILLAY
FRANCE
6574436

A07 VOTRE COMMANDE NO 210STO007
DATE 06-05-2021

CONTRAT NO GC14TO3001

NOS REFERENCES
VOS REFERENCES DBC-AU/VJRE
NORME « TOLCOLOR/ETM

B01-B04 MATERIEL -- BOBINES LAMINEES A FROID, RECUITES, SKINPASSEES,
QUALITE DC06EK
STAND: EN 10131 (2006) NORM.TOL.

B09 POSTE B10 LARGEUR **B11** EPAISSEUR
MM MM
02 1.400 1.60

B09 POSTE	PAQUET	B13 POIDS	B07 BOBINE	B08 COULEE
02	866828178 12790	KG 49222500	85312	7
	866828184 10580	49222517	85313	7
	2 23470			

2 23470

ANALYSE CHIMIQUE
C20 ELABORATION D'ACIER: LD

	C71 C	C72 Mn	C73 Si	C74 P	C75 S	C76 N	C77 Al.t	C78 Ti	C79 Cr	C80 Ni	C81 Cu	C82 Nb	C83 B	C84 V	C85 Mo
	10⁻³%	10⁻³%	10⁻³%	10⁻³%	10⁻⁴%	10⁻³%	10⁻³%	10⁻³%	10⁻³%	10⁻³%	10⁻³%	10⁻³%	10⁻⁴%	10⁻³%	10⁻³%
	7	14	6	5	28	54	107	13	11	10	0	1	5	2
	7	13	5	5	28	30	52	108	12	11	0	1	0	3

PROPRIETES MECANIQUES
TEST DE TRACTION

B09 POSTE	PAQUET	C04 CO2	C11 LIM.ELAST.RESIST. RpO.2	C12 RESIST. Rm	A%	C13
			MPa	MPa	10⁻²	10⁻² 10⁻²
02	866828178	F D	140	304	42 235 245
	866828184	F D	137	297	46 285 250

REMARQUES
EPROUVETTE DE TRACTION LC/LO/B0 120/80/20 MM.
210STO007/001

CO4 ETAT D'ESSAIS
V:AGEE F:FRAIS N:NORMALISEE
CO2 DIRECTION D'ESSAIS
L:OGR S:45GR D:90GR

Zetsic: Kalicarlaclaan 68, B-1000 Brussel (België) BTW BE 0400.106.361 RPR Brussel

TOLCOLOR SAS
25 rue des Ecoles - BP 839
95508 LE THILLAY cedex
Tél 01.39.92.86.45 - Fax 01.39.92.86.48
Email jeticolor@tolcolor.fr

GENT 09-11-2021

R. SLOCK
SERVICE QUALITE

ANALYSE CHIMIQUE — PROPRIETES MECANIQUE

N°COULEE	C %	Mn 10⁻³%	Si 10⁻³%	P 10⁻³%	S 10⁻³%	N 10⁻³%	Al-t 10⁻³%	Ti 10⁻³%	Cr 10⁻³%	Ni 10⁻³%	Cu 10⁻³%	Nb 10⁻³%	B 10⁻³%	V 10⁻³%	Mo 10⁻³%	Co4	Co2	Rpo 2 Mpa	Rm Mpa	A %	e 10⁻³%	N 10⁻³%
855578 (2)	40	20	7	11	24	69	33	1	14	8	8	0	1	0	1	V	D	170	306	41	215	225
86779 (2) DC	50	19	5	9	26	68	35	1	21	30	25	0	1	2	0	V	D	150	297	41	230	230
86780 (2) 05	50	18	5	8	25	72	34	1/ cef 12	19	7	0	1	0	1	V	D	168	305	42	240	225	
86780 (2) EK	50	18	6	8	25	78	35	1	13	20	7	0	0	0	1	V	D	166	303	42	205	230
85312 (2)		14	6	5	28	32	54	107	13	11	10	0	1	5	2	F	D	140	306	42	235	245
85313		13	5	5	28	30	52	108	12	11	10	0	1	0	3	F	D	137	297	46	245	240
85312 (2) DC		14	5	6	28	32	54	106	15	10	9	1	1	5	2	F	D	138	302	47	204	250
86660 (2) 06		13	6	11	28	24	43	99	16	21	13	0	0	5	2	F	D	135	302	42	245	255
86657 (2) EK		13	6	9	27	25	52	104	20	22	18	0	1	0	2	F	D	145	304	42	240	245
86660 (2)		13	5	10	28	28	46	102	17	21	14	0	0	6	2	F	D	137	303	45	240	250
86660 (1)		13	6	11	28	24	43	99	16	21	13	0	0	5	2	F	D	139	303	42	225	250
86607 (2)		13	6	9	27	27	50	102	20	22	17	0	1	0	2	F	D	142	303	45	219	250